Hydroxyapatite/Titanium Composite Coating for Biomedical Applications

by

Xuan Zhou

A dissertation submitted in partial fulfillment
of the requirements for the degree of
Doctor of Philosophy
(Automotive System Engineering)
in The University of Michigan-Dearborn
2012

Doctoral Committee:

Professor Pravansu Mohanty, Chair
Professor Pankaj Mallick
Associate Professor Krisanu Bandyopadhyay
Assistant Research Professor Ramesh Guduru

To my parents, my wife and my daughter

Acknowledgements

First and foremost I want to thank my dissertation advisor, Prof. Pravansu Mohanty. It has been an honor to be his graduate student. He has taught me much both consciously and unconsciously. I appreciate all his contributions of time, ideas, and funding to make my graduate experience productive and stimulating. Without his knowledge and technical support, this thesis would have never been achieved. I would also like to express thanks and gratitude to my other dissertation committee members, Dr. Pankaj Mallick, Dr. Kris Bandyopadhyay, and Dr. Ramesh Guduru for their contribution to my scientific training and growth.

Thanks to all the students and research scholars in the Additive Manufacturing Processes Laboratory (particularly Dr. Satishkumar B C, Harishankar Umapathy, Nick Moroz, Raj Siman, Ramcharan Palacode Visveswaran, Raghava Tummala, Vikram Varadaraajan, Animesh Koneru, Lin Lu, Yaping Wang, Jovan Stanisic), they have contributed immensely to my personal and professional time at the University of Michigan – Dearborn. They enriched my life and broadened my horizon. Thanks so much to all professors in Mechanical Engineering Department for their immense help. And thanks to all my friends who stuck around while I tried to complete this.

I would also like to express my special appreciation to our beloved Abhinav Choudhari who has left us four years ago. He helped me start this research and finished part of the spraying processes. This dissertation would not have been possible without his support.

And last but not the least I would like to thank my parent and my wife for all their love and encouragement. Their faithful support during this stage is so appreciated. Thank you.

Table of Contents

Chapter

List of Tables

List of Figures

Abstract

Hydroxyapatite/Titanium Composite Coating for Biomedical Applications

by

Xuan Zhou

Chair: Pravansu Mohanty

Hydroxyapatite, (HAP), a calcium phosphate bioceramic material, has been widely used in both dentistry and orthopaedics due to its biocompatibility and osteoconductivity. However, its poor bulk mechanical properties have limited its use as load bearing material. An effective approach to solve this problem is to form a composite coating of HAP and Titanium, in which titanium will be the matrix and HAP will act as reinforcement.

In this research, two novel approaches, namely cold gas dynamic spraying (CGDS) and argon atmosphere plasma spraying (AAPS), were applied to manufacture HAP/Ti composite coatings. The aim was to produce thick and dense deposits and investigate the mechanical, electrochemical and incubation behavior of such biocomposites as potential load bearing materials for biomedical applications. The complex nature of the manufacturing processes and the characteristics of these materials make this a challenging study in terms of coating manufacturing and property evaluation.

For cold sprayed HAP/Ti composite coatings, it was found that the phase composition of the HAP in the deposits was identical to that of the precursor powder and the bond strength of the deposit was comparable/better to that of the plasma sprayed 100% HAP typically used in industry. A relatively higher corrosion current of HAP/Ti composite than that of pure Ti coating in simulated body fluid indicated a good bioactivity for composite coating, which was also verified by the formation of apatite layer on the surface of composite coating in *in-vitro* testing. The cold sprayed HAP/Ti composite is expected to be a promising load-bearing implant material for biomedical applications.

For AAPS-deposited HAP/Ti composite coatings, results demonstrated that dense composite coatings with a typical morphology of HAP homogenously distributed in Ti matrix was obtained and the decomposition of HAP during plasma spraying process was avoided. The bond strength was significantly higher than that of 100% HAP or Ti reinforced cold sprayed HAP coatings and the frictional property was comparable to the Ti substrate. A relatively higher corrosion current of HAP/Ti composite than that of pure Ti coating indicated a good bioactivity, which was also verified by the formation of apatite layer in *in-vitro* testing. Therefore, AAPS deposited HAP/Ti composites are also potential material for load bearing implant materials.

However, oxidation free HAP/Ti coatings could only be achieved under argon environment which makes the process expensive. In contrast, the cold spray technique does not require any protective environment; thus can be an inexpensive approach.

Chapter 1

Introduction

While selecting the material for medical implants, three major factors need to be considered: biocompatibility, osteo-integration and strength [1-3]. Titanium has been widely used for many years as surgical implant materials due to its remarkable corrosion resistance, good biocompatibility and high strength. However, the unlikeliness of formation of a bone-like apatite layer in body environment deteriorates the bonding strength between the titanium implant and the bony tissues and hinders its long-term application as biomedical material [4-7].

Hydroxyapatate (HAP) has received continued attention as biomedical materials to promote accelerated osteo-integration with bone because of its physical and chemical similarities with bone tissues [8-10]. In order to combine the good mechanical properties of Ti based metals with excellent biocompatibility and bioacticity of HAP, various coating techniques such as plasma spraying [11-14], sol-gel processing [2,15], electrical polarization [16], high velocity oxy-fuel (HVOF) spray [17-18] and aerosol deposition [19] have been applied to deposit HAP coating onto Ti or its alloy substrate. However, as a type of bio-ceramic materials, the low ductility of HAP limits its application as load bearing materials. An effective approach to solve this problem is to form a composite coating by reinforcing the HAP coating with a mechanically strong second phase, such as Ti [20], Ti6Al4V [21] and carbon nano-tube [22] et al.

Among various coating techniques, plasma spraying is perhaps the most popularly used technique due to its good chemical composition control and high process efficiency. However, because of high temperature involvement during plasma spraying process, the HAP can be converted into secondary calcium phosphate phases such as tricalcium phosphate (TCP), tetracalcium phosphate (TTCP) or calcium oxide (CaO) and the crystallinity of HAP can also be lowered due to rapid solidification [23-25]. These non-favorable phases and amorphous contents can lead to rapid degeneration and disintegration of the coating and deteriorate the novel biocompatibility of HAP as well as its adhesion to bone. In addition, Ti is easy to be oxidized during plasma spray process, which could also deteriorate the bonding strength between the composite coating and the metallic substrate.

To overcome the above mentioned disadvantages, two novel approaches, namely cold gas dynamic spraying (CGDS) and argon atmosphere plasma spraying (AAPS) techniques were applied to manufacture HAP/titanium composite coating in this study. Cold gas dynamic spraying technique has been developed greatly in recent years [26]. It differs from traditional thermal spray technique in that there is no need for heating the feedstock to be melted or semi-melted before spraying. The feedstock particles are accelerated by ‘cold’, high pressure gas of helium or nitrogen to supersonic speeds through a converging/diverging nozzle and then deposited on a substrate by plastic impact deformation at temperatures generally well below the melting point of the feedstock powder [27,28]. The use of cold deformation in the production of materials reduces the oxide content in deposits and avoids the undesirable phase transfer and thermally induced stress simultaneously [29, 30]. Controlled atmosphere plasma spraying

(CAPS) technique has also been applied to study the deposition of HAP coatings [31, 32]. Advantages similar to cold spray technique are also expected.

In the current study, HAP/Ti composite coatings were successfully fabricated by using in-house developed CGDS and AAPS systems. A systematic investigation was carried out to assess the structural, mechanical, electrochemical properties of deposited composite coatings. The hardness, shear punch and bonding strength tests were conducted to evaluate the mechanical properties. The conventional potentiodynamic polarization technique, Tafel polarization analysis, cyclic voltammetry tests and electrochemical impedance spectroscopy (EIS) were used to evaluate the electrochemical corrosion behavior. The *in-vitro* bioactivity was investigated by immersing composite in simulated body fluid (SBF) solution for a period of time and the formation of bone-like apatite layer was studied by using scanning electron microscope (SEM).

References:

[1]Alexia W.E. Hodgson, Yves Mueller, Dominic Forster, Sannakaisa Virtanen, *Electrochim. Acta* 47 (2002) 1913.

[2] M. Metikos-Hukovic, E. Tkalcecm A. Kwokal, J. Piljac, *Surf. Coat. Technol*. 40 (2003) 165.

[3] S. Tamilselvi, V. Raman, N. Rajendran, *Electrochim. Acta*, 52 (2006) 839.

[4] M. Karthega, S. Nagarajan, N. Rajendran, *Electrochim. Acta*, 55 (2010) 2201.

[5] Shigeru Nishiguchi, Takashi Nakamura, Masahiko Kobayashi, Hyun-Min Kim, Fumiaki Miyaji, Tadashi Kokubo, *Biomaterials* 20 (1999) 491.

[6] Wei-Qi Yan, Takashi Nakamura, Keiichi Kawanabe, Shigeru Nishigochi, Masanori Oka, Tadashi Kokubo, *Biomaterials* 18 (1997) 1185.

[7] C.X. Wang, M. Wang, X. Zhou, *Biomaterials* 24 (2003) 3069.

[8] Byoung-Ki Lim, Fangfang Sun, Su-Chak Ryu, Kwangnak Koh, Dong-Wook Han, Jaebeom Lee, *Biomed. Mater.* 4 (2009) 7.

[9] M Bobby Kannan, Lynnley Orr, *Biomed. Mater.* 6 (2011) 11.

[10] C.Q. Ning, Y. Zhou, *Biomaterials* 23 (2002) 2909.

[11] Z. Zyman, J. Weng, X. Liu, X. Zhang, Z. Ma, *Biomaterials* 14 (1993) 225.

[12] K.A. Khor, P. Cheang, *J. Therm. Spray Technol.* 3 (1994) 45.

[13] E.P. Paschalis, Q. Zhao, B.E. Tucker, S. Mukhopadhayay, J.A. Bearcroft, N.B. Beals, M. Spector, G. H. Nancollas, *J. Biomed. Mater. Res.* 29 (1995) 1499.

[14] Y.C. Tsui, C. Doyle, T.W. Clyne, *Biomaterials* 19 (1998) 2015.

[15] L. -D. Piveteau, M.I. Girona, L. Schlapbach, P. Barboux, J. –P. Boilot, B. Gasser, *J. Mater. Sci. – Mater. Med.* 10 (1999) 161.

[16] Subhadip Bodhak, Susmita Bose, Amit Bandyopadhyay, *Acta Biomater.* 6 (2010) 641.

[17] R.S. Lima, K.A. Khor, H. Li, P. Cheang, B.R. Marple, *Mater. Sci. Eng. A* 396 (2005) 181.

[18] H. Li, K.A. Khor, P. Cheang, *Biomaterials* 23 (2002) 85.

[19] Byung-Dong Hahn, Jung-Min Lee, Dong-Soo Park, Jong-Jin Choi, Jungho Ryu, Woon-Ha Yoon, Byoung-Kuk Lee, Du-Sik Shin, Hyoun-Ee Kim, *Acta Biomater.* 5 (2009) 3205.

[20] Won-Gi Kim, Han-Cheol Choe, *Thin Solid Films* 519 (2011) 7045.

[21] Y.W. Gu, K.A. Khor, P. Cheang, *Biomaterials* 24 (2003) 1603.

[22] Kantesh Balani, Rebecca Anderson, Tapas Laha, Melanie Andara, Jorge Tercero, Eric Crumpler, Arvind Agarwal, *Biomaterials* 28 (2007) 618.

[23] Y.C. Tsui, C. Doyle, T.W. Clyne, *Biomaterials* 19 (1998) 2031.

[24] Shinn-Jyh Ding, Tsui-Hsien Huang, Chia-tze Kao, *Surf. Coat. Technol.* 165 (2003) 248.

[25] Jiyong Chen, J.G.C. Wolke, K. de Groot, *Biomaterials* 15 (1994) 396.

[26] K. Balani, T. Laha, A. Agarwal, J.Karthikeyan, N. Munroe, *Surf. Coat. Technol.* 195 (2005) 272.

[27] Chang-Jiu Li, Wen-Ya Li, *Surf. Coat. Technol.* 167 (2003) 278.

[28] T. Novoselova, P. Fox, R. Morgan, W. O’Neill, *Surf. Coat. Technol.* 200 (2006) 2775.

[29] Wen-Ya Li, Chao Zhang, Xueping Guo, Jinling Xu, Chang-Jiu Li, Hanlin Liao, Christian Coddet, Khiam Aik Khor, *Adv. Eng. Mater.* 9 (2007) 418.

[30] A.C. Hall, D.J. Cook, R.A. Neiser, T.J. Roemer, D.A. Hirschfeld, *J. Therm. Spray Technol.* 15 (2006) 233.

[31] V. Guipont, M. Espanol, F. Borit, N. Llorca-Isern, M. Jeandin, K.A. Khor, P. Cheang, *Mater. Sci. Eng., A* 325 (2002) 9.

[32] S. Beauvais, V. Guipont, F. Borit, M. Jeandin, M. Espanol, K.A. Khor, A. Robission, R. Saenger, *Surf. Coat. Technol.* 183 (2004) 204.

Chapter 2

Literature review

2.1 Cold Spray Technology

The principle of cold spray technology is sketched in Fig.2.1a. Premixed powders were fed by a high pressure powder feeder into pre-heated gas stream through a converging-diverging De Laval type nozzle. In the divergent section of gas expansion, gas and powder are accelerated to supersonic velocity. Different from thermal spraying, bonding in cold spraying occurs due to the high kinetic energy upon particle impact [1,2]. The spraying system adopted in the present study is CGT 4000 system (Fig.2.1b) developed by ASB Industries, Barberton, Ohio.

As mentioned above, the particles must be accelerated to a so called critical speed for successful deposition. Fig.2.2 shows correlation between particle velocity and deposition efficiency [2]. The transition between abrasion in the low velocity range and deposition in the high velocity range defines the critical velocity. Below the critical velocity, the plastic deformation of sprayed powder is not big enough for deposition and the particles just abrade off the substrate like grit blasting. When the velocity is increased to above critical velocity, deposition occurrs and the higher of the particle velocity, the higher the deposition efficiency. The deposition efficiency will reach a saturation limit, which can be close to 100% with further increase in particle velocity [2].

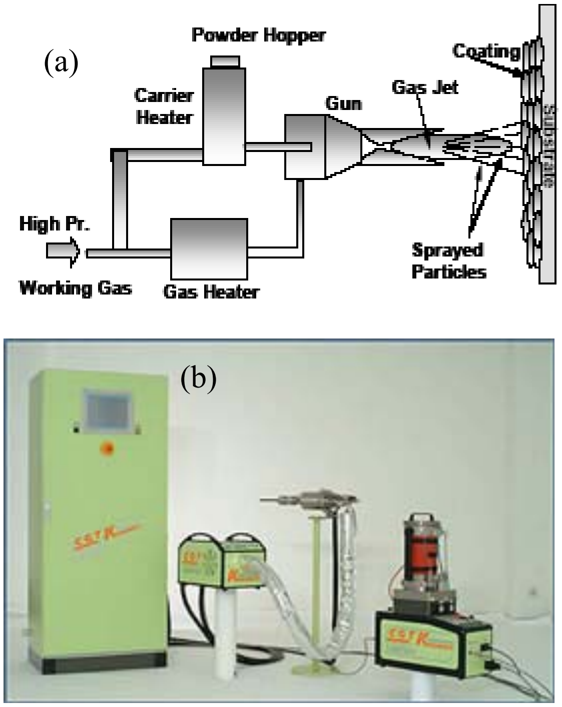

Fig.2.1 (a) Schematic of cold spray process, and
(b) CGT 4000 system used in the present study

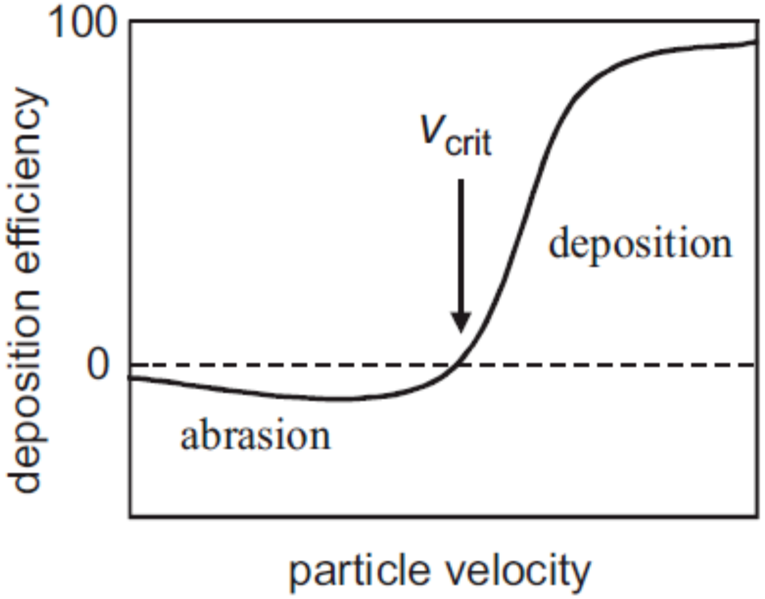

Fig.2.2 Schematic of the correlation between particle velocity and deposition efficiency for cold spraying technology [2].

2.2 Thermal Spray Technology

Thermal spraying involves a group of processes in which surfacing materials are heated to plastic or molten state through the heat source generated by using combustible gases or an electric arc. The molten or semi-molten particles are accelerated and propelled by compressed gas toward the substrate where they strike the substrate's surface, flatten, form thin splats and adhere to the surface and to each other. As the sprayed particles continue impacting on the substrate, a coating is built up [3].

According to the method of heat generation, an academic classification of thermal spraying technique can be obtained. The commonly used thermal spraying techniques in industry include flame spraying (FS), plasma spraying (PS), arc spraying (AS), detonation-gun spraying (D-GUN) and high velocity oxy-fuel (HVOF) spraying. Brief introductions of each of these techniques are presented in the following paragraphs. For plasma spraying, as one of two techniques applied in my research, a detailed description will be given.

As the first invented spraying technique, flame spraying was developed by Swiss engineer Schoop at the beginning of the last century. The chemical energy of combustion of the fuel gas in oxygen is used as heating source and the flame temperature is in the range of 3000 to 3350 K. In arc spraying, two consumable wire electrodes are drawn from spools and fed independently into the gun in which an arc is generated between the two electrodes and the electrodes are heated to form liquid droplets. The droplets are blown by atomizing gas toward the substrate to form a coating. The typical arc temperature can reach as high as 6100 K and the spraying rate is commonly higher than the other thermal spray processes. Detonation-gun basically consists of a long water cooled barrel and with inlet valves for gases and powders. A mixture of oxygen and fuel gas (e.g. acetylene) is fed into the barrel simultaneously with a charge of powder. The mixture gas is ignited by a sprak, explodes and its detonation wave accelerates the powder toward substrate to form a coating. The D-gun process was first developed by Poorman et al. in the early 1950s. High velocity oxy-fuel spraying technique is initially developed near the end of 1970s. It has been developed to produce extremely high spray velocity. The fuel gas or liquid is introduced into the combustion chamber together with oxygen, where they are ignited and combusted continuously. The resultant hot gas is passed through a converging/diverging nozzle and is directed through a long barrel toward the substrate surface to be coated [4,5].

2.3 Plasma Spraying

Plasma is a complex phenomenon. Differing from solid, liquid and gas, it is commonly called “the fourth state of mater” in which a certain portion of particles are ionized. Basically, plasma is an electrically neutrally mixed medium of charged particles (positive ions and negative electrons or ions). Ionization can be induced by several physical phenomena, such as energetic particles colliding, strong electromagnetic field working on bonding electrons or ionizing radiation. These phenomena are usually realized by application of different sources, for example, heating, arcing etc. No matter what kind of method selected, plasma is formed by adding energy to the gas to make the gas atom ionized [6,7].

In plasma spraying, a plasma torch (or plasma gun) is used to generate and direct plasma. In plasma gun, plasma is generated either by direct current (DC) arc or radio frequency discharge (RF). The DC arc is the most commonly used heat source and more than 95% of industrial installations use DC plasma torch. The plasma gun that we adopted in this project is from Thermach, Inc., which is also a DC plasma torch. The plasma gun consists of a circular anode, usually copper and a cathode made of thoriated tungsten. An electric arc is created between the anode and the cathode within the plasma gun. The plasma jet is produced and expanded at atmosphere by passing a plasma gas through the arc which is formed between the tip of the cathode and the wall of the anode. According to the difference of environmental atmosphere, plasma spraying can be divided into three categories: atmospheric plasma spraying (APS), vacuum plasma spraying (VPS) and controlled atmosphere plasma spraying (CAPS). A lab built argon atmospheric plasma spraying system is utilized in this project and the detailed info and spraying parameter will be introduced in Chapter 6 [6-8].

Typically, mixed gases, such Ar+H_2, Ar+N_2 and Ar+He, are used as working gases to form plasma jet. Each gas has its own effect. Ar stabilizes the arc formed inside the gun. H_2, He and N_2 enhance the heat transfer to particles due to their high heat conductivities. The typical temperature in which a plasma gun works is 16,000K and the velocity at the exit of the nozzle can reach 800 m/s [4].

2.4 Bonding Mechanism of Cold Spraying and Plasma Spraying

The mechanism of solid state particles deposit and bond during cold spraying process has been investigated for years. Because of complexity and lack of available characterizing tools, it is still a matter of debate [9]. Although a number of hypotheses have been proposed, extensive plastic deformation is considered the main cause of bonding that takes place in cold spraying. Dykhuizen [10] postulates that when solid state particles impinge on the substrate or deposited particles, they undergoe extensive plastic deformation which could disrupt the thin oxide surface film and, thus, an intimate conformal contact is achieved. The intimate conformal contact which establishes a true metal to metal contact toward the target surface, combined with high contact pressure, promotes bonding [10]. By comparing the results of numerical modeling with experimental results, Gartner et al found that adiabatic shear instabilities at the particle surface occurred at or beyond the critical velocity which is the velocity at which bonding starts forming [11]. The adiabatic shear instabilities is believed to be the result of high strain rate deformation process taking place at the interface and through this deformation process, a metal jet consisting of highly deformed particles and substrate materials is formed [12]. It is the formation of this metal jet make the thin oxide film rupture, create clean interfaces and then a metallurgical bond is created. Besides metallurgical bonding, an additional bonding mechanism, which is termed as mechanical interlocking, is proposed by Hussain et al [13]. It is postulated that when incoming particles impact on the surface, metal jet forms and causes formation of lips of surface material which partially envelop the incoming particles. This creates mechanical interlocking.

A good adherence between molten particles and substrate determines the bonding quality of plasma sprayed coating. A dense and coherent coating ensures protection and bonding strength. When the molten particles impinge onto the substrate, the molten particles lose their kinetic energy and undergo severe deformation. The pressure caused by the sudden deceleration forces the melted material to flow laterally. The substrate stroked by molten particles also undergoes severe plastic deformation. In addition, the heat transfer from sprayed particles to the substrate may cause melting a part of the substrate. Thus, the localized diffusion between the substrate and the molten particles and the local fusion between molten particles and melted substrate cause the formation of metallurgical bonding. The metallurgical bonding has been proposed as one of the mechanisms for bonding of plasma sprayed particles to the substrate [14,15].

2.5 Electrochemical Impedance Spectroscopy Technology [16,17]

Electrochemical impedance spectroscopy (EIS), acknowledged as a modern and efficient evaluation method, is being extensively used in many fields of electrochemistry, e.g. corrosion, electrodeposition, battery, fuel cell. It is one of the linear response methods. The impedance spectrum is measured as a function of frequency of a small-amplitude sinusoidal potential perturbation superimposed on a direct potential bias. Small amplitude perturbations bring two advantages. First, the effects of perturbations on the studied system will be small, which is beneficial to describe the system more accurately. Second, the response of the system will be linear, namely it contains only the first-order terms of the Taylor-expanded non-linear current-voltage relationship, which is beneficial to the analysis of the data.

Fig.2.3 shows a typical electrochemical experiment setup for EIS measurement. In this study, the electrochemical impedance spectroscopy (EIS) measurements were conducted using a Solartron 1255B frequency response analyzer coupled to a 1287 electrochemical potentiostat in conjunction with Zplot software. All measurements were conducted at open-circuit potential (OCP), with an amplitude of 10 mV and at room temperature. The saturated Ag/AgCl electrode was used as the reference electrode.

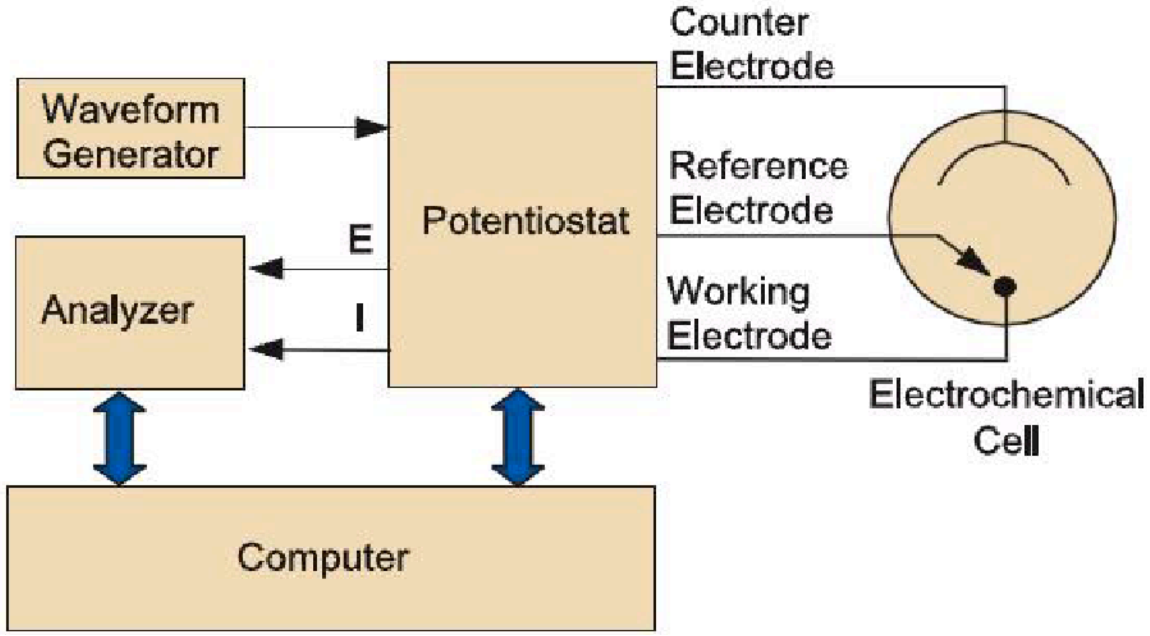

Fig.2.3 Schematic of an electrochemical experiment setup for EIS measurement

In order to answer the question "what circuit would give the same response as the chemical system", equivalent circuit modeling technology was developed by electrochemists. Besides the commonly used electrical circuit elements, some special elements were provided to better explain the electrochemical behavior, e.g. diffusion impedance Warburg (W) and Constant phase element (CPE). In order to develop an equivalent circuit for an electrochemical system, first we need to analyze the nature of the current and potential of the system. Fig.2.4 shows an electrical circuit corresponding to a single reaction on a uniformly accessible electrode. The overall potential equals the potential drop in electrolyte ($R_e i$) plus the potential drop at interface (V). The interfacial impedance (Z_0) is composed of a parallel combination of the Faradic impedance (Z_f) and the double-layer capacitance (C_{dl}), as seen in Fig.2.4b. In the case of single uniform reaction, the Faradic impedance can be represented as a charge transfer resistance.

However for response of coupled reactions involving mass transfer, adsorbing and non-uniform reaction, the representations would be more complicated.

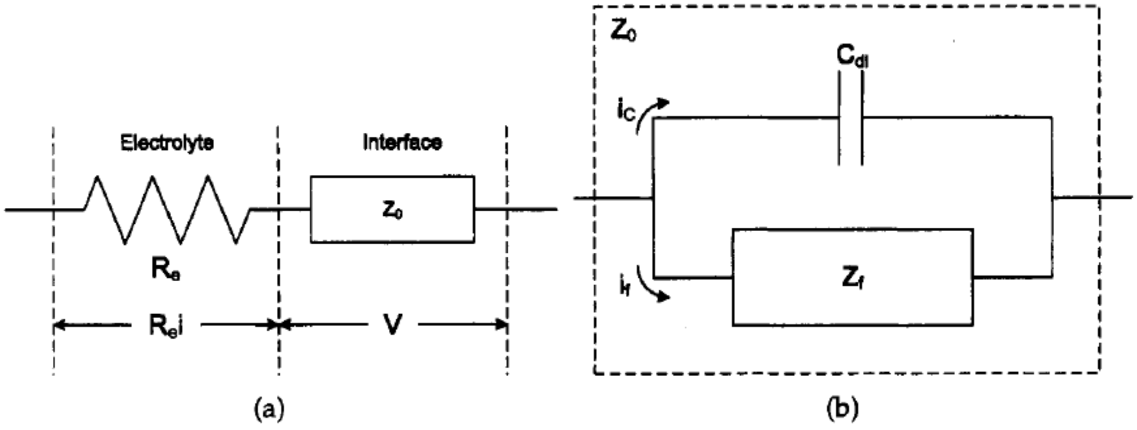

Fig.2.4 Electrical circuit corresponding to a single reaction on a uniformly accessible electrode: a) series combination of the electrolyte resistance and the interfacial impedance; and b) parallel combination of the Faradic impedance and the double-layer capacitance, which comprise the interfacial impedance [16]

The following section derives the overall impedance (Z) of the equivalent circuit in Fig.2.4.

$$Z = R_e + Z_f \, \mathrm{P} Z_c$$

$$Z_{f\mathrm{P}c} = \frac{Z_f Z_c}{Z_f + Z_c} = \frac{R \cdot \dfrac{1}{j\omega C}}{R + \dfrac{1}{j\omega C}} = \frac{R}{1 + j(\omega RC)} = \frac{R}{1 + \omega^2 R^2 C^2} - j\left(\frac{\omega R^2 C}{1 + \omega^2 R^2 C^2}\right)$$

$$Z = R_s + \frac{R}{1 + \omega^2 R^2 C^2} - j\left(\frac{\omega R^2 C}{1 + \omega^2 R^2 C^2}\right) \quad \text{..(1)}$$

From equation (1), it can be concluded that $Z \rightarrow R_s$ as $\omega \rightarrow \infty$ and $Z \rightarrow R_s + R_{ct}$ as $\omega \rightarrow 0$. At very high frequency range, double layer capacitor acts as wire and shortthe R_{ct}. However at very low frequency range, the current can not pass through the double layer capacitor and a series connection between R_e and R_{ct} is formed. Plotting the equation (1) with real part of Z value as X-axis and imaginary part of Z value as Y-axis, a semicircle on the complex plane can be obtained (Fig.2.5). This complex plane plot are also called Nyquist plot.

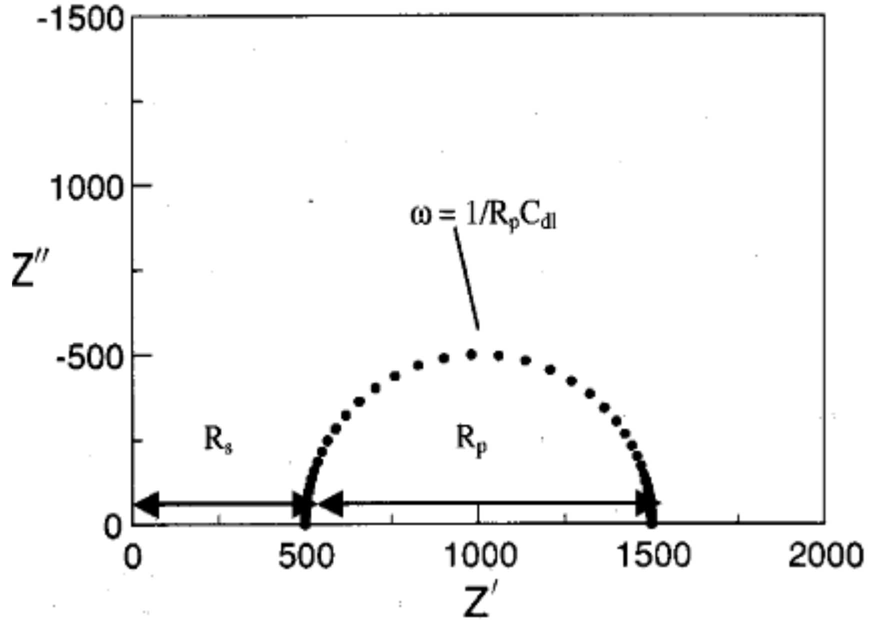

Fig.2.5 Corresponding Nyquist plot for the equivalent circuit shown in Fig.2.4.

Here, R_s represents electrolyte resistance, R_p represents charge transfer resistance and ϖ is the characteristic frequency. The value of the elements of the equivalent circuit can also be extracted by analyzing the Nyquist plot. Thus, based on these values, we can better understand and explain the chemical system.

2.6 Shear Punch Test

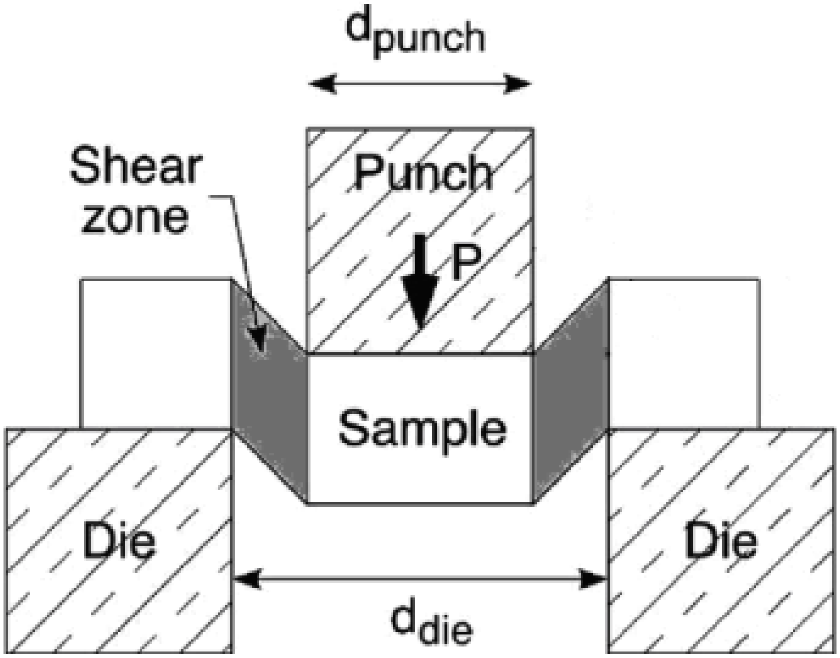

Fig.2.6 Schematic plot of shear punch test

Fig.2.6 shows the schematic plot of shear punch test (SPT). SPT is a small scale specimen testing procedure in which thin disc samples are punched through a die hole while driving the punch at a constant speed. During the process, load on the punch and punch displacement are measured simultaneously. The SPT technique produces the equivalent of a stress-strain curve in shear loading. It is similar to the sheet metal blanking process in which shear deformation occurs combined with some degree of compression, tension and bending.

References:

[1] A. Choudhuri, P.S. Mohanty, J. Karthikeyan, *ASM international* (2009), 391.

[2] F. Gartner, T. Schmidt, T. Stoltenhoff, H. Kreye, *Advanced engineering materials* 8 (2006) No. 7.

[3] AWS Committee on Thermal Spraying, Thermal Spraying-Practice, Theory, and Application, *American Welding Society, INC.*, 1985.

[4] Lech Pawlowski, The Science and Engineering of Thermal Spray Coatings, *John Wiley & Sons, Ltd.*, 2008.

[5] Davis, J. R. (ed.), Handbook of thermal spray technology, *ASM Thermal Spray Society*, Ohio, USA, 2005.

[6] P Fauchais, *J. Phys. D: Appl. Phys.* 37 (2004) 86.

[7] J.Webster (ed.), Thermal spray coating, *John Wiley & Sons, Inc.*, 2007.

[8] Tanya J. Levingstone, BEng, Optimization of plasma sprayed hydroxyapatite coatings, Thesis, *Dublin City University*, Ireland, 2008

[9] M. Grujicic, C.L. Zhao, C. Tong, W.S. DeRosset, D. Helfritch, *Mater. Sci. Eng., A* 368 (2004) 222.

[10] R.C. Dykhuizen, M.F. Smith, *J. Therm. Spray Technol.* 7 (1998) 205.

[11] Hamid Assadi, Frank Gartner, Thorsten Stoltenhoff, Herinrich Kreye, *Acta Materialia* 51 (2003) 4379.

[12] M. Grujicic, C.L. Zhao, W.S. DeRosset, D. Helfritch, *Mater. Des.* 25 (2004) 681.

[13] T. Hussain, D.G. McCartney, P.H. Shipway, D. Zhang, Journal *J. Therm. Spray Technol.* 18 (2009) 364.

[14] S. Dallaire, Influence of temperature on the bonding mechanism of plasma-sprayed coatings, *Metallurgical and protective coatings*, (1982) 237

[15] H.-D. Steffens and M. Mack, *Pure & App. Chem.* 62 (1990) 1801.

[16] Mark E. Orazem, Bernard Tribollet, Electrochemical impedance spectroscopy, *John Wiley & Sons, INC.*, 2008

[17] Robert S Rodgers, An introduction to electrochemical impedance spectroscopy (EIS), *ACS Princeton Local Section*, 2009

Chapter 3

Study of High-Frequency Artifacts in EIS Measurements of Ti and Its Alloys in Simulated Body Fluid

3.1 Abstract

In electrochemical impedance spectroscopy which is commonly used to study the behavior of titanium and its alloy in simulated body fluid solution, high frequency artifacts are commonly observed. Two parameters that may augment the high frequency artifacts including the electrochemical cell design and the solution are investigated in this environment. The results suggest that the luggin capillary design of the cell can be the main reason responsible for high frequency artifacts. In order to reduce the effect of high frequency artifacts, two cell modification methods including use of auxiliary platinum wire and by-pass circuit, were selected. Both methods can greatly reduce the high frequency artifacts, but both methods increase the complexity of experiments. In addition, increasing the solution conductivity can reduce the artifacts in high frequency region too.

3.2 Introduction

Titanium and its alloy Ti6Al4V have been widely used for many years as surgical implant materials due to their remarkable corrosion resistance, good biocompatibility and high mechanical strength [1, 2]. Electrochemical impedance spectroscopy (EIS), acknowledged as a modern and efficient evaluation method, are being extensively used to study the corrosion properties of titanium based implant materials [3-8]. However, high frequency range artifacts, which are considered unavoidable in electrochemical impedance measurements in a three-terminal cell [9], have not received enough attention particularly in the case of simulated body fluids. And it is perceived that there are three variables that contribute to these high-frequency artifacts: the potentiostat, the electrochemical cell and the solution itself [10]. This chapter deals with the study of high-frequency artifacts of Ti and its alloys Ti6Al4V in simulated body fluid (SBF). The effect of the electrochemical cell design and the solution resistance on high-frequency artifacts has been investigated.

3.3 Materials and Method

3.3.1 Samples Preparation

Five types of samples (polished, unpolished titanium; polished, unpolished Ti_6Al_4V alloys; Plasma sprayed TiO_2 coating on titanium substrate) were prepared before EIS measurement. For polishing process, commercially available titanium and Ti_6Al_4V plates were polished progressively with SiC papers of grit 240, 400, 600, 800, 1000 and 1-μm diamond paste. For plasma spraying process, titanium substrates were grit blasted using alumina, then TiO_2 coatings with a thickness of 50±10 μm were plasma sprayed on titanium substrates.

3.3.2 Simulated Body Fluid

In order to study the effect of solution on EIS measurements, three solutions were selected: Hanks' solution, NaCl solution and Hanks' + NaCl solution, shown in Table 3.1. Two kinds of Hank's balanced salt solution were purchased from Mediatech Inc. One is with calcium, magnesium, and phenol red. The other is without calcium, magnesium, and phenol red. The chemical composition of Hanks' solution is given in Table 3.2. Different concentration of NaCl solutions were prepared as shown in Table 3.1. Hanks' + NaCl solution was prepared by dissolving commercial NaCl (>99.5%) in Hanks' solution without calcium, magnesium and phenol red. The NaCl concentration of the new solution was 2.7 wt%.

Table 3.1 Simulated Body Fluid Solution Types of Testing

Hanks'	With calcium, magnesium, & phenol red			Without calcium, magnesium, & phenol red	
NaCl (wt%)	0.9	2.7	3.5	6.3	9
Hanks' + NaCl	Hanks' + 2.7% NaCl				

Table 3.2 Chemical Composition of Hank's Solution

Hanks' solution	With calcium, magnesium and phenol red	Without calcium, magnesium and phenol red
Concentration	g/L	g/L
NaCl	8.00	8.00
KCl	0.40	0.40
$CaCl_2$(anhydrous)	0.14	—
$NaHCO_3$	0.35	0.35
Na_2HPO_4(anhydrous)	0.0477	0.0477
$MgSO_4$(anhydrous)	0.0977	—
KH_2PO_4	0.06	0.06
D-Glucose	1.00	1.00
Phenol red, Na	0.01	—
PH (final)	7.1 - 7.4	7.25 ±0.15

3.3.3 Electrochemical Cell

Electrochemical cell, including the geometry, reference electrode, wiring, and connections, is a variable that can contribute to the high-frequency artifacts and should not be ignored [11]. In this work, three types of commercially available three-electrode electrochemical cell were tested: Gamry PTC1 Paint Test Cell, Gamry CCK Corrosion Cell Kit and Princeton Applied Research K0235 Flat Cell. The schematic diagrams of these three cells are shown in Figs.3.1 to 3.3 respectively. They all use Ag/AgCl electrode as reference electrode. Paint cell and flat cell are designed to test samples with flat surface. However, CCK corrosion cell is designed to test cylindrical samples. Another difference is that flat cell and CCK corrosion cell have luggin capillary design but paint cell does not have a luggin capillary.

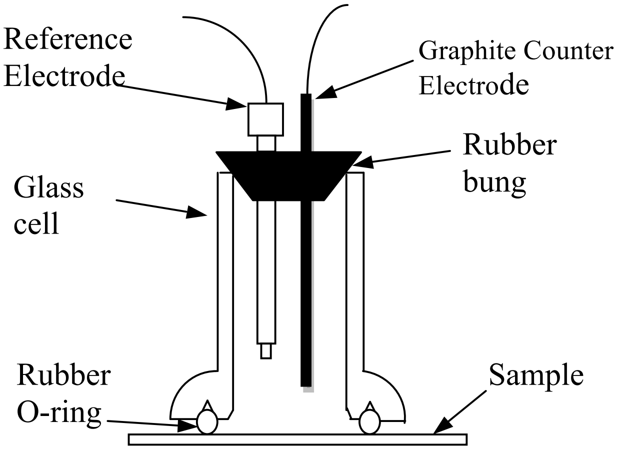

Fig.3.1 Sketch of Gamry PTC1 Paint Test Cell

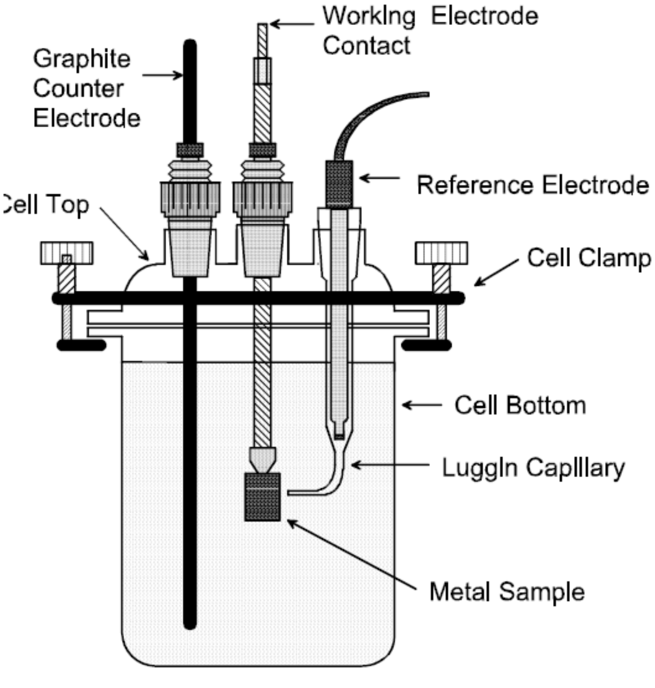

Fig.3.2 Sketch of Gamry CCK Corrosion Cell Kit

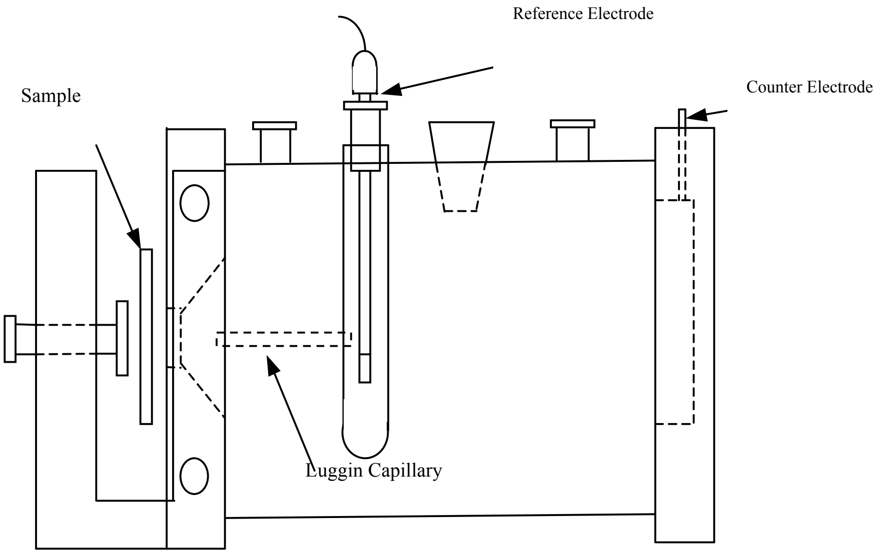

Fig.3.3 Exploded View of Model K0235 Flat Cell

3.3.4 Electrochemical Impedance Spectroscopy (EIS)

The electrochemical impedance spectroscopy (EIS) measurements were conducted using a Solartron 1255B frequency response analyzer coupled to a 1287 electrochemical interface in conjunction with Zplot software. All measurements were conducted at open-circuit potential (OCP), with an amplitude of 10 mV and at room temperature. The range of measured frequency extended from 0.01 Hz to 100 KHz, with a logarithmic sweep of 6 points per decade. Data acquisition was performed on an interfaced computer with the aid of Zplot software. The spectral fitting were conducted by using the complex nonlinear least square (CNLS) method which was developed by Boukamp[12], with the aid of Zview software. For K0235 Flat Cell, a platinum foil was used as counter electrode and for the other two cells, the graphite rods were selected as counter electrodes. The saturated Ag/AgCl electrode was used as reference electrode for all three cells. The exposed surface area for K0235 flat cell and PTC1 paint test cell was 1 cm^2; for CCK corrosion cell, it was 3.8 cm^2.

3.4 Results and Discussion

3.4.1 EIS of Ti and Ti_6Al_4V Alloy in Simulated Body Fluid Solution

Generally, the impedance spectra can be divided to three frequency regions: high, intermediate and low regions. In the high frequency region ($f > 10^4$ Hz), the |Z| value exhibits plateau behavior, and the phase angle approaches 0, which yields the value of solution resistance, Rs. The Rs value is affected by the following parameters: electrolyte resistance, cell geometry, impedance of the conductors and the reference electrode. In the low frequency region (f <10 Hz), these electrochemical processes are detected including electron charge transfer process, the mass transfer (diffusion or migration) process, and other relaxation processes taking place at the film-electrolyte interface or within the pores of the surface film. The intermediate frequency region (10 to 10^3 Hz) has the maximum phase angle with the log|Z| vs. log$f$ slope approaching -1, which corresponds to the capacitive behavior of the electrode and the dielectric properties of the electronically conducting surface film [13].

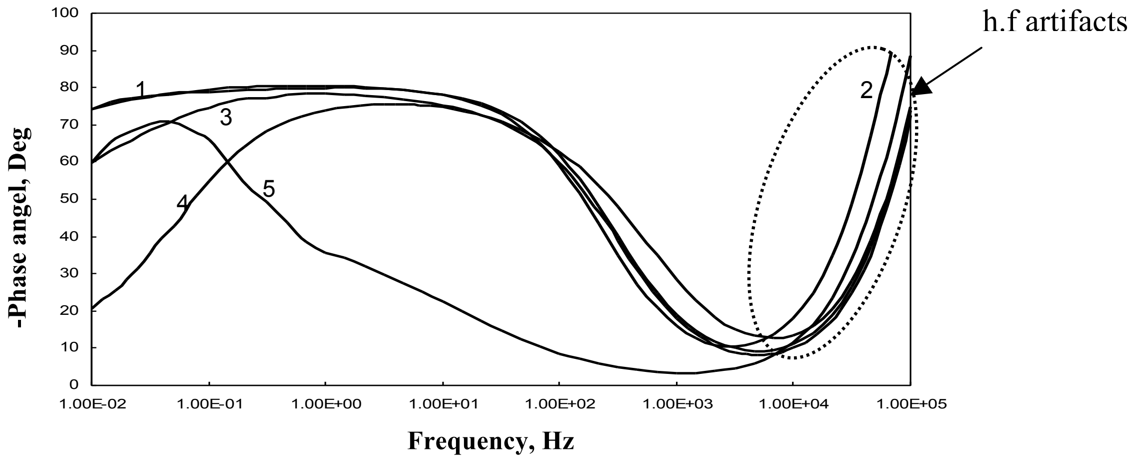

Fig.3.4 Impedance Bode plot showing the high frequency artifacts. 1,Ti6Al4V in Hank's I; 2, Ti6Al4V in Hank's II; 3, Ti6Al4V in 0.9wt% NaCl; 4, Polished Ti in Hank's I; 5, Plasma sprayed TiO2 on Ti substrate in Hank's I.

Fig.3.4 shows the high frequency artifacts in different solutions in K0235 flat cell. Irrespective of the material (Ti, Ti6Al4V or TiO2 coating on Ti substrate), as well as the solutions (Hank's solution or NaCl solution), the phase angles at high frequency range go up instead of approaching 0 degree, which is contrary to the theory discussed above. This suggests that the obtained impedance data at high frequency region beyond 10K Hz are artifacts and in the current system, the high-frequency artifacts always appeared and were unavoidable. Fig.3.5 shows the high frequency artifacts in a corresponding Nyquist plot in detail. The artifacts show a curved line which can be considered as part of the semi-circle. If we complete the semi-circle by drawing it along the artifact, the intersection with X axis will be in the second quadrant and has a negative value. The electrolyte resistance is always positive and can not be negative. Again this proves that these data are artifacts.

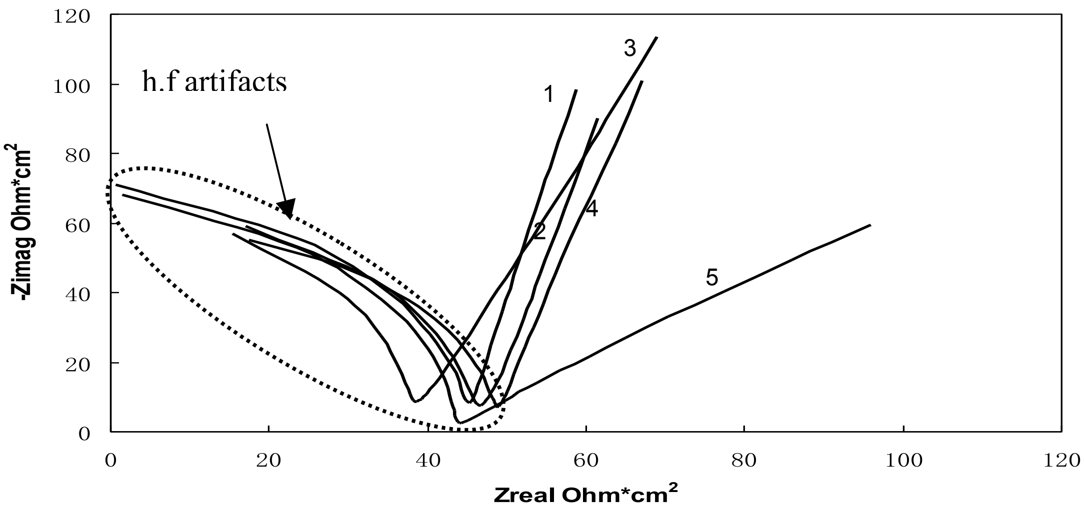

Fig.3.5 High frequency artifacts in corresponding Nyquist plot in different situation.1,Ti6Al4V in Hank's I; 2, Ti6Al4V in Hank's II; 3, Ti6Al4V in 0.9wt% NaCl; 4, Polished Ti in Hank's I; 5, Plasma sprayed TiO2 on Ti substrate in Hank's I

3.4.2 The Effects of Electrochemical Cell

Fig.3.6 shows the high frequency artifacts comparison of three different cells. The phase angle goes up around 10K Hz for both Flat Cell and CCK Cell Kit. But for Paint cell, the phase angle is close to zero degree. This indicates that a relatively larger frequency range can be measured by using Paint cell. However, because of no capillary design is included in the Paint cell, relatively higher Ohmic drop will be expected. The corresponding high frequency artifacts in Nyquist are also shown in Fig.11. The high frequency artifacts are absent in the measurement done in the Paint cell. It is to be noted that the reason for difference in low frequency range spectrum tested in CCK cell with the other two cells is due to relatively porous surface of the titanium rod used in this cell compared to Ti6Al4V plate tested by the other two cells.

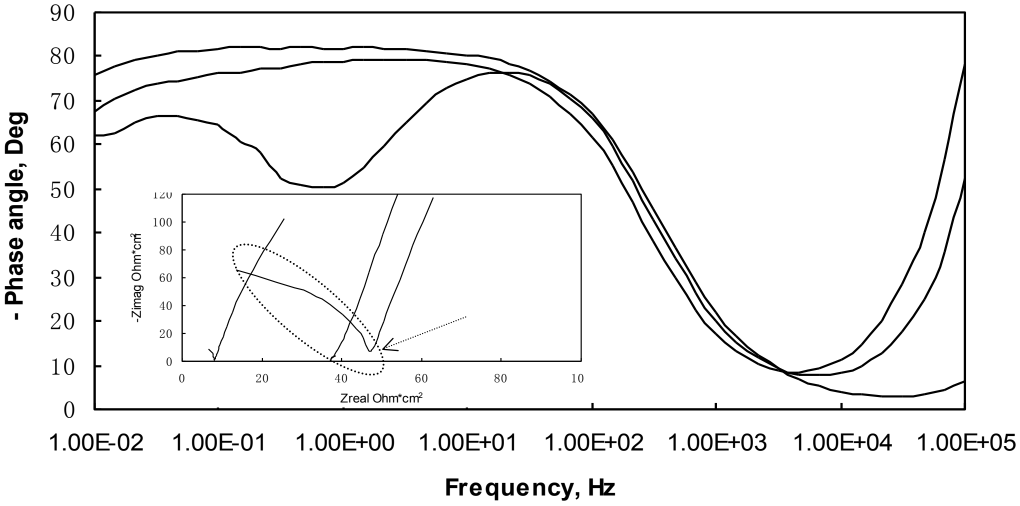

Fig.3.6 High frequency artifacts comparison for three different Cells

3.4.3 The Effects of Solution Conductivity

In order to better understand the impedance artifacts in high frequency range, sets of experiments were conducted in K0235 flat cell by changing the solution conductivity. The results are shown in Fig.3.7. It is seen that as the solution concentration increased, the phase angle dropped continuously reaching zero degree and high frequency artifacts totally disappeared (Nyquist plot inset of Fig.3.7). The biggest change happened when the solution concentration was increased from 0.9wt% to 2.7wt%.This suggests that the artifacts at high frequency range can be eliminated by increasing solution conductivity. Additionally the testing frequency range is enlarged simultaneously with the increasing of solution conductivity, which means more valuable information can be obtained in higher frequency range. However increasing the solution conductivity becomes impractical as it deviates from body fluid characteristics.

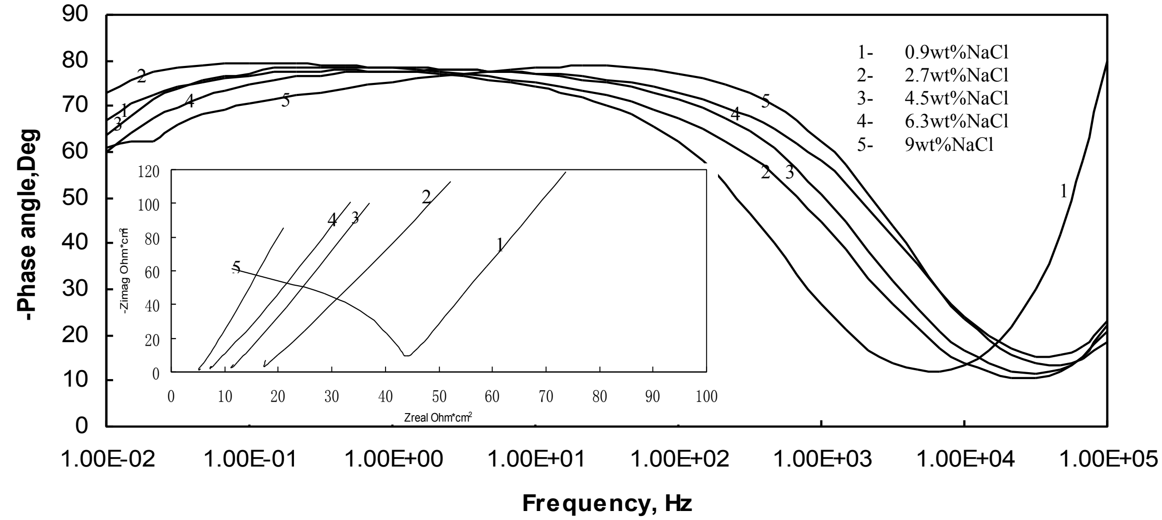

Fig.3.7 Impedance spectra of Ti6Al4V alloy exposed to NaCl solution with different solution concentration in K0235 Flat Cell.

3.4.4 Use of Auxiliary Platinum Wire and By-pass Circuit

In order to minimize the effects of the high frequency artifacts, two methods were adopted. One is inserting a platinum wire in the luggin capillary tube of the Flat Cell. The other is the use of a by-pass circuit, namely adding a 470pF capacitor in parallel with reference electrode. Fig.3.8 presents the comparison of impedance spectra with and without use of these two methods. It is seen that the high frequency artifacts are greatly reduced at high frequency range by these two methods and the phase angle already approaches to zero degree at 50k Hz by using a by-pass circuit. However, it is also seen that the impedance data in middle and low frequency range are affected by these two methods. This suggests that although both methods can reduce the high frequency artifacts, but the uncertainty of experiment is increased simultaneously and both methods increase the complexity of experiments.

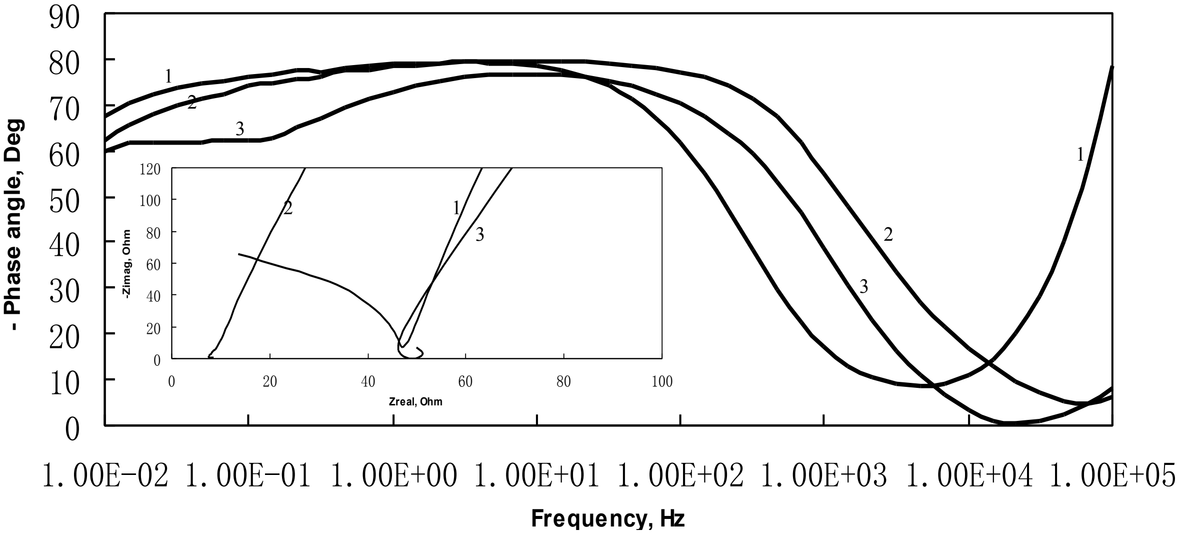

Fig.3.8 Minimizing the high frequency artifacts by use of auxiliary platinum wire and by-pass circuit methods: 1. without cell modification 2; Insertion of a platinum wire in the luggin capillary tube; 3. Insertion of a 470pF by-pass circuit

3.4.5 Effects of Deleting the High Frequency Range Data

Alternatively, if we select 10K Hz as frequency range limitation, and delete the high frequency artifacts, will it affect the results of the equivalent circuit? Fig.3.9 is the fitted Bode Impedance spectra of non-polished Ti6Al4V alloy immersed in Hank's solution. Fig.3.10 presents the determined equivalent circuit-double layer model. Here, we use a constant phase element (CPE1) combined with a resistance (R1) to simulate the high frequency artifacts.

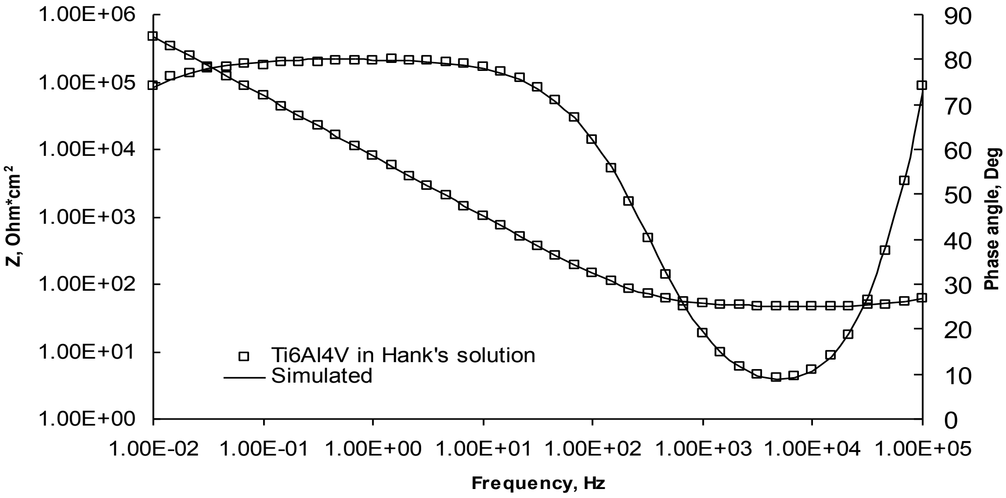

Fig.3.9 Fitted Bode Impedance spectra of Ti6Al4V alloy exposed to Hank I in K0235 flat cell.

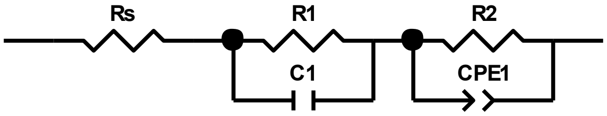

Fig.3.10 Equivalent circuit used to simulate impedance spectra of Ti6Al4V alloy exposed to Hank I in K0235 flat cell.

After deleting the high frequency range data (>10K Hz), the fitted Bode impedance spectra and equivalent circuit are shown in Fig.3.11 and 3.12. The EIS spectra fitting results of the original and after deleting high frequency artifacts are listed in Table 3.3. Here, CPE2 stands for the double layer capacitance and R2 stands for the charge transfer resistance. It is seen that the value of these two elements does not change much after deleting the high frequency artifacts. This result suggests that one can ignore the high frequency artifacts when equivalent circuit method is used to analyze impedance spectra data. In addition, after deleting the high frequency artifacts, the R1 (stands for electrolyte resistance) value changed from -103.3 to 46.34 ohm. In the application of impedance spectra to electrochemical systems, the electrolyte resistance is usually considered as high-frequency limit. When K0235 Flat Cell is used in simulated body fluid system, in order to obtain meaningful electrolyte resistance, the high-frequency limit should be set around 10K Hz.

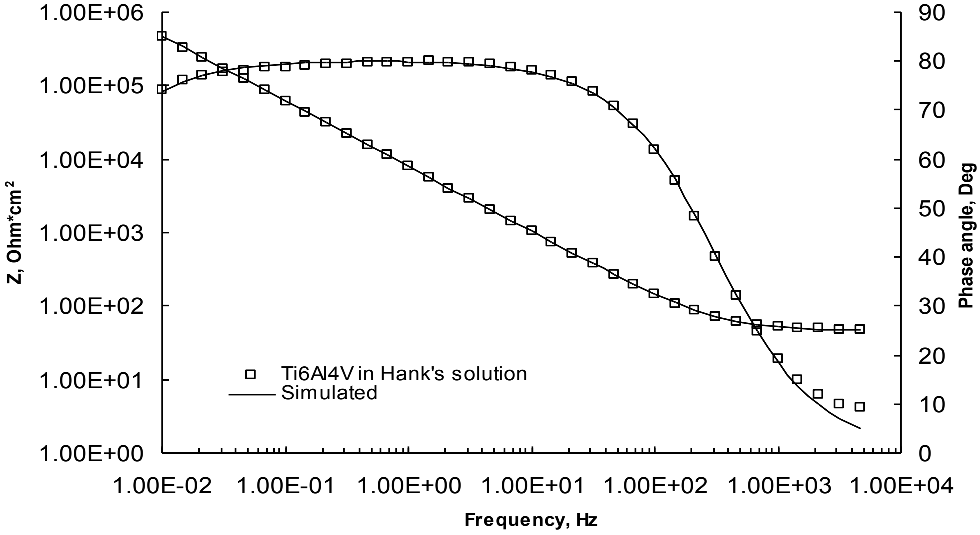

Fig.3.11 Fitted Bode Impedance spectra of Ti6Al4V alloy exposed to Hank I in K0235 flat cell, after deleting high frequency range data

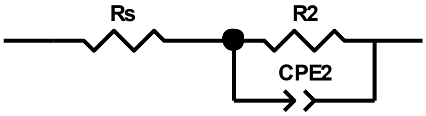

Fig.3.12 Equivalent circuit used to simulate impedance spectra of Ti6Al4V alloy exposed to Hank I in K0235 flat cell, after deleting high frequency range data

Table.3.3 Comparison of EIS spectra fitting results of original and after deleting high frequency artifacts

EEC	Rs (Ω)	C1(Fcm^{-2})	R1 (Ω)	CPE2 (Fcm^{-2})	n^2	R2 (Ω cm^2)
Two	-103.3	5.02E-9	149.5	2.44E-5	0.89	4.0082
One	46.34			2.43E-5	0.89	4.0806

3.5 Conclusions

Electrochemical impedance analysis is a very useful technique for studying corrosion behavior of surgical implant materials, but in simulated body fluid solution, the high frequency artifacts are unavoidable and need attention. Although increasing the solution conductivity can reduce the artifacts at high frequency region, the approach is impractical as it deviates from body fluid characteristics. In order to reduce the high frequency phase shifts, both auxiliary platinum wire and by-pass circuit methods can be used, but both methods increase the complexity of experiments.

In addition, based on above discussion, it is concluded that when the K0235 flat cell is used, it is safe to delete the high frequency data (beyond 10 kHz), which wouldn’t change the results much. Thus the flat cell is used in the following study to evaluate the electrochemical corrosion behavior.

References:

[1] Alexia W.E. Hodgson, Yves Mueller, Dominic Forster, Sannakaisa Virtanen, *Electrochim. Acta* 47 (2002) 1847.

[2] M. Metikos-Hukovic, E. Tkalcecm A. Kwokal, J. Piljac, *Surf. Coat. Technol.* 165, (2003) 40.

[3] Neluta Ibris, Julia Claudia, Mirza Rosca*, J. Electroanal. Chem.* 526 (2002) 53.

[4] Niki J. Kouloumbi, Stavros T. Kyvelidis, *Mikrochim. Acta* 136 (2001) 175.

[5] D. Starosvetsky, I. Gotman, *Surf. Coat. Technol.* 148 (2001) 268.

[6] C.X. Wang, M. Wang, X. Zhou, *Biomaterials* 24 (2003) 3069.

[7] Zhongping Yao, Zhaohua Jiang, Fuping Wang, *Electrochim. Acta,* 52 (2007) 4539.

[8] Ricardo M. Souto, Maria M. Laz, Rui L. Reis, *Biomaterials* 24 (2003) 4213.

[9] S. Fletcher, *Elctrochem. Commun.* 3 (2001) 692

[10] Johan R. Scully, David C. Silverman, Martin W. Kendig, Editors, Electrochemical Impedance: Analysis and Interpretation, *ASTM special technical publication*, (1993) 77.

[11] Gamry CCK Corrosion Cell Kit Operator's Manual, *Gamry Instruments, Inc.*,(1994)

[12] Bernard A. Boukamp, *Solid State Ionics* 20 (1986) 31

[13] S. Tamilselvi, V. Raman, N. Rajendran, *Electrochim. Acta* 52 (2006) 839.

Chapter 4

Corrosion Behavior of Cold Sprayed Titanium Coatings in Simulated Body Fluid

4.1 Abstract

A composite structure comprising high strength titanium (Ti) alloy core and a high surface area pure Ti coating can be ideal for implant applications. In this work, the corrosion behavior of pure Ti coatings composed of porous top layer (~100 μm) and dense bottom layer (~500 μm) obtained by cold spray method has been investigated. The porous top layer satisfies the high surface area requirement for the implant and the dense bottom layer ensures a good corrosion protection of the substrate and also good bond strength. In order to further improve the corrosion and mechanical property of cold sprayed Ti coatings, heat treatment (850 ^{o}C for 5 h) was applied. Electrochemical potentiodynamic and electrochemical impedance spectroscopy (EIS) measurements were used to characterize the electrochemical corrosion behavior of the cold sprayed Ti coatings in Hanks' solution. For comparison, the corrosion and mechanical properties of annealed and un-annealed wrought Ti substrates were also investigated. Our results showed that the as-sprayed Ti coatings exhibited a relatively low corrosion resistance than the pure Ti substrate. However, post spray heat treatment improved the corrosion resistance to a level close to that of the bulk material. Further, EIS studies

revealed that the newly formed dense and structurally stable oxide layer on the surface of the coating during potentiodynamic scanning was beneficial to the corrosion behavior.

4.2 Introduction

While selecting the material for medical implants, three major factors need to be considered: biocompatibility, osseointegration and mechanical strength [1-3]. Corrosion resistance of an implant to body fluid can be improved by creating a corrosion resistant barrier layer on it [4]. Further, by creating a rough or porous layer on the implant, osseointegration can be enhanced due to increased surface area [5]. Titanium alloys exhibit very good mechanical strength but relatively low corrosion resistance compared to pure titanium. For example, any dissolution of aluminum and vanadium ions from the commonly used Ti6Al4V alloy may result in toxicity effects [6-9]. In order to combine good mechanical property of Ti6Al4V and good corrosion property of titanium, thermal spray methods (e.g., plasma spray) have been used to produce titanium barrier coatings on Ti6Al4V alloys [10]. Although porous Ti coatings with high surface area can be achieved by plasma spray method [11], the elevated processing temperatures, unless carried out under inert environment, result in oxidation of Ti as well as associated thermal residual stress. Further, plasma spray does not create a metallurgical bonding with the substrate. These effects can lead to degradation and detachment of Ti coatings from the metallic substrate. Cold spray, on the other hand, can be a suitable alternative and mitigate the problems associated with plasma spray. Since its first invention in middle 1980s, cold gas dynamic spray (CGDS) technique has rapidly found many applications in recent years [12]. It differs from traditional thermal spray technique in that there is no need for heating the feedstock to be melted or semi-melted before spraying.

The feedstock particles are accelerated by high pressure gas of helium or nitrogen to supersonic speeds through a converging/diverging nozzle and then deposited on a substrate by plastic fusion at temperatures generally well below the melting point of the feedstock powder [13,14]. The low temperature processing environment reduces the oxide content in the deposits and avoids the undesirable phase change and thermally induced stress, which makes cold gas dynamic spray a very attractive technique for many applications [15, 16].

Recent advances on cold sprayed Ti coatings include studies on fatigue behavior by Price et al. [17], and influence of post spray heat treatment on microstructure and mechanical properties carried out by Li et al [15, 18,19]. Also, Hussain et al. [20] studied the role of porosity on the corrosion behavior in salt water of both free standing Ti deposits and coatings, while corrosion behavior of the coatings in seawater has been investigated by Wang et al. [21]. However, most of these studies are focused on producing a dense coating to improve its corrosion property as a barrier layer. The potential applications of cold sprayed Ti coatings in biomedical applications have not received much attention so far.

In our previous work [22], cold sprayed Ti coatings composed of two distinct layers (a top porous layer with variable porosity and a dense bottom layer) have been successfully achieved. The objective of the present work is to study the *in-vitro* corrosion behavior of cold sprayed Ti coatings in Hanks' solution and to evaluate their suitability for biomedical applications. The conventional potentiodynamic polarization technique as well as electrochemical impedance spectroscopy have been used to test the electrochemical corrosion characteristics. In addition, post-spray heat treatment has been applied to modify the microstructure and other properties of cold sprayed coatings. The corrosion behavior of oxide layer formed during potentiodynamic polarization process was further studied by electrochemical impedance measurements. Also, the role of oxide layer as a potentially useful protective layer in biomedical applications is highlighted.

4.3 Experimental Details

4.3.1 Deposition of Coatings and Heat Treatment

Commercially available pure wrought titanium sheet (98.9%, from Mcmaster-Carr Co, USA) was used as the substrate. Rectangular Ti coupons, 50×36×3 mm^3, cut from sheet materials, were grit blasted with Al_2O_3 particles (36 meshes) and ultrasonically cleaned in acetone for 10 min before cold spraying. The spray powder was commercial titanium sponge powder (Accushape Inc.USA) with 325 mesh size. A commercial cold spray (Kinetic 400, CGT, Germany) as well as an in-house developed system was utilized to fabricate Ti coatings under optimized spray parameters listed in Table 4.1. Coating thickness for all samples was about 600 μm. The basic schemes of the cold spray process and other information are described in literature [12, 28-30]. After spraying, some samples were annealed at 850^oC for 5 hrs in Argon with 5% hydrogen atmosphere. The pure wrought titanium samples were also annealed under the same conditions for comparison.

Table 4.1 Cold spray deposition parameters

Substrate	Ti
Powder	Ti sponge powder
Spray distance	15 mm
Powder feed	2 RPM
Carrier gas flow	4 m^3/h
Pressure	35 Bar
Temperature	500 ^oC
Gas type	N_2

4.3.2 Microstructural Characterization and Microhardness Studies

The characteristics of powders and cross-sections of coatings were examined using an optical microscope (Nikon Eclipse LV100) as well as a scanning electron microscope (HITACHI S-2600N SEM). The coatings were cut perpendicular to the coating-substrate interface, hot-mounted, and then polished progressively (down to 1200 SiC paper grit). The final polishing procedure was performed using colloidal silica with a particle size of 0.04 μm. The samples were washed in running water and ultrasonically cleaned with acetone. The samples were etched by swabbing the samples with an etchant of 91% H_2O, 3% HF and 6% HNO_3. The phase composition of coatings was determined by a RIGAKU MINIFLEX XRD system using Cu K_α. The X-ray data were collected in the 2 θ range of 30-90° in steps of 0.02°. A Future-Tech, type FM microhardness tester was used to measure microhardness. The microhardness measurements were performed on the cross section of the sprayed deposit with a load of 100 gf applied for a dwell time of 10 s.

4.3.3 Electrochemical Corrosion Studies

The electrochemical measurements were carried out using a flat three-electrode cell (K0235 Flat Cell, Princeton Applied Research), with the samples acting as the working electrode, a silver/silver chloride electrode as the reference electrode and a platinum grid as the counter electrode. The specimen area exposed to the electrolyte solution was 1 cm^2. A commercially available simulated body fluid solution (SBF), Hank's balanced salt solution with pH = 7.25 ±0.15 [composition, NaCl: 8 g/L, KCl : 0.4 g/L, $NaHCO_3$: 0.35 g/L, Na_2HPO_4 (anhydrous) : 0.0477 g/L, KH_2PO_4 : 0.06 g/L and D-Glucose : 1g/L] was used as the electrolyte solution.

Potentiodynamic polarization curves were determined by using a Solartron SI 1287 potentiostat and electrochemical impedance spectra were recorded with a Solartron 1255B frequency response analyzer. Prior to each measurement, all samples (as-received Ti coatings, annealed Ti coatings, pure Ti substrates and annealed pure Ti substrates) were polished progressively until a mirror finish surface was achieved. In order to avoid the possible oxidation of samples, the electrochemical tests were commenced immediately after immersion of the samples in Hank's solution. All the experiments were carried out at least three times under ambient temperature.

For potentiodynamic polarization studies, the working electrodes were polarized from -1 V (Vs. reference electrode potential) to +5 V at a scan rate of 1 mV/s. CorrWare software was used to determine the corrosion potential (Ecorr), corrosion current (Icorr) and polarization resistance (Rp). For electrochemical impedance spectroscopy, measurements were conducted at open-circuit potential (OCP), with the amplitude of sinusoidal signal set at 10 mV. The range of measured frequency extended from 0.01 Hz to 10 kHz, with a logarithmic sweep of six points per decade. The impedance data at higher frequency range was not recorded due to artifacts that become significant beyond 10kHz in a low conductive solution like the SBF [31]. But one can ignore the high frequency artifacts in constructing the equivalent circuit without changing the surface film parameters considerably. This issue will be discussed further, later in this chapter. The recorded impedance spectra were fitted using the complex nonlinear least square (CNLS) method which was developed by Boukamp [32], with the aid of Zview software. After polarization, the electrochemical impedance spectroscopy studies were also conducted again to investigate the possible characteristic changes of the sample surface. This was done following a delay period of one hour in order to stabilize the open circuit potential.

4.4 Results and Discussion

4.4.1 Microstructual Characterization

The typical morphology of titanium sponge powder used for deposition of coatings in this thesis is shown in Fig.4.1. Two different shapes of particles are visible; relatively large elongated particles mixed with porous spongy clusters formed by small particles (Fig. 4.1(a)). In order to study the internal structure of the particles, the Ti sponge powder was hot-mounted, polished and etched, and the structure is shown in Fig. 4.1(b). Although the biggest elongated particles have a size close to 100 μm and the small ones have a size in a range of 10-30 μm. Structurally, the two types of particles are essentially the same, i.e., both have an internal porous structure with pore size ~1.5 μm.

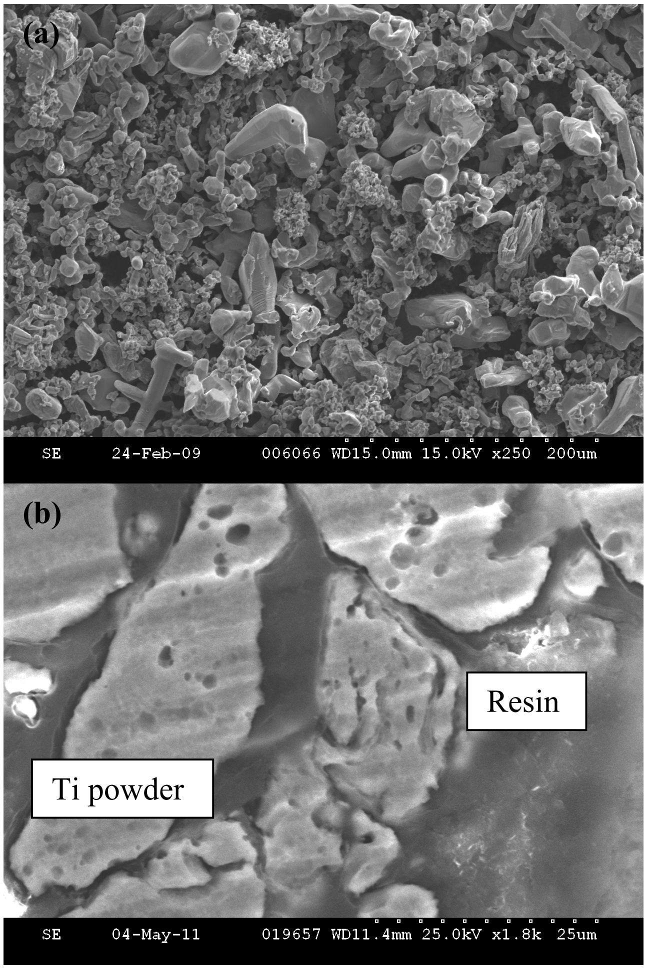

Fig.4.1 SEM images of Ti sponge powder for
(a) surface image and (b) cross-section image.

In our earlier study, we have demonstrated the influence of particle morphology on the resulting cold sprayed coating structures. The above mentioned sponge powder provides a greater flexibility in terms of controlling the coating structures, i.e, very dense to porous. Examining the coating structure shown in Fig. 4.2(a), it is observed that the top surface layer of the coating is relatively porous compared to the bottom layer. Both porous top layer and the internal porous structure of sponge powder can provide the anchoring sites and thus enhance osseointergration. Dense bottom layer ensures a good bonding between the coating and the substrate. The optimal porosity for tissue integration has not been determined yet in the literature. However, too large porosity may adversely affect the cell growth between the implant and the bone. The cold sprayed Ti coating with small porosity on top layer might be a potential candidate for biomedical applications. The detailed morphology of as-received Ti coating after etching is shown in Fig. 4.2(b). The splat structure of sprayed coatings resembles the initial particle shapes. This is in spite of the fact that titanium sponge powder experienced significant deformation during cold spray process. Although particle to particle mechanical interlocking is apparent in the coating, metallurgical bonding was also observed at some particle-particle interfaces and particle-substrate interfaces (marked by the arrows) due to cold welding phenomenon. Some incomplete interfacial fusion and submicron pores are visible in the etched surface. The incomplete interfacial defects resulted from the attack of particle boundaries by the etchant and the submicron pores resembled the internal porous structure of sponge powder. After annealing, it was found that some contact interfaces between the deposited particles, interfaces between particles and substrate disappeared through the atomic diffusion and grain boundary migration (marked by arrow in Fig. 4.2(c)). The metallurgical bonding to the substrate improved further after annealing. A higher bonding strength can be anticipated due to these changes. It was also observed that big pores and cracks in Fig. 4.2(b) were converted into smaller ones (Fig. 4.2(c)) during the annealing process. It is to be noted that the cold sprayed coating is highly strained due to the inherent mechanical deformation associated with the process. A better corrosion behavior could result from strain relief induced by the annealing process. Fine grains were observed in the coating microstructure after the annealing step (Fig. 4.3(c)). This observation indicates that the material experienced nucleation and recrystallization during the annealing process and improved metallurgical bonding between deposited particles was obtained. But unlike the bulk material (Fig. 4.3(a)), grains do not grow thoroughly and grain boundary is not well defined at some places of the coating. This is possibly related to the preexisting surface oxide layers in the as received powder, which prevent the grain growth. In other words, some level of porosity still can be maintained in the coating even after the strain relief annealing step.

4.4.2 Phase Analysis

The X-ray diffraction patterns of the powder, as-received specimen and heat treated specimen are shown in Fig. 4.4. No major difference in the XRD patterns was expected as the coating formation primarily relies on cold plastic deformation of the particles and interfacial fusion. After annealing step, no evidence of new phase formation, for example titanium oxides, was found. Compared to atmospheric plasma sprayed coating, less oxide content are beneficial to the mechanical strength of the coatings.

4.4.3 Microhardness Analysis

Table 4.2 shows the Vickers microhardness values measured on as-sprayed and annealed titanium coatings and the corresponding values on the bulk substrate. For Vickers indentation tests, strong load-hardness dependence has been found in metallic coatings [14]. When a relatively lower load is used, the indentation location, whether in the bulk of a splat or at a splat boundary, affects the final results considerably [14].

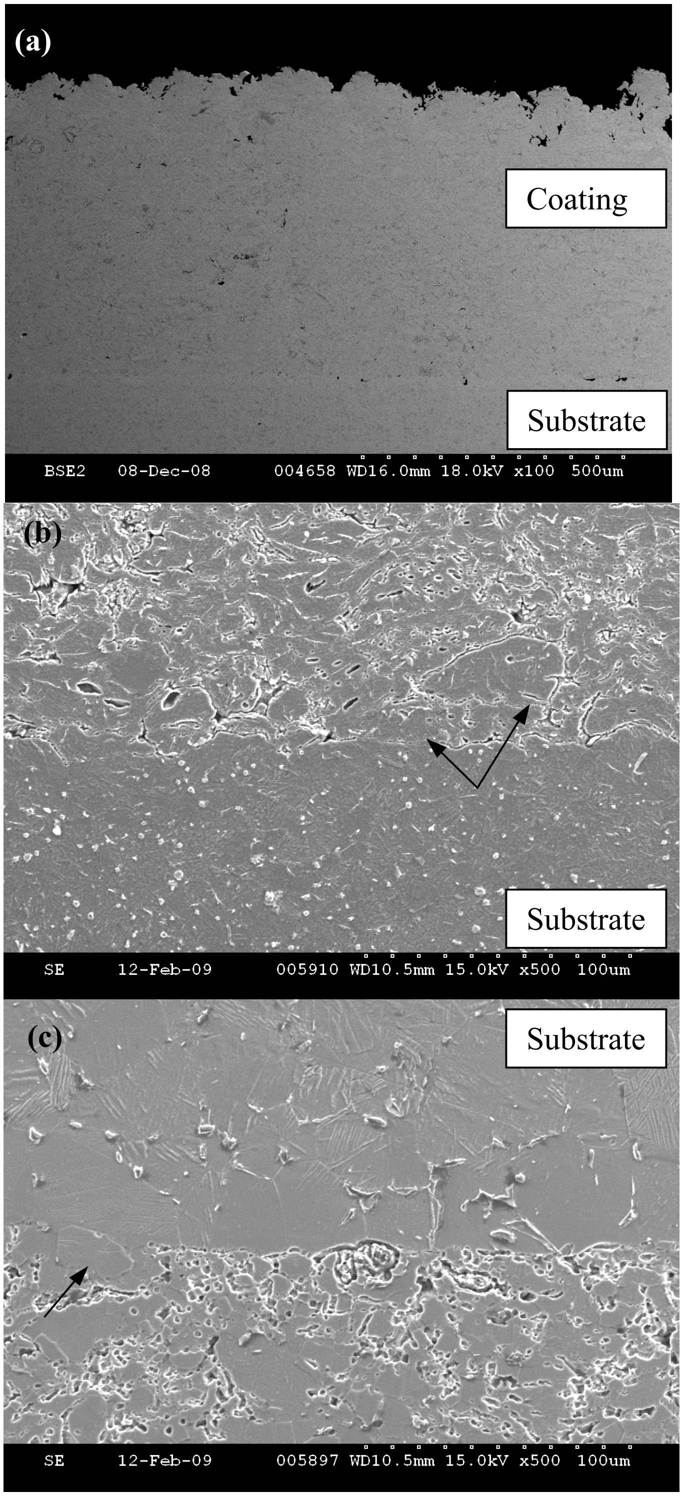

Fig.4.2 Cross-section SEM images showing (a) overall morphology of as-received Ti coating, (b) detailed morphology of etched Ti coating and (c) detailed morphology of annealed and etched Ti coating

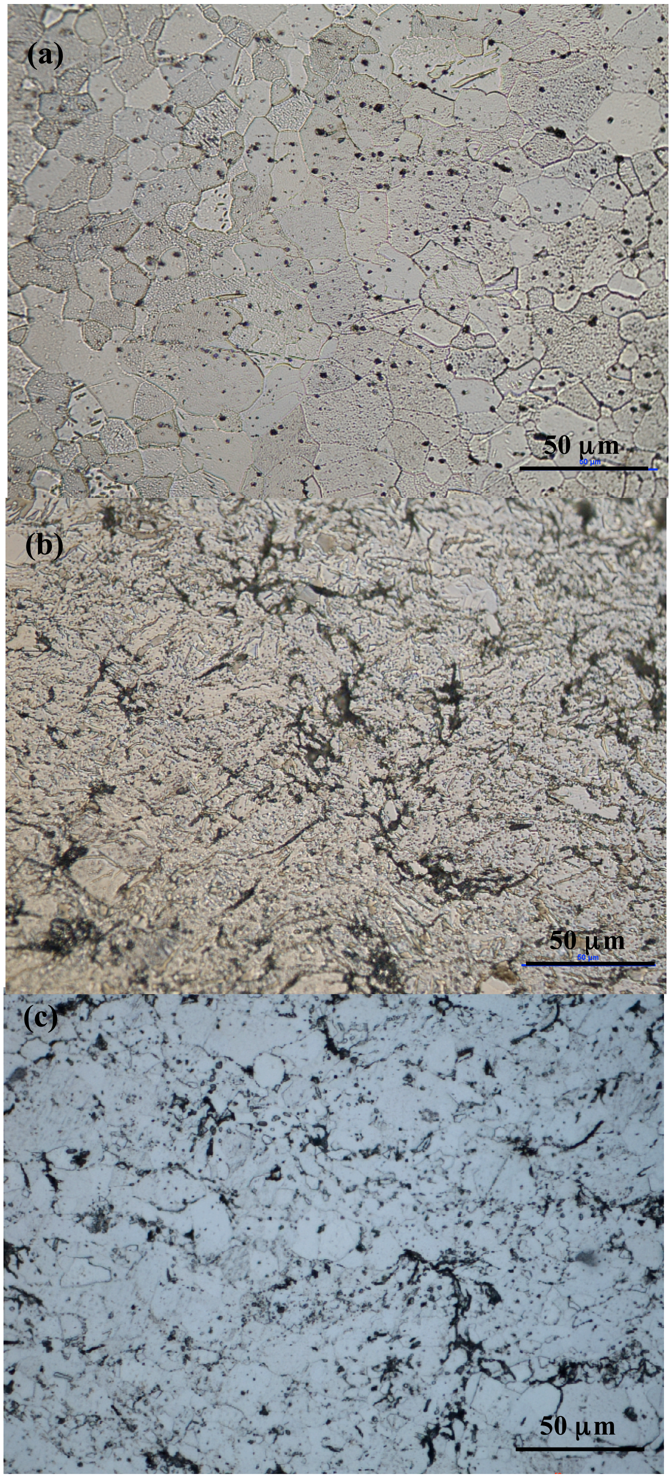

Fig.4.3 Cross-section optical microscope images of (a) etched pure Ti substrate, (b) etched Ti coating and (c) annealed and etched Ti coating at 850 °C for 5 h

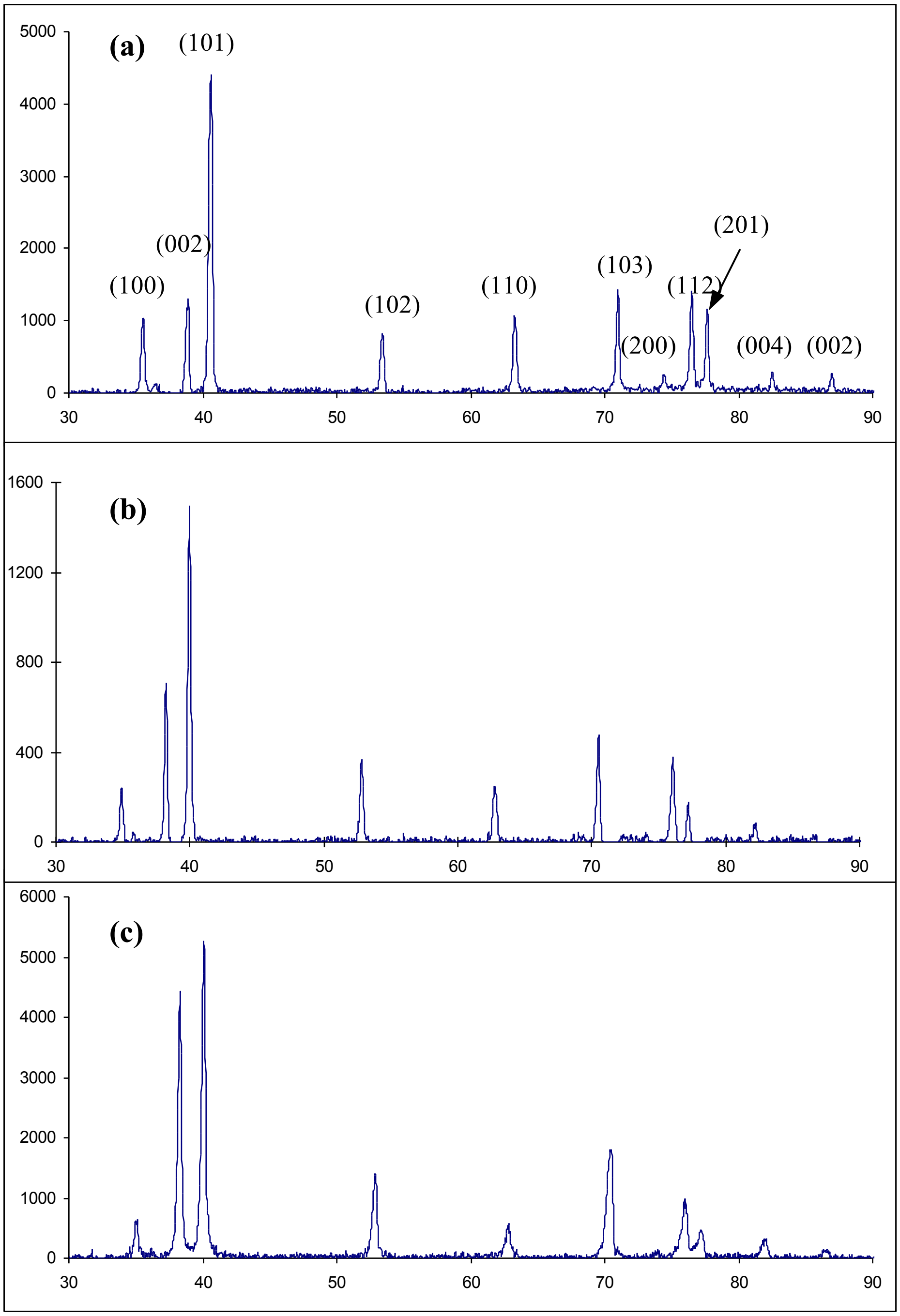

Fig.4.4 X-ray diffraction patterns of (a) Ti powder (b) an as-received Ti coating and (c) annealed Ti coatings

Table 4.2 The Vickers microhardness test results

Specimen	As-received coating (HV)	Annealed coating (HV)
Coating surface	172 ± 22	258 ± 68
Coating middle	207 ± 30	251 ± 89
Coating bottom	221 ± 18	210 ± 30
Substrate surface	288 ± 14	199 ± 39
Substrate bulk	264 ± 14	205 ± 40

This explains why big standard deviation values were found in our coatings. Maximum values correspond to tests that happened in the bulk of a splat and minimum values may correspond to boundary regions. For as-sprayed coatings, the microhardness values increased gradually from coating surface to the bottom. This is possibly due to the fact that the coatings became denser from surface to bottom. After the heat treatment, this trend disappeared, the microhardness of the coatings improved and the highest value (258 HV) on coating surface was found close to the value (264 HV) of bulk substrate. This is because nucleation and recrystallization resulted in homogenous coatings. For pure titanium substrate, the microhardness on the surface (288 HV) is higher than in bulk, which is attributed to cold work hardening effect during the deposition. After annealing, the microhardness value is reduced to ~200 HV, which is due to the release of residual stress. Similar results can be found in literature [12]. Cold-sprayed coatings are reported to have higher hardness than wrought materials [14, 18, 34], however in our case the hardness of the coatings was much lower than that of the wrought material (substrate).

This is because sponge titanium powder was used in this study and inter particulate defects are embedded by the cold deformation. After annealing, the hardness of coatings was improved and the highest value (258 HV) is close to the value (264 HV) for bulk substrate, which in turn indicates a homogenous coating was produced by the heat treatment.

Microstructurally, porosity and residual stress are two major differences between cold sprayed coating and bulk material. These two parameters affect not only corrosion property but also mechanical properties. Although the residual stresses are eliminated by the annealing process, porosity of coatings was not completely eliminated as stated previously.

4.4.4 Potentiodynamic Polarization

Fig.4.5 presents the typical potentiodynamic polarization behavior of pure Ti, annealed Ti, cold sprayed Ti coating and the annealed coating. From the polarization curves, it is evident that all four kinds of samples exhibit highly passive characteristics. The passive current density for as sprayed Ti coating is relatively higher than that of other substrates, but it is still lower than 8×10^{-4} A/cm^2 even at anodic potential of 5 V. The average corrosion potential estimated from these curves are -376 mV, -326 mV and -362 mV for annealed Ti coating, pure Ti substrate and annealed Ti substrate respectively, which are all approximately similar. But, the as received Ti coating has a relatively lower corrosion potential compared to the other three, which is -445 mV. This indicates that the as received Ti coating corrodes easily compared to others. .

From the corrosion potential (- 0.326 V) till 0.2 V, the current density for pure Ti substrate started around 2×10^{-8} A/cm^2 and initially increased rapidly, and then resumed a slower growth at approximately 5×10^{-6} A/cm^2. This characteristic behavior suggests that the protective passive film formed in this potential range [34]. From potential above 1.2 V, the current density further increased at a faster rate to a maximum value of 4×10^{-5} A/cm^2 (obtained at approximately 2.0 V), and then decreased slightly afterward, stabilizing at a current density of about 4×10^{-5} A/cm^2. This behavior suggests that the protective passive film formed previously was gradually replaced by a new protective passive film [35]. The potentiodynamic polarization curve for annealed Ti substrate has similar shape as that for the non-annealed one, but the current density is smaller than that of the non-annealed sample and stabilized at about 1×10^{-5} A/cm^2. This observation i.e., the corrosion property of wrought Ti improved by annealing process illustrates the effect of residual stress relief.

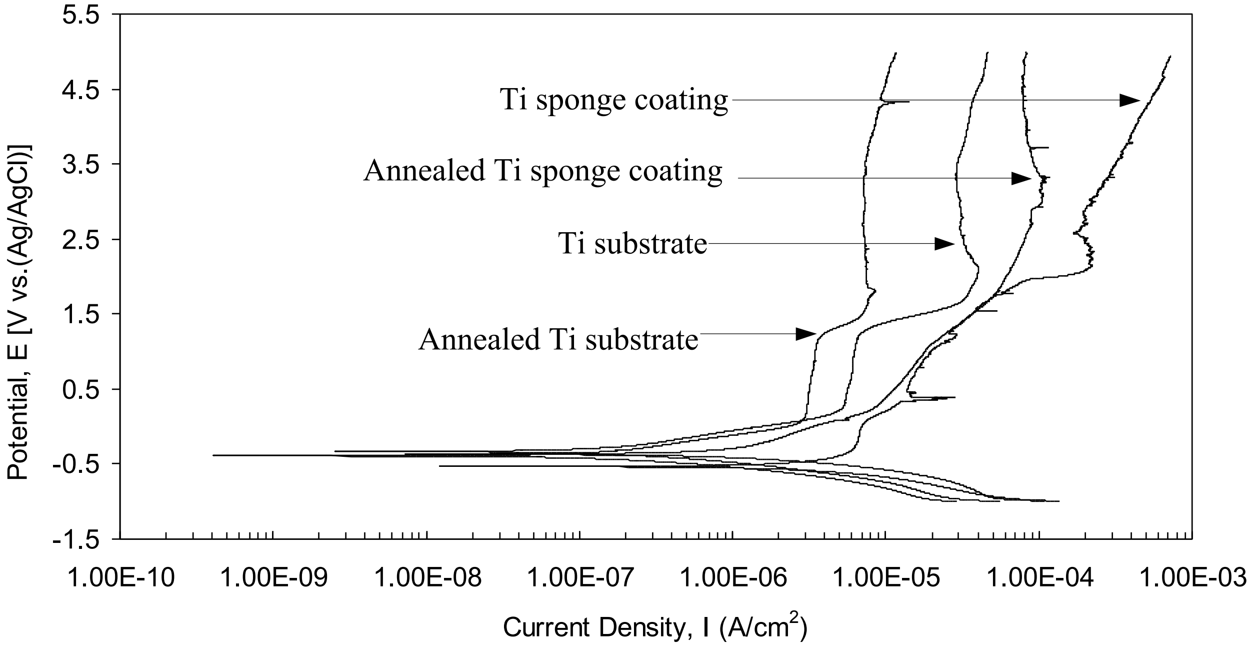

Fig.4.5 Potentiodynamic polarization curves recorded for annealed and non-annealed Ti substrate and cold sprayed Ti coatings in Hank's solution. Scanning rate was 1 mV/s.

The polarization curves for the Ti coatings are considerably different from the substrate samples. In the case of the as received Ti coating, from the corrosion potential (-0.445 V) to about -0.3 V, the current density increased linearly from about 3×10^{-6} A/cm^2 to 6×10^{-6} A/cm^2, and then resumed a slower increase until 0 V. In the anodic regime, the current density increased continuously and reached a maximum value of 7×10^{-4} A/cm^2 at the end of the scanning potential range (5 V). During this process, a current oscillation is seen at a potential around 0.4 V, which typifies a pitting nucleation and re-passivation process. At a potential around 2 V, severe pitting corrosion was observed, which leads to a big fluctuation for current density. It is to be noted that the existing pores on the surface may extend as pits into the sample. For the annealed Ti coating, a current density in the range of 4×10^{-7} A/cm^2 - 1×10^{-6} A/cm^2 was estimated in the potential range of corrosion potential to ~ -0.3 V. The current density increased continuously until around 3.5 V, at which it stabilized at a value of 8×10^{-5} A/cm^2.

Comparing four polarization curves in Fig.4.5, it is apparent that heat treatment process improved the corrosion characteristics of samples. For Ti coating, the overall polarization curve moved leftward after heat treatment and no obvious pitting behavior was observed. And at high potential (above 3.5 V), current density of annealed coating exhibited a stable and passive behavior compared to non-annealed sample. For Ti substrate, heat treatment made the polarization curve move to low current density too. Moreover, the decrease of corrosion current (Table 4.3, from 1.37 $\mu A/cm^2$ to 0.45 $\mu A/cm^2$) and the increase of corrosion potential (from -445 mV to -376 mV) on coating sample do indicate that the heat treatment can significantly improve the corrosion characteristics of cold sprayed Ti coating.

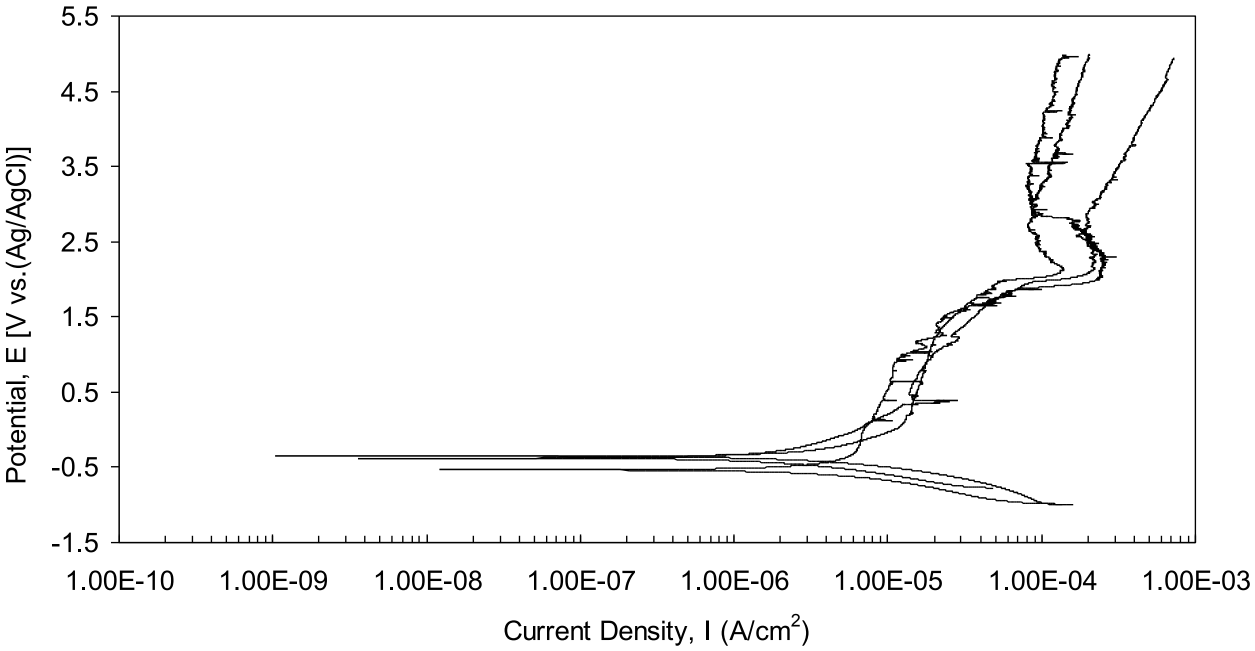

Fig.4.6 Potentiodynamic polarization curves recorded for three cold sprayed Ti coatings in Hank's solution. Scanning rate was 1 mV/s.

The substantial improvements of corrosion characteristics are related to the strain relief as well as defect annihilation that occur during the annealing process. It is to be noted that substantial plastic deformation of the material is an inherent phenomenon in cold spray process. The annealing process causes recovery, recrystallization and grain growth in this cold worked material. The observed reduction in discontinuity and porosity is a direct result of these phenomena. All these factors are expected to contribute towards the reduction in the corrosion rate [20].

To demonstrate the repeatability of results, three measurements are shown for each case. Figs.4.6 and 4.7. present the results for Ti coatings and annealed Ti coatings respectively. The three measurement curves have similar shape and similar value. The pitting corrosion phenomenon occurred around 2.5 V in all three measurements (Fig.4.6) and, it was not observed after annealing (Fig.4.7). The current densities became stable when the potential was increased above 3.5 V for all three measurements compared to non-annealed samples. All these observations indicate a good repeatability of our experiments.

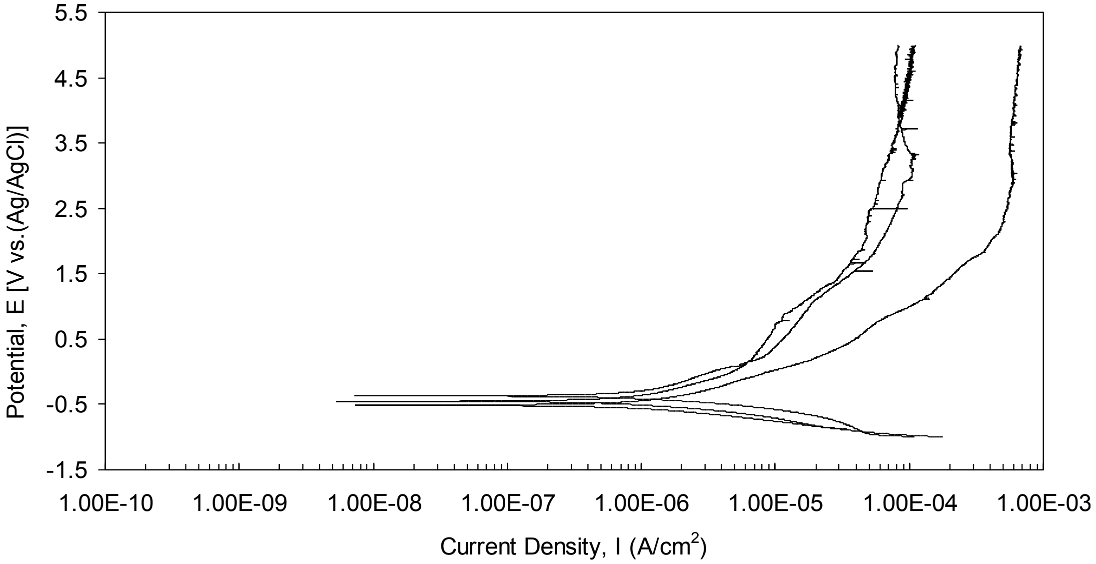

Fig.4.7 Potentiodynamic polarization curves recorded for three annealed cold sprayed Ti coatings in Hank's solution. Scanning rate was 1 mV/s

Table.4.3 Average values of Ecorr, Icorr and Rp obtained from polarization curves using Rp fitting in range -0.1 to 0.1 V vs. OCP

Sample	E_{corr} (mv)	I_{corr} ($\mu A/cm^2$)	Rp ($k\Omega/cm^2$)
As received Ti coating	-445 ± 90	1.37 ± 0.09	19.1 ± 1.2
Annealed Ti coating	-376 ± 70	0.45 ± 0.05	58.9 ± 7.8
Ti substrate	-326 ± 21	0.13 ± 0.03	210.1 ± 46.9
Annealed Ti substrate	-362 ± 16	0.14 ± 0.05	200.2 ± 80.8

The average values of E_{corr}, I_{corr} and R_p, from polarization curves determined by the Z-view software are presented in Table 6. The range of potential used for R_p fitting is from -0.01 V to 0.01 V vs. OCP. Note that the corrosion rates of uncoated samples are lower than those of coated samples and the lower corrosion potential observed in Table 3 for as received Ti coatings also implies that the coated samples are less stable than the other three samples.

After the polarization studies, the Ti coating samples were examined by the SEM. Fig.4.8 (a). shows a typical view of pit morphology and Fig.4.8 (b) shows the magnified view. As observed in Fig.4.8 (a), pits seem to have started from a local defect (void) and propagate along the interface of particles with different rate in different directions. Boven et al., have noted that pits preferentially occur in areas where the tensile residual stresses are high [36]. A newly formed passive layer can be observed under higher magnification, as illustrated in Fig.4.8 (b). Detailed investigations indicated that the passive layer consists of two types of morphologies: the particles with spherical shape (as shown by arrows) embedded in shell shaped films. Phosphates of calcium are usually formed on titanium and its alloys when immersed in Hanks' solution [37]. The existence of phosphorus without calcium in the spherical particles detected by Energy dispersive X-ray spectroscopy (EDS) analysis indicates that the spherical particles might be titanium phosphate precipitated on the surface of Ti oxide film. A detailed examination of formation mechanism and composition of newly formed layer need further attention.

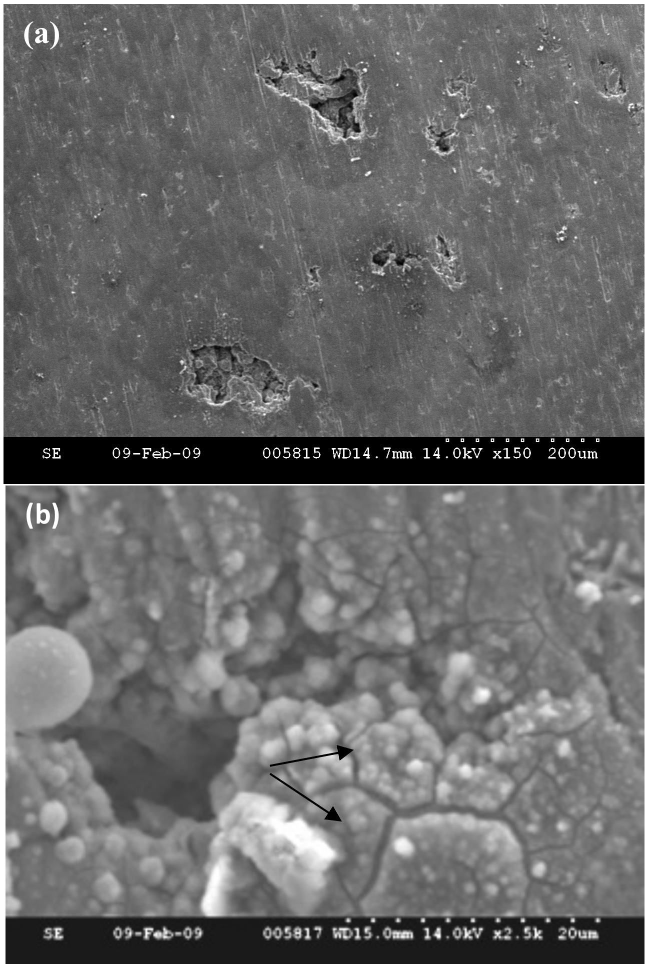

Fig.4.8 SEM images showing characteristic morphologies of pitting generated on as-sprayed coating surface during the polarization process: (a) overall surface view and (b) high magnification view showing newly formed layer.

4.4.5 Electrochemical Impedance Spectroscopy

The representative electrochemical impedance spectra obtained prior to polarization together with the fitted curves are shown in Fig.4.9. After potentiodynamic polarization test and one hour waiting for a stable open circuit potential, the EIS tests were performed again and the results are shown in Fig.4.10. Fig.4.11 shows the equivalent circuits used for simulating the spectra obtained from different samples at various conditions. The quality of fitting to the equivalent circuit was judged by the Chi-

Squared values (χ^2) given in Table 4.4, which confirmed a very good agreement between the fitted and experimental data.

In our earlier study [31], we investigated the influence of electrochemical cell design and solution conductivity on high frequency artifacts. And we demonstrated that the high frequency artifacts are unavoidable in simulated body fluid. However, with K0235 Flat cell combined with Hank's solution, one can ignore the high frequency artifacts when equivalent circuit method is used to analyze impedance spectra data. The values of equivalent circuit elements would not change much by deleting the high frequency artifacts and a meaningful electrolyte resistance is obtained when the high-frequency limit is set around 10K Hz.

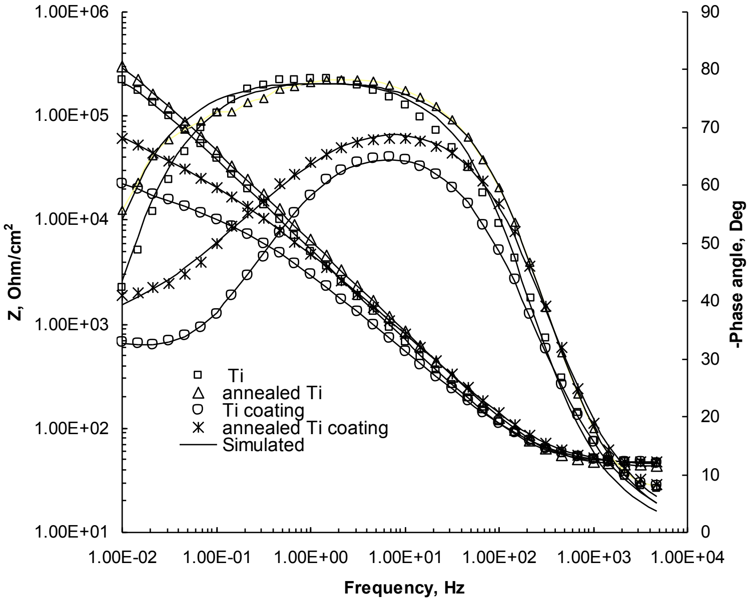

Fig.4.9 Experimental and fitted Bode plots for four kinds of samples of (before polarization test) Ti, annealed Ti, Ti coating and annealed Ti coating in Hank's solution

From Fig.4.9, it is clear that one time constant behavior controlled the corrosion mechanism for Ti substrate samples. The impedance data are simulated by a single layer equivalent circuit (Fig.4.11 (a)) using Zview software, in which R_s refers to solution resistance, constant phase element (CPE1) corresponds to the double-layer capacitance and R_1 is the charge transfer resistance. Here, constant phase element (CPE) was used to substitute the pure capacitance, which accounts for deviations from ideal dielectric behavior related to interface roughness and inhomogeneity [38-40]. A similar result can be found for annealed Ti sample with only a little increase of impedance modulus at lowest frequency range. The equivalent circuit was also used by other literature reports [3, 41, 42] to explain the corrosion mechanism in case of single passive oxide layer present on the metal surface in simulated body fluid solution. The impedance spectra displayed in Fig.4.9 for as received Ti coating as well as annealed Ti coating exhibit a two time constant characteristics. A modified double layer equivalent circuit (Fig.4.11 (b)) can be satisfactorily used for fitting the spectra obtained from Ti coated samples before and after the anneal process. In this case, the first time constant (CPE1) in high frequency range represents the impendence characteristics of outer porous passive layer formed by spontaneous oxidation of Ti. The second time constant (CPE2) in low frequency range represents the impedance characteristics of cold sprayed Ti coating layer. Considering the bottom layer of cold sprayed Ti coating is relatively dense, it is can be anticipated that CPE2 represents the porous top layer of the coating. R1 is the charge transfer resistance of the outer passive oxide layer. The impedance modulus at lowest frequency for coated Ti sample is around 1.1×10^4 Ω cm^2, which is lower than the uncoated sample and the highest phase angle is about -60^o, which is far away from -90^o. This indicates a relatively poor corrosion protection property for the coated samples and this agrees well with the results obtained from potentiodynamic polarization tests. But after heat-treatment, the corrosion property was remarkably enhanced with the increase of the impedance modulus at lowest frequency to 5×10^4 Ω $cm^2$and the highest phase angle increased to -70^o. This indicates cold sprayed Ti coating became denser and more homogenous by annealing process, which is beneficial to the corrosion protection. This observation is in line with the CPE2 value being reduced by one order of magnitude, through the annealing process (Table 4.4). These results from EIS tests are consistent with the outcome from potentiodynamic polarization tests and indicate that the corrosion characteristics of sprayed coating were greatly improved by post heat-treatment process. In addition, the missing of R_2 in the modified equivalent circuit, which is a slightly different form of traditional double-layer equivalent circuit, is probably due to the fact that the porosity of coating under study is small and has high conductivity.

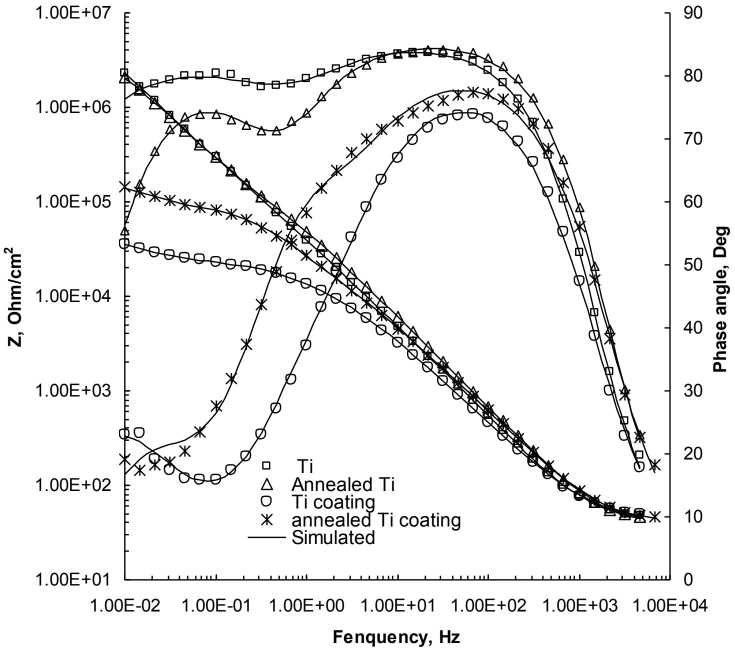

Fig.4.10 Experimental and fitted Bode plots for four kinds of samples, (after the polarization test) Ti, annealed Ti, Ti coating and annealed Ti coating in Hank's solution

After potentiodynamic polarization test, a two-peak EIS curve (Fig.4.10) is observed for Ti substrate samples, which revealed that a two time constant behavior controlled the corrosion mechanism and a new oxide layer was formed by the polarization process. A conventional double layer model equivalent circuit (Fig.4.11 (c)) is satisfactorily used to fit the spectra obtained from Ti substrate samples in polarized state. This circuit is slightly different from the modified circuit (Fig.4.11 (b)), in terms of addition of the resistance R_2 to represent the transfer resistance of the newly formed oxide layer. EIS spectra obtained from Ti coatings and annealed Ti coatings after polarization test are satisfactorily simulated by the equivalent circuit based on a three-layer model (inner sprayed Ti coating, outer oxide layer and the newly formed layer, see Fig.4.11 (d)). Similar three-layer model was also used by Wang et al. [38] to simulate the nucleation and growth of apatite on chemically treated titanium alloy.

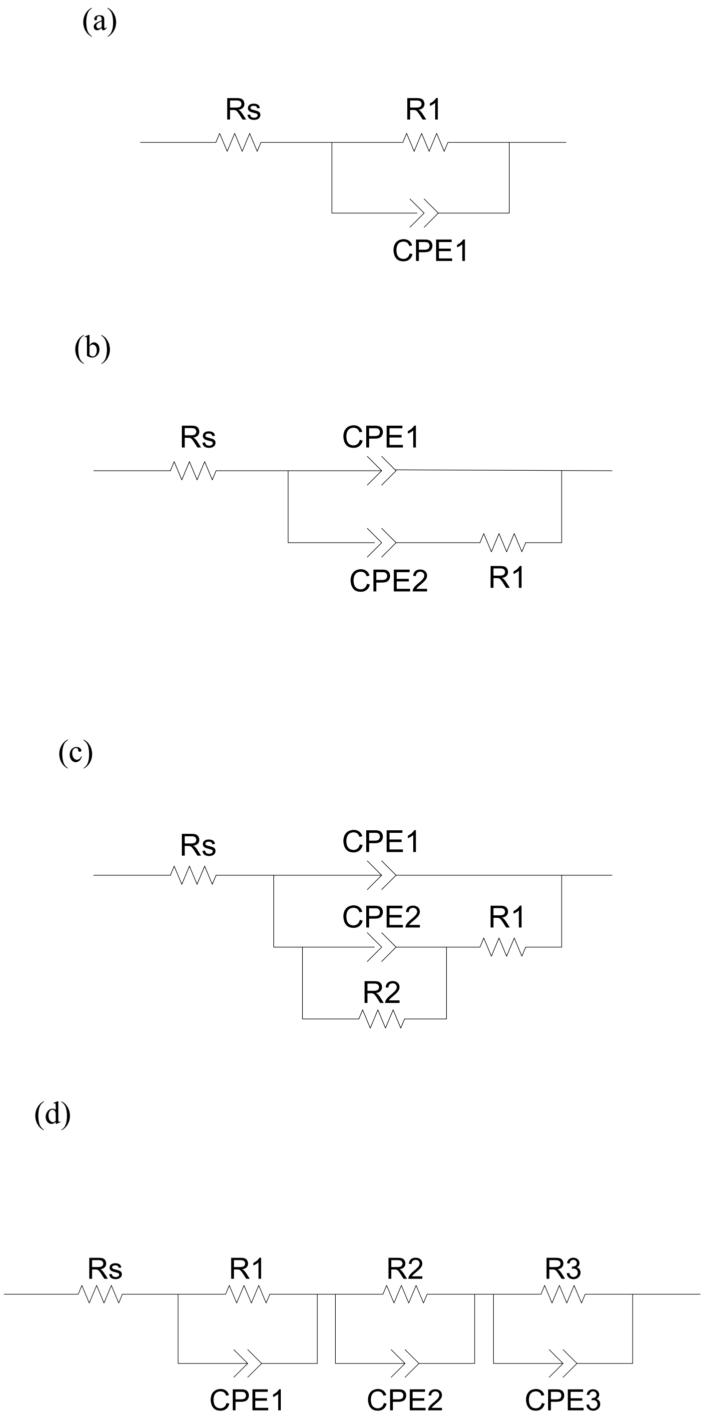

Fig.4.11 Electrochemical equivalent circuits used for the interpretation of the measured impedance spectra

The impedance results in Fig. 4.10 show that after polarization test, a new layer was formed on the surface of substrate as well as coated samples. But close scrutiny of each of the polarized samples under SEM revealed that this newly formed layer could only be observed in the area near the pits on the coated Ti surface. This is probably because, around the pits, the newly formed layer cracked and formed a shell like morphology (see Fig. 4.8(b)). The EDS analysis indicates that the newly formed layer is Ti oxide layer. Also, titanium phosphate precipitated on Ti oxide layer (Fig. 4.8(b)) results in the appearance of third CPE in the EIS model (Fig. 4.11). In order to better understand the electrochemical phenomena taking place at the interface of biomaterial/cold sprayed Ti coating/Hanks' solution, two physical models were constructed and shown in Fig.4.12. Fig. 4.12(a) represents the double-layer model for cold sprayed Ti coating before polarization, which corresponds to the equivalent circuit of Fig. 4.11(b). Fig. 4.12(b) represents the three-layer model for cold sprayed Ti coating after polarization. Different with Fig. 4.12(a), a newly formed TiO_2 layer was presented on the top surface.

After comparing the EIS data of Ti substrate before and after the polarization tests, it can be found that the impedance modulus at lowest frequency increased from 2×10^5 to 2×10^6 Ω cm^2, and the two phase angles at peak points are both close to -90^o. This suggested that the newly formed oxide layer was beneficial to corrosion protection of the coatings. In addition, from Table 4.4, it is obvious that the newly formed oxide layer acts as an ideal capacitor (with n value close to 1), which in turn indicates an improved corrosion property for the material.

Table 4.4 EIS spectra fitting results obtained from experimental impedance data using the electrochemical equivalent circuits of Fig. 12. The abbreviations Pl (polarized), Al (annealed), Ct (coating) were used in the table

Samples	EC	R_1 (Ω cm^2)	CPE1 (F cm^{-2})	n_1	R_2 (Ω cm^2)	CPE2 (F cm^{-2})	n_2	R_3 (Ωcm^2)	CPE3 (F cm^{-2})	n_3	Chi-Squared
Ti	(a)	3.53×10^{5}	3.81×10^{-5}	0.88	-	-	-	-	-	-	2.89×10^{-3}
(Pl) Ti	(c)	2.20×10^{5}	4.10×10^{-6}	0.95	2.53×10^{7}	1.30×10^{-6}	0.82	-	-	-	3.06×10^{-4}
(Al) Ti	(a)	3.74×10^{5}	5.33×10^{-5}	0.84	-	-	-	-	-	-	6.31×10^{-4}
(Al&Pl)Ti	(c)	1.79×10^{5}	3.13×10^{-6}	0.96	4.41×10^{6}	2.45×10^{-6}	0.89	-	-	-	2.94×10^{-4}
Ti Ct	(b)	0.12×10^{5}	7.02×10^{-5}	0.79	-	2.30×10^{-4}	0.48	-	-	-	2.80×10^{-4}
(Pl)Ti Ct	(d)	6732	1.11×10^{-5}	0.90	14754	2.05×10^{-5}	0.90	48581	3.81×10^{-4}	0.77	4.62×10^{-4}
(Al)Ti Ct	(b)	11148	4.06×10^{-5}	0.82	-	4.12×10^{-5}	0.37	-	-	-	4.56×10^{-4}
(Al&Pl)Ti Ct	(d)	3980	1.36×10^{-5}	0.92	77140	7.75×10^{-6}	0.91	88680	1.06×10^{-4}	0.88	1.54×10^{-3}
Ti Ct (2h)	(b)	2476	9.3×10^{-4}	0.67	-	1.37×10^{-3}	0.55	-	-	-	4.87×10^{-4}
Ti Ct (24h)	(b)	1310	1.01×10^{-3}	0.70	-	1.14×10^{-3}	0.59	-	-	-	4.07×10^{-4}
Ti Ct (48h)	(b)	1226	7.7×10^{-4}	0.72	-	1.24×10^{-3}	0.60	-	-	-	6.46×10^{-4}

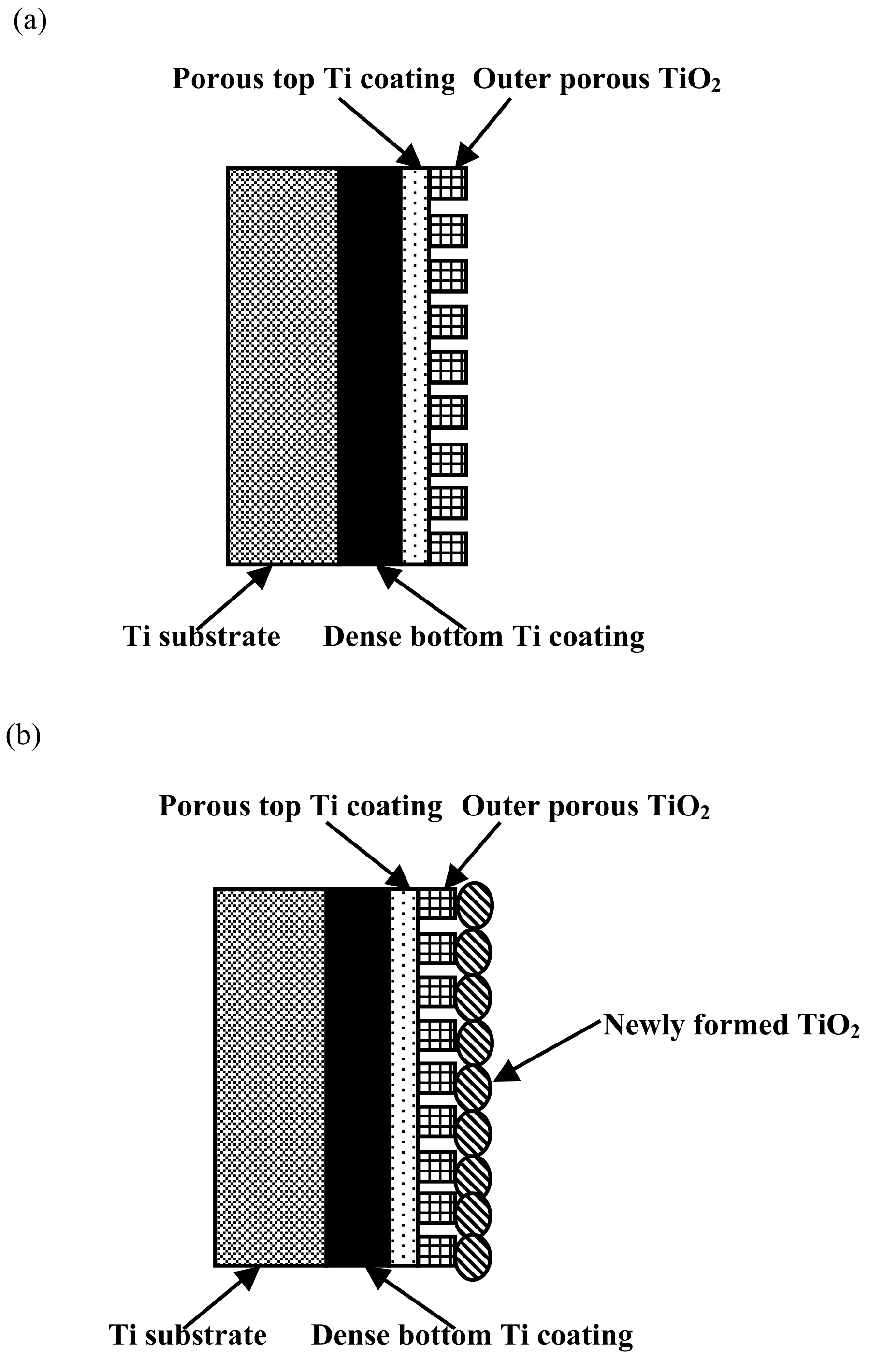

Fig. 4.12 Physical model of biomaterial/Ti coating/Hanks' solution interface:
(a) double-layer model for cold sprayed Ti coating before polarization test
(b) three-layer model for cold sprayed Ti coating after polarization test

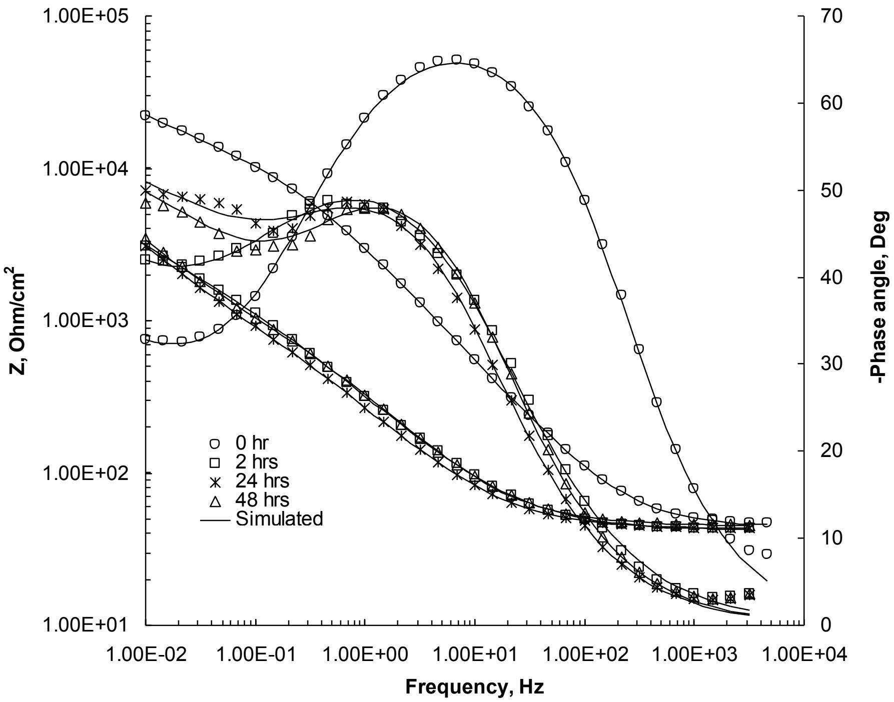

Fig.4.13 Experimental and fitted Bode plots for Ti coatings with immersion time of 0, 2, 24 and 48 hrs in Hank's solution

Further EIS measurements were carried out at 2, 24, 48 hrs for Ti coating immersed in Hank's solution and the results are presented in Fig.4.13. The impedance modulus decreased drastically in the beginning 2 hrs of immersion, the value at lowest frequency dropped from 1.1×10^4 to 1.2×10^3 Ω cm^2. However after 2 hrs there was no significant change in impedance modulus. At low frequency, the phase angle was reduced from -30° to -40° with an immersion time of 2 hrs. When the immersion time was increased to 24 hrs, the phase angle was reduced further to -50°. At middle frequency, the phase angle was shifted to -50° with an increase of immersion time.

The immediate decrease of impedance value and increase of phase angle at middle frequency for 2 hrs of immersion both indicated a decrease in corrosion resistance of outer passive layer formed by spontaneous oxidation of Ti. This was also suggested by the decrease of R1 value with the increase of immersion time (Table.4.4). The unchanged nature of Bode plot for 24 hrs and 48 hrs immersion indicated that a stable and passive oxide film formed.

4.5 Conclusions

Pure titanium coatings composed with porous top layer and dense bottom layer were successfully deposited by cold spray method. Porosity and residual stress are two major characteristics for cold sprayed coatings, which affect their mechanical and corrosion properties. Our results show a good correspondence between these two characteristics and coating properties. The results also showed that post deposition heat treatment, carried out at 850 ^{o}C for 5 h, drastically improved the microhardness and corrosion characteristics for the coatings. The heat treated Ti coatings showed microhardness and corrosion resistance values close to those for Ti substrates. This is because that the material experienced nucleation and re-crystallization during the annealing step. The residual stresses were relieved and the interconnected porosity was reduced because of atomic diffusion [20]. The potentiodynamic polarization tests were carried out until high voltage (5 V) to form a passive Ti oxide layer. The newly formed layer examined by EIS method revealed that it is beneficial to the improvement of corrosion behavior. The EIS results also indicated that a stable and passive film already formed on surface of Ti coating after immersion of 24 h in Hanks' solution and further immersion would not change its corrosion property much. In addition, the second time constant element present in the impedance diagram for coated samples can be used to determine the electrochemical characteristic of porous top layer of the coatings.

References:

[1]Alexia W.E. Hodgson, Yves Mueller, Dominic Forster, Sannakaisa Virtanen, *Electrochim. Acta*, 47 (2002) 1913.

[2] M. Metikos-Hukovic, E. Tkalcecm A. Kwokal, J. Piljac, *Surf. Coat. Technol.*, 165 (2003) 40.

[3] S. Tamilselvi, V. Raman, N. Rajendran, *Electrochim. Acta*, 52 (2006) 839.

[4] V.Barranco, M.L. Escudero, M.C. Garcia-Alonso, *Acta Biomater.* 7 (2011) 2716.

[5] Peter Heinl, Lenka Muller, Carolin Korner, Robert F. Singer, Frank A. Muller, *Acta Biomater.* 4 (2008),1536.

[6] M.A. Khan, R.L. Williams, D.F. Williams, *Biomaterials* 20 (1999) 631.

[7] Daniel Mareci, Romeu Chelariu, Doina-Margareta Gordin, Gina Ungureanu, Thierry Gloriant, *Acta Biomater.* 5 (2009) 3625.

[8] N.T.C. Oliveira, A.C. Guastaldi, *Acta Biomater.* 5 (2009) 399.

[9] M.C. Garcia-Alonso, L. Saldana, C. Alonso, V. Barranco, M.A. Munoz-Morris, M.L. Escudero, *Acta Biomater.* 5 (2009) 1374.

[10] S. Vercaigne, J.G.C. Wolke, I. Naert, J.A. Jansen, *J. Biomed. Mater. Res.* 41 (1998) 41.

[11] Y.Z. Yang, J.M. Tian, J.T. Tian, Z.Q. Chen, X.J. Deng, D.H. Zhang, *J. Biomed. Mater. Res.* 52 (2000) 333.

[12] K. Balani, T. Laha, A. Agarwal, J. Karthikeyan, N. Munroe, *Surf. Coat. Technol.*, 195 (2005) 272.

[13] Chang-Jiu Li, Wen-Ya Li, *Surf. Coat. Technol.* 167 (2003) 278.

[14] T. Novoselova, P.Fox, R. Morgan, W. O'Neill, *Surf. Coat. Technol.* 200 (2006) 2775.

[15] Wen-Ya Li, Chao Zhang, Xueping Guo, Jinling Xu, Chang-Jiu Li, Hanlin Liao, Christian Coddet, Khiam Aik Khor, *Adv. Eng. Mater.* 9 (2007) 418.

[16] A.C. Hall, D.J. Cook, R.A. Neiser, T.J. Roemer, D.A. Hirschfeld, *J. Therm. Spray Technol.* 15(2006) 233.

[17] T.S. Price, P.H. Shipway, and D.G. McCartney, *J. Therm. Spray Technol.* 15 (2006) 507.

[18] W.-Y. Li, C. Zhang, H. Liao, C.Coddet, *J. Coat. Technol. Res.* 6 (2009) 401.

[19] W.-Y. Li, C. Zhang, H.-T. Wang, X.P. Guo, H.L. Liao, C.-J. Li, C. Coddet, *Appl. Surf. Sci.* 253 (2007) 3557.

[20] T.Hussain, D. G. McCartney, P.H. Shipway, and T. Marrocco, *J. Therm. Spray Technol.* 20 (2011) 260.

[21] Hong-Ren Wang, Wen-Ya Li, Li Ma, Jun Wang, Qi Wang, *Surf. Coat. Technol*, 201 (2007) 5203.

[22] A. Choudhuri, P.S. Mohanty, J. Karthikeyan, *ASM International*, 2009, 391-396.

[23] W.-Y. Li, X.P. Guo, C. Verdy, L. Dembinski, H.L. Liao, C.Coddet, *Scr. Mater.* 55 (2006) 327.

[24] P. Sudharshan Phani, D. Srinivasa Rao, S.V. Joshi, G. Sundararajan, *J. Therm. Spray Technol.*, 16 (2007) 425.

[25] Hong-Tao Wang, Chang-Jiu Li, Guan-Jun Yang, Cheng-Xing Li, *Appl. Surf. Sci.* 255 (2008) 2538.

[26] T. Novoselova, S.Celotto, R. Morgan, P.Fox, W.O'Neill, *J. Alloys Compd.* 436 (2007) 69.

[27] Saden H. Zahiri, Darren Fraser, Mahnaz Jahedi, *J. Therm. Spray Technol.* 18 (2008) 16.

[28] R.S. Lima, J. Karthikeyan, C.M. Kay, J. Lindemann, C.C. Berndt, *Thin Solid Film* 416 (2002) 129.

[29] J. Karthikeyan: NASA/CR-2007-214706

[30] R.S. Lima, A. Kucuk, C.C. Berndt, *J. Mater. Sci. Lett.* 21 (2002) 1687.

[31] Xuan Zhou and Pravansu Mohanty, *ECS Transactions* 33 (2010) 59.

[32] Bernard A. Boukamp, *Solid State Ionics* 20 (1986) 31.

[33] T. Marrocco, D.G. McCartney, P.H. Shipway, A.J. Sturgeon, *J. Therm. Spray Technol.* 15 (2006) 263.

[34] T.Valentre, *Surf. Coat. Technol.* 90 (1997) 14.

[35] Sergio Luiz de Assis, Stephan Wolynec, Isolda Costa, *Electrochimi Acta*, 51 (2006) 1815.

[36] G. Van Boven, W. Chen, R. Rogge, *Acta Mater.* 55 (2007) 29.

[37] T. Hanawa, *Mater. Sci. Eng., C* 24 (2004) 745.

[38] C.X. Wang, M. Wang, X. Zhou, *Biomaterials* 24 (2003) 3069.

[39] Ricardo M. Souto, Maria M. Laz, Rui L. Reis, *Biomaterials* 24 (2003) 4213.

[40] Maan Aziz-Kerrzo, Kenneth G. Conroy, Anna M. Fenelon, *Biomaterials* 22 (2001) 1531.

[41] A.K. Shukla, R. Balasubramaniam, S. Bhargava, *J. Alloys Compd.* 389 (2005) 144.

[42] M.C. Garcia-Alonso, L. Saldana, G. Valles, J.L. Gonzalez-Carrasco, J.Gonzalez-Cabrero, M.E. Martinez, E. Gil-Garay, L. Munuera, *Biomaterials* 24 (2003) 19.

Chapter 5

Electrochemical Corrosion Behavior of Cold Sprayed Hydroxyapatite/Titanium Composites in Simulated Body Fluid

5.1 Abstract

A novel approach-cold spraying technique is successfully used to deposit HAP/Ti composite coating on titanium substrate. The aim of this study is to evaluate the in vitro electrochemical corrosion behavior of cold sprayed 20wt% and 50wt% HAP/Ti composite coating for biomedical application. X-ray diffraction (XRD) analysis and scanning electron microscopy were applied to identify the phases and the morphologies of the coatings. Potentiodynamic polarization and EIS techniques were used to analyze the corrosion behavior in Hanks' solution. The Vickers microhardness and shear punch tests were also conducted to investigate the mechanical property. It was found that cold sprayed 20wt% HAP/Ti coating showed relatively higher corrosion current than pure Ti and 50wt% HAP/Ti coating in Hanks' solution, which indicates a low corrosion resistance. However, the post spray heat treatment improved the corrosion and mechanical properties remarkably. The results obtained in the present work demonstrate suitability of cold spraying technique to manufacture HAP/Ti composite coating on titanium substrate as load-bearing implant material for biomedical applications.

5.2 Introduction

Titanium has been widely used for many years as surgical implant materials due to its remarkable corrosion resistance, good biocompatibility and high mechanical strength. A protective passive titanium dioxide (TiO_2) formed on the surface of the Ti is responsible for both its corrosion resistance and biocompatibility [1-3]. However, the unlikeness of formation of a bone-like apatite layer in body environment deteriorates the bonding strength between implant and bony tissues and hinders its long-term application as biomedical materials [4-7]. Therefore, as a good approach to improve the bioactivity of Ti implants, surface modification technique has attracted considerable attention in recent years.

Hydroxyapatite [HAP, $Ca_{10}(PO_4)_6(OH)_2$] has been proved that not only stimulates the bone growth between implant material and bone but also improves the bonding strength of the implants to the bone [8-21]. Thus, various coating techniques, such as magnetron sputtering [10], powder metallurgy [17,18], and plasma spraying [19-21] have been employed to deposit HAP coating on titanium implant to improve its bioactivity. However, the poor mechanical properties and low bonding strength between HAP coating and metallic substrate hinder its application as a loading bearing implant. To overcome above mentioned disadvantages, a mechanically strong second phase, for example titanium [20], has been added to reinforce the HAP coating. However, because most of these coating techniques are carried out at elevated temperature, titanium reacts readily with oxygen to form TiO_2, which will deteriorate the adhesion of the composite coating to its titanium substrate. In addition, the high temperature involvement may result the decomposition of HAP, which will also deteriorate the novel bioactivity of HAP.

Since its first invention in middle 1980s, cold gas dynamic spray (CGDS) technique has been developed quickly in recent years [22]. It differs from traditional thermal spray technique in that there is no need for heating the feedstock to be melted or semi-melted before spraying. The feedstock particles are accelerated by ‘cold’, high pressure gas of helium or nitrogen to supersonic speeds through a converging/diverging nozzle and then deposited on a substrate by plastic impact deformation at temperatures generally well below the melting point of the feedstock powder [23,24]. The use of cold deformation in the production of materials reduces the oxide content in deposits and avoids the undesirable phase transfer and thermally induced stress simultaneously, which makes cold gas dynamic spray a very attractive technique for many applications [25, 26].

In our previous work [27], HAP/Ti composite coating has been successfully manufactured by cold spray technique. The influence of the process parameters, powder type as well as HAP to titanium ratio has been investigated. The objective of the present work is to study the *in-vitro* corrosion behavior of cold sprayed HAP/Ti composite coating in simulated body fluid solution. The conventional potentiodynamic polarization technique as well as electrochemical impedance spectroscopy (EIS) has been used to evaluate the electrochemical corrosion behavior. In addition, the effects of post-spray heat treatment on the microstructure, mechanical and electrochemical properties of cold sprayed coatings were also investigated.

5.3 Experimental

5.3.1 Sample Preparation

The substrate used for this study was commercially available pure wrought titanium sheet (98.9%, from Mcmaster-Carr Co, USA). Rectangular Ti coupons, 50×36×3 mm^3, cut from sheet materials, were grit blasted with Al_2O_3 particles (36 mesh) and ultrasonically cleaned in acetone for 10 min before cold spraying. Sponge titanium powder (~45 μm) was purchased from Titanium Powder Specialists, LLC, Sandy, UT. Commercial high purity HAP powder (CAPTAL 30, Plasma Biotal Limited, UK) was used at 20wt% and 50wt% level and mechanically mixed with titanium powders. An in-house developed cold spray system was utilized to fabricate HAP/Ti composite coatings under optimized spray parameters listed in Table 1. The basic schemes of the cold spray process are described in literature [22, 24, 28, 29]. The pure titanium sponge coatings were also deposited under same conditions for comparison. After spraying, some samples were annealed at 850 ^oC for 5 h in Argon with 5% hydrogen atmosphere.

5.3.2 Phase, Microstructure Characterization

The microstructural characteristics of coatings were examined using a scanning electron microscope (HITACHI S-2600N SEM). The coatings were cut perpendicular to the coating-substrate interface, hot-mounted, and then polished progressively. The final polishing procedure was performed using colloidal silica with a particle size of 0.04 μm. The samples were then washed in running water and ultrasonically cleaned with acetone. The phase composition of coatings was determined by a RIGAKU MINIFLEX XRD system using Cu Kα. The X-ray data were collected in the 2θ range of 30-55° in steps of 0.02°.

5.3.3 Electrochemical Corrosion Studies

The electrochemical measurements were carried out using a flat three-electrode cell (K0235 Flat Cell, Princeton Applied Research), with the samples acting as the working electrode, a silver/silver chloride electrode as the reference electrode and a platinum grid as the counter electrode. The specimen area exposed to the electrolyte solution was 1 cm^2. A commercially available simulated body fluid solution (SBF), Hanks' balanced salt solution with pH = 7.25 ±0.15 [composition, NaCl: 8 g/L, $CaCl_2$: 0.14g/L, KCl: 0.4 g/L, $NaHCO_3$: 0.35 g/L, Na_2HPO_4 (anhydrous) : 0.0477 g/L, KH_2PO_4 : 0.06 g/L, $MaSO_4$: 0.0977 g/L and D-Glucose : 1g/L] was used as the electrolyte solution.

Potentiodynamic polarization curves were determined by using a Solartron SI 1287 potentiostat and electrochemical impedance spectra were recorded with a Solartron 1255B frequency response analyzer. Prior to each measurement, all samples (as-sprayed and annealed coatings) were polished progressively until a mirror finish surface was achieved. In order to avoid the possible oxidation of samples, the electrochemical tests were commenced immediately after immersion of the samples in Hanks' solution. All the experiments were carried out at least three times under ambient temperature.

For potentiodynamic polarization studies, the working electrodes were polarized from -1 V (Vs. reference electrode potential) to +5 V at a scan rate of 1 mV/s. CorrWare software was used to determine the corrosion potential (E_{corr}), corrosion current (I_{corr}) and polarization resistance (Rp). For electrochemical impedance spectroscopy, measurements were conducted at open-circuit potential (OCP), with the amplitude of sinusoidal signal set at 10 mV. The range of measured frequency extended from 0.01 Hz to 10 kHz, with a logarithmic sweep of six points per decade. The recorded impedance spectra were fitted using the complex nonlinear least square (CNLS) method which was developed by Boukamp [30], with the aid of Zview software.

5.3.4 Microhardness, and Shear Punch Test

The hardness measurements were carried out using a Future-Tech, (Tokyo, Japan) Vickers microhardness tester. The measurements were performed with a load of 200 gf applied for a dwell time of 10 s. Eight indentations were made for each hardness test.

In addition to the basic hardness measurement, the strength of as-sprayed as well as annealed coatings was measured using a testing procedure called "Shear Punch Test (SPT)" under quasi static loading conditions. SPT is a small scale specimen testing procedure in which thin disc samples are punched through a die hole while driving the punch at a constant speed. During the process, load on the punch and punch displacement are measured simultaneously. The tests were carried out using a newly built SPT in our laboratory and more details on the SPT procedure can be found in the literature [31,32]. The diameters of the punch and die employed were 1.51 and 1.54 mm, respectively. Testing was conducted on the coatings that were peeled off from the substrate. Prior to the testing, coatings were thinned down to 200 – 450 microns thickness range with metallographic grinding procedures. An Instron 4469 tester was used to conduct the experiments. The load was measured by the load cell whereas the punch displacement was recorded from the Instron crosshead displacement. The punch was driven at a constant speed of 4.12 μm/s throughout the test. The shear stress is calculated using the equation:

$$\tau = \frac{P}{\pi d_{mean} h}$$

where d_{mean} is the mean of the punch and die diameters, P is the applied load and h is the specimen thickness. Five tests were performed for each material and the average value of maximum stresses (ultimate shear stress) is reported.

5.3.5 Immersion Test of Deposited Coatings in Hanks' Solution

The coated specimens were immersed in vials with 50 ml of Hanks' solution. The experiment was performed at 37 ^{o}C and the vials were sealed to remain sterile. After certain periods of time, the specimens were removed from Hanks' solution, washed with distilled water and dried at room temperature. Then, the morphological and elemental analysis of the coatings was studies by SEM/EDX.

5.4. Results and Discussion

5.4.1 Phase and Microstructure Characterization

Fig.5.1 shows the XRD patterns of cold sprayed HAP/Ti composite coatings as well as the precursor powders. The diffraction peaks of both HAP and Ti phases are observed on cold sprayed composite coatings and no other peaks besides these two phases are shown. This indicates that the phases of both HAP and Ti powders were not altered during spraying process, which suggests that a good bioactivity can be expected from unaltered HAP phase and a good bonding strength can be expected from unaltered Ti phase. The broadening of HAP peaks indicates that the refining effect of HAP particles by cold spraying process. This observation comes from the fact that the particles of HAP powder were crushed into small pieces during spraying process [27].

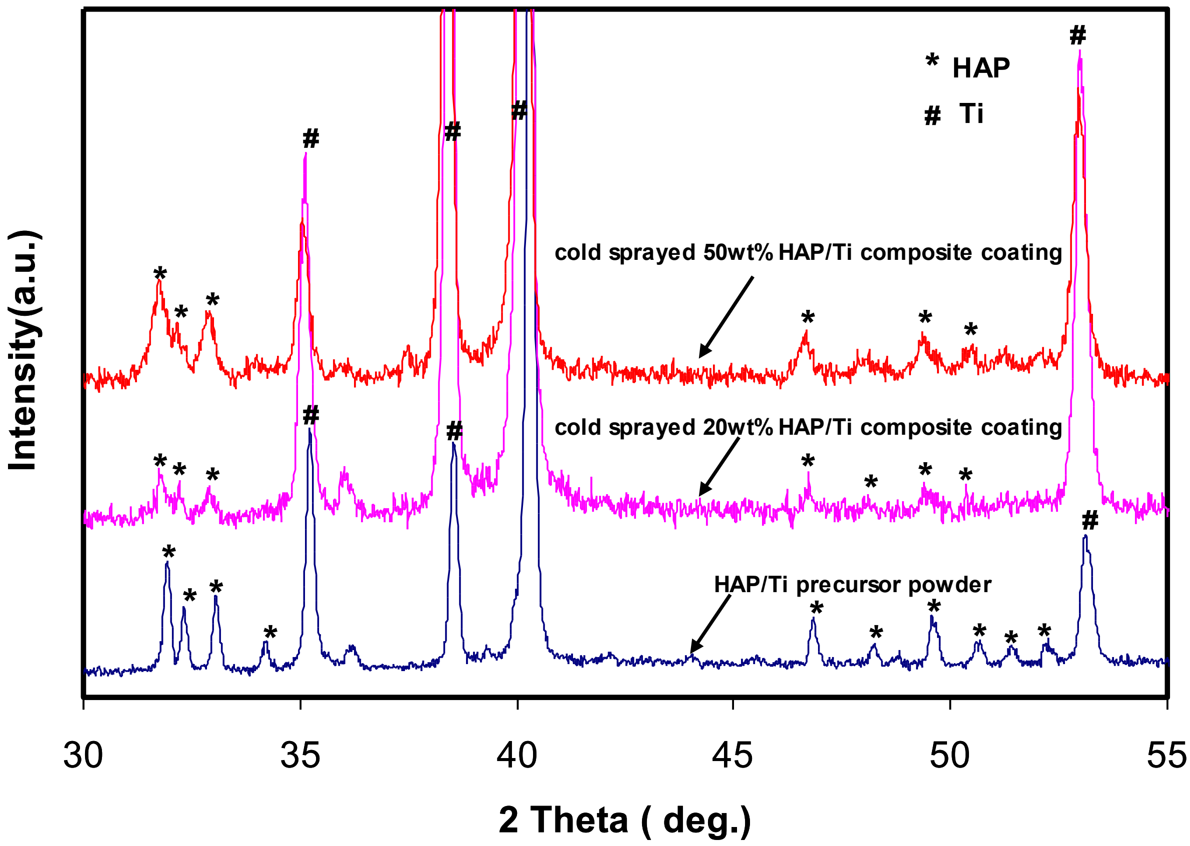

Fig.5.1 X-ray diffraction patterns for cold sprayed 20wt%, 50wt% HAP/Ti composite coating and 20wt% HAP/Ti precursor powder

Fig.5.2a shows the cross-section microstructure of as-sprayed pure titanium coating. It is observed that the top surface layer of the coating is relatively porous compared to the bottom layer. The porous top layer satisfies the high surface area requirement for the implant and the dense bottom layer ensures a good corrosion protection of the substrate and also good bond strength. Fig.5.2b shows the cross-section structure of 20wt% HAP/Ti composite coating. EDX analysis indicates that the darkish

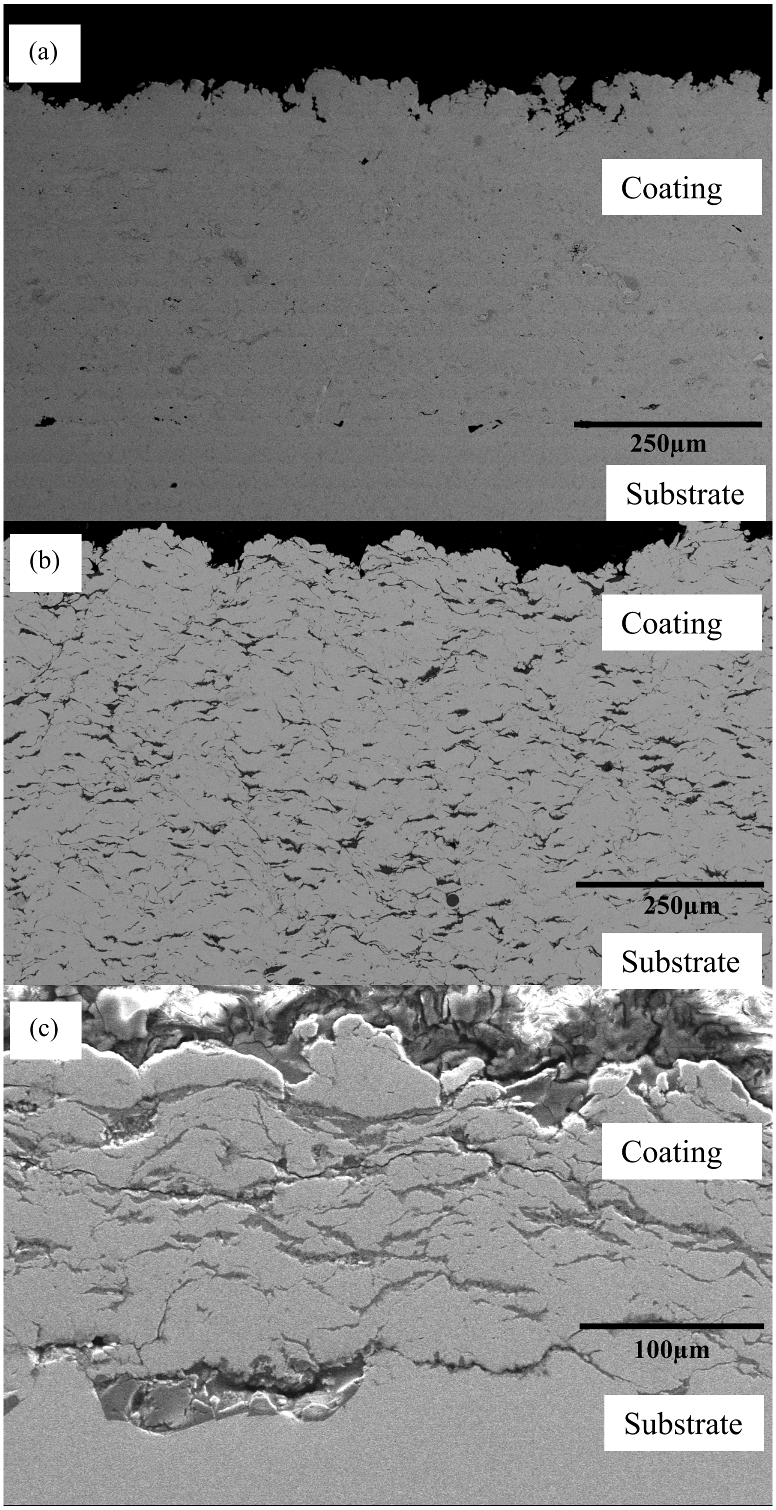

Fig.5.2 Cross section view of cold sprayed coating: (a) pure Ti coating; (b) 20wt% HAP/Ti composite coating; (c) 50wt % HAP/Ti composite coating

gray area is HAP and the light gray area is Ti. It is observed that HAP was successfully deposited in Ti matrix and a dense, homogenous coating was obtained. The microstructure of a coating manufactured with 50wt% HAP powder is shown in Fig.5.2c. Although a significant level of HAP powder is encapsulated in the coating, voids and cracks are observed in these coatings. These voids and cracks inhibit further deposition and limit coating thickness to lesser than 200 μm. Image analysis indicated that more than 15% HAP powder from the powder mixture were lost during the deposition process.

5.4.2 Potentiodynamic Polarization

Fig.5.3 presents the typical potentiodynamic polarization behavior of cold sprayed pure Ti coating, 20wt% and 50wt% HAP/Ti composite coating. From the polarization curves, it is evident that the 50wt% HAP/Ti composite coating has the highest corrosion potential of -0.24 V, the pure Ti coating and 20wt% HAP/Ti coating have the similar corrosion potential with values of -0.445 V and -0.466 V respectively. This result indicates that the 50wt% HAP/Ti coating is thermodynamically most stable in Hanks' solution. All samples show obvious passivation zone in a similar potential range of 0.3 V to 1.2 V, while the 20wt% HAP/Ti coating has the highest passivation current. From potential above 1.2 V, the anodic current density of pure Ti coating increases at a faster rate, indicating TiO_2 passive layer breakdown [33] and at a potential around 2V (pitting potential), a current oscillation is observed, which typifies a pitting nucleation and re-passivation process. A similar phenomenon is observed for 50wt% HAP/Ti coating, but the anodic current density increases more sharply above 1.2 V and severe pitting corrosion is seen. It is noted that the existing pores on the coating surface may extend as pits into the sample. Basically, the cold sprayed coatings are coatings consisted of porous top layer and dense bottom layer. The relatively higher porosity of top surface of cold sprayed coatings promotes the occurrence of pitting corrosion.

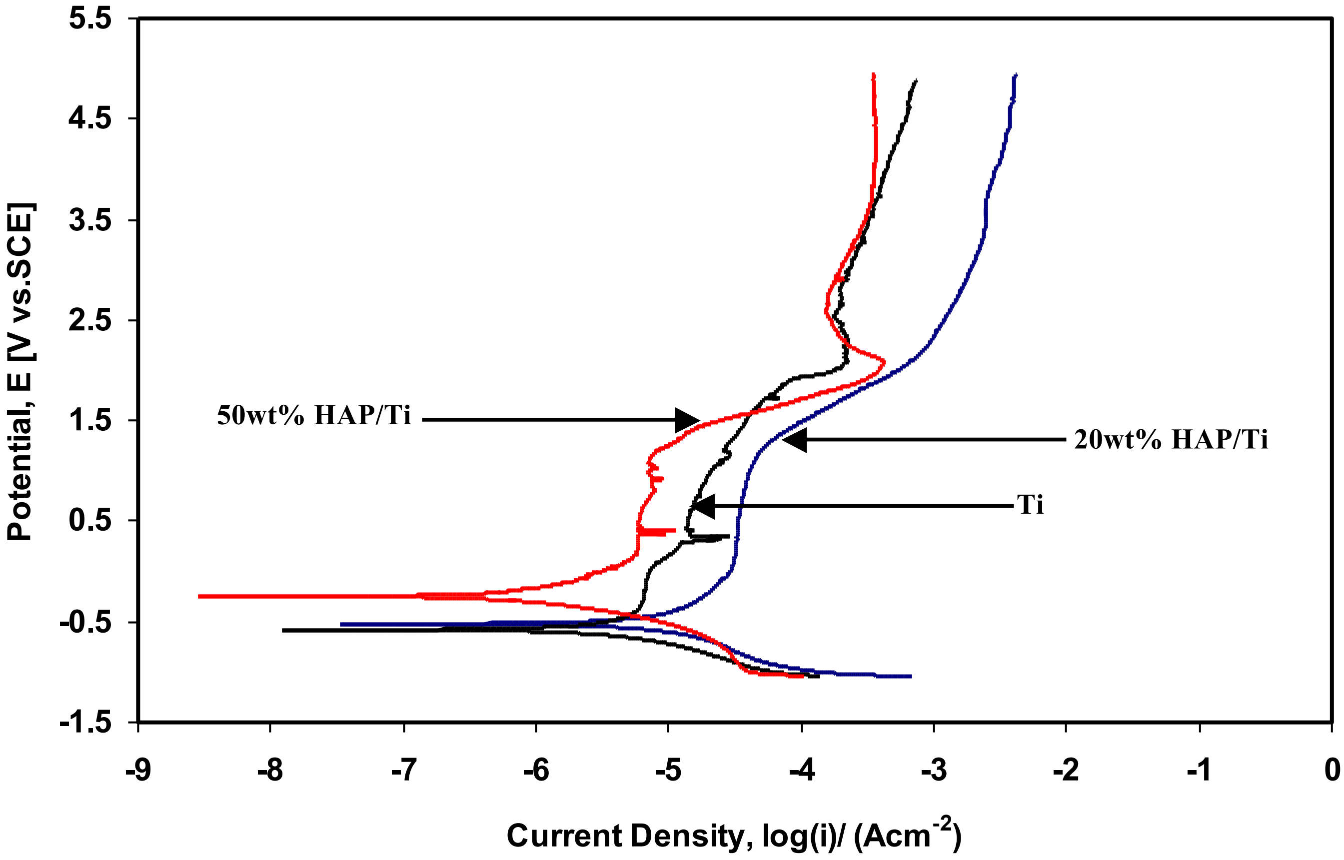

Fig.5.3 Potentiodynamic polarization curves for cold sprayed Ti, 20wt% and 50wt% HAP/Ti composite coatings in Hanks' balanced solution

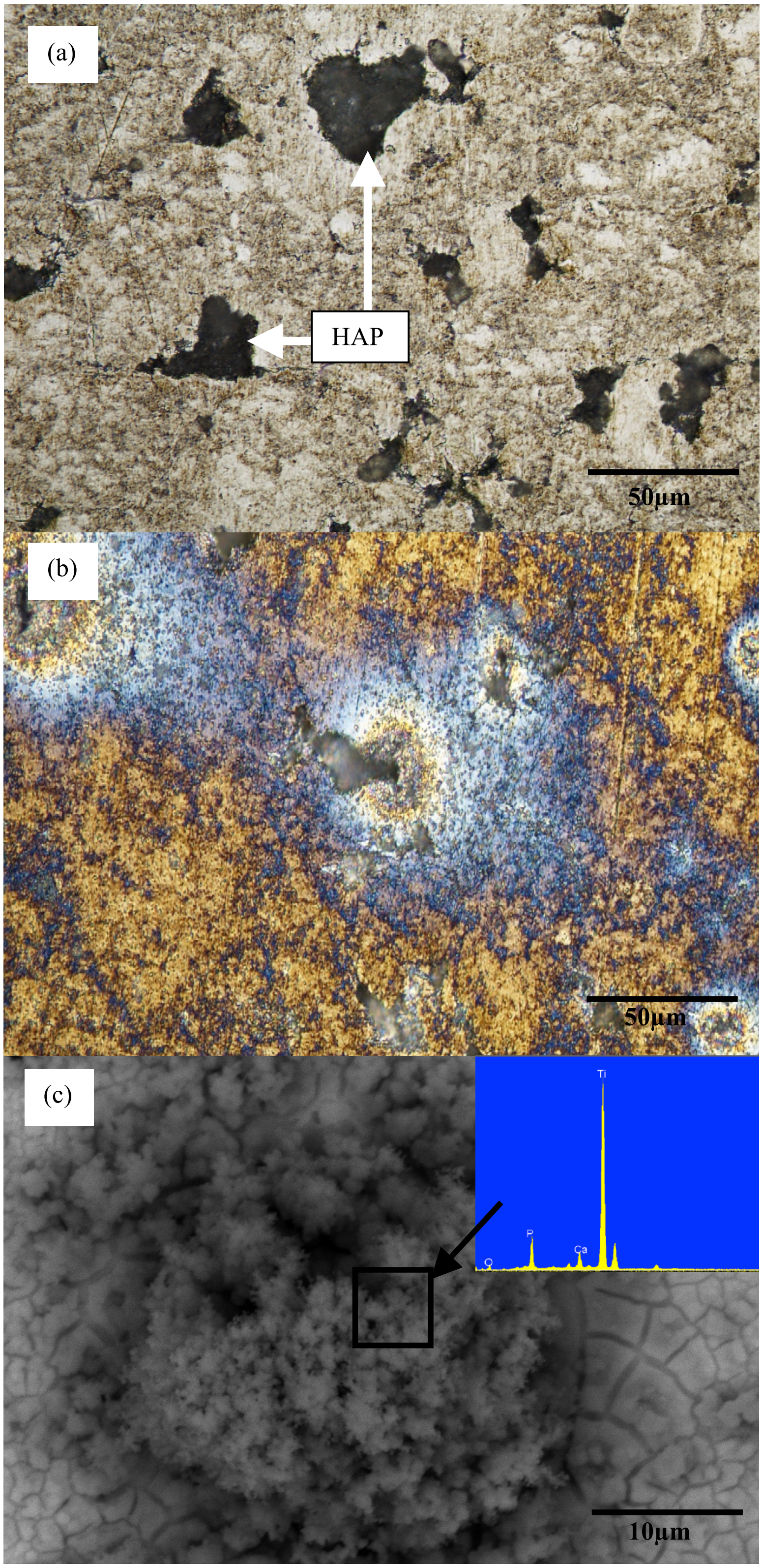

Fig.5.4 Optical microscope images of surface morphology of cold sprayed 20wt% HAP/Ti composite coating: (a) polished surface
(b) corroded surface after potentiodynamic polarization scan
(c) High-magnification SEM image showing one of those corroded areas

Fig.5.4(a) shows the surface morphology of cold sprayed 20wt% HAP/Ti composite coating after progressive polishing. It is observed that HAP was encapsulated within the titanium matrix and HAP particles were nicely compacted. Fig.5.4(b) and (c) are top surface images of cold sprayed 20wt% Hap/Ti composite coating after potentiodynamic polarization scan at low and high magnification. Although no apparent current oscillation is observed for 20wt% HAP/Ti coating, the evidence of the localized corrosion is found in Fig.5.4(b), which is consistent with the results observed by Hussain et al [34] on cold sprayed pure Ti coating. However, compared with Hussain's results, a newly formed layer was observed on top of HAP part of the surface (Fig.5.4c). Energy dispersive x-ray (EDX) spectroscopy analysis indicates that this newly formed layer is apatite layer composed of Ca, P, and O (Fig.5.4c inset picture).

Table 5.1 Average values of Ecorr, Icorr and Rp obtained from polarization curves by Tafel extrapolation method

Material	E_{corr} (mV)	I_{corr} ($\mu A/cm^2$)	Rp ($k\Omega\, cm^2$)
Ti coating	-445 ± 90	1.37 ± 0.1	19.1 ± 1.2
20wt% HAP/Ti	-466 ± 24	3.67 ± 0.8	7.4 ± 1.7
50wt% HAP/Ti	-240 ± 57	0.30 ± 0.1	96 ± 38.4
Annealed 20wt% HAP/Ti	-549 ± 50	0.91 ± 0.1	29.2 ± 4.7

The corrosion current density (I_{corr}) obtained from the polarization curves by the Tafel extrapolation method were summarized in Table 2. The I_{corr} values of the pure Ti coating, 20wt% HAP/Ti coating and 50wt% HAP/Ti coating are 1.37×10^{-6} $\mu A/cm^2$, 3.67×10^{-6} $\mu A/cm^2$ and 3×10^{-7} $\mu A/cm^2$ respectively. 20wt% HAP coating has the highest corrosion current density and it is around 10 times higher than 50wt% HAP coating. The corrosion current density of pure Ti coating is comparable to but a little bit lesser than that of 20wt% HAP coating. This result indicates that 20wt% HAP coating is kinetically most active and the pure Ti coating is comparable to it. At corrosion potential, the corrosion current is in an equilibrium state and can be considered as an exchange current between coating and Hanks' solution indicating deposition and/or release of Ca^{2+} and/or phosphorous [15]. For cold sprayed coating, two parameters are considered as main factors that affect the corrosion behavior: porosity and residual stresses. In our case, besides these two parameters, the content of HAP should also be considered. The mechanism of formation of apatite layer on pure Ti coating and HAP coating is different. The HAP promotes the formation of new apatite layer compared to pure Ti. This explains why 20wt% HAP coating has higher corrosion current than pure Ti coating. The reason why 50wt% HAP coating has lowest corrosion current is quite possible resulted from the fact that our cold sprayed 50wt% HAP coating contains many voids and cracks. These voids and cracks are narrow and long, the recant is consumed faster than it can be supplied by diffusion.

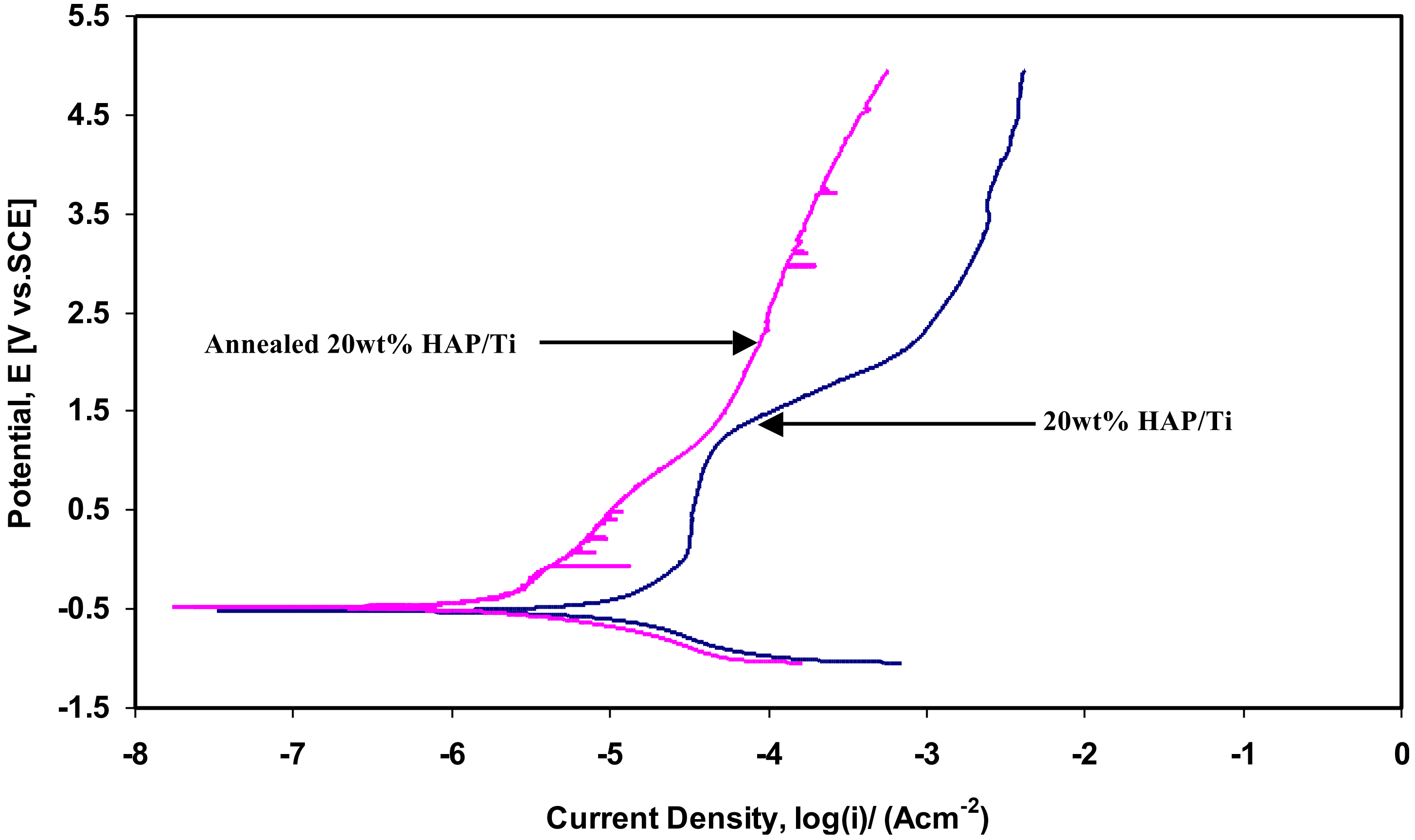

Fig.5.5 Comparison of potentiodynamic polarization curves for cold sprayed 20wt% HAP/Ti composite coating with the one after annealed at 850 oC for 5 hrs

The effects of heat treatment on the corrosion property of 20wt% HAP/Ti composite coating are shown in Fig. 5.5. It can be found that heat treatment process improved the corrosion resistance of samples. For 20wt% HAP/Ti coating, heat treatment made the polarization curve move leftward. Furthermore, the decrease of corrosion current (Table 5.1, from 3.67 μA/cm^2 to 0.91 μA/cm^2) and the increase of corrosion resistance (from 7.4 kΩ/cm^2 to 29.2 kΩ/cm^2) also indicate that the heat treatment can significantly improve the corrosion characteristics of cold sprayed 20wt% HAP/Ti coating. The substantial improvements of corrosion characteristics are related to the strain relief as well as defect annihilation that occur during the annealing process. Fig.5.6 shows the microstructural variation of cold saryed 20wt% Hap/Ti composite coating before and after heat treatment. After annealing, grain boundaries of titanium particles are clearly observed (Fig.5.6b). It is to be noted that substantial plastic deformation of the material is an inherent phenomenon in cold spray process. The annealing process causes recovery,

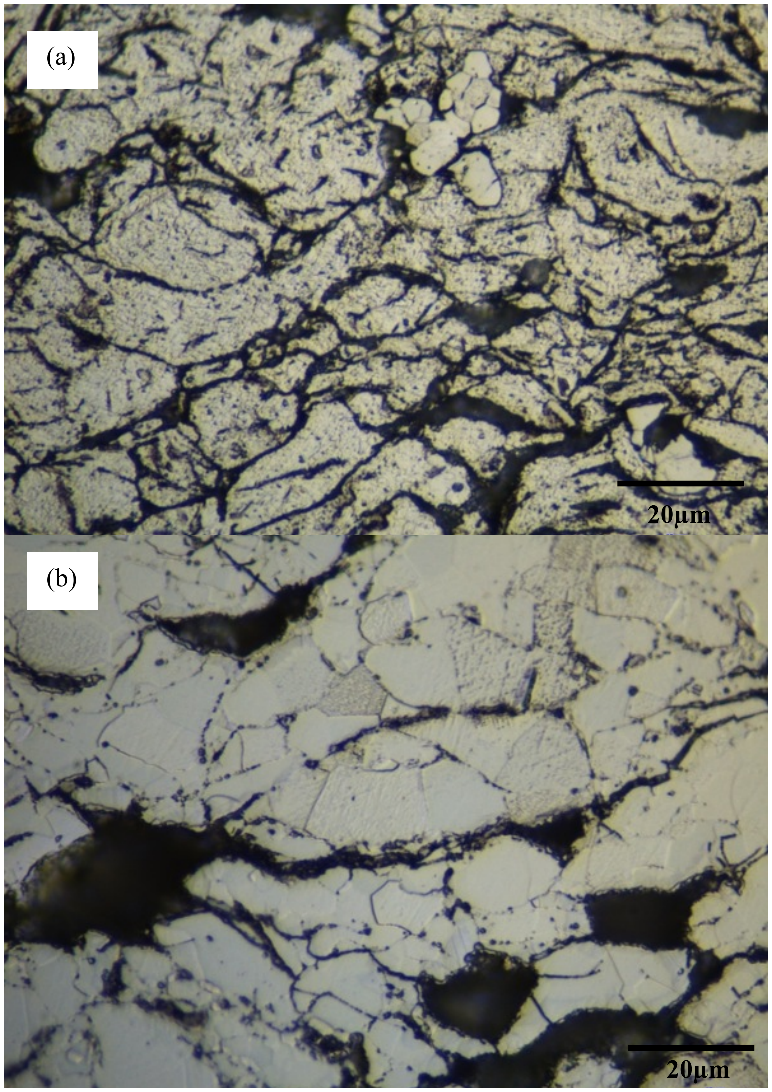

Fig.5.6 Optical microscope images of etched 20wt% HAP/Ti composite coating showing microstructure change before and after heat treatment:
(a) As-sprayed coating (b) Heat-treated coating

recrystallization and grain growth in this cold worked material. The observed reduction in discontinuity and porosity is a direct result of these phenomena. Hussain et al also observed the reduction of interparticle voids in their cold sprayed pure titanium coating [34]. All these factors are expected to contribute towards the improvement of corrosion property. Since HAP would not decompose at a temperature below 1350 ^{o}C [35], our annealing process carried out at a temperature of 850 ^{o}C would not affect the existing crystalline HAP.

5.4.3 Electrochemical Impedance Spectra

Electrochemical impedance experiments were performed at open circuit potential in Hanks' solution. The representative electrochemical impedance spectra of cold sprayed composite coating obtained prior to polarization together with the fitted curves are shown in Fig.5.7. For comparison purpose, EIS analysis on cold sprayed pure Ti coatings is conducted and the typical result is also presented.

The Bode phase angle and impedance plot for as received pure Ti coating, 20wt% as well as 50wt% HAP/Ti composite coating immediately after immersion in Hanks' solution is presented in Fig.5.7. The impedance spectra exhibit two time constants for all three types of coating. The first time constant presented as a phase hump at high frequency range corresponds to the capacitive behavior of the surface coating and describes the dielectric relaxation effects inside the pores of the surface coating as well as the impedance characteristics resulting from the diffusion of electrolyte inside the pores and through the surface coating. The second time constant at low frequency range is related to electrochemical processes taking place at the surface/electrolyte interface.

Considering the bottom layer of cold sprayed coating is relatively dense, electrolyte could not diffuse into it. It is can be anticipated that the second time constant for current study represents electrochemical processes taking place at the interface between electrolyte and dense bottom layer of the coating. Fig.5.8 shows the schematic physical model of substrate/cold sprayed coating/Hanks' solution interface. Such behavior is a typical behavior of a metallic material covered by a porous coating exposed to electrolytic environment [36].

Fig.5.9 shows the equivalent circuit used for simulating the spectra obtained from different samples at the same condition. The quality of fitting to the equivalent circuit was judged by the Chi-Squared values (χ^2) given in Table 5.2, which confirmed a very good agreement between the fitted and experimental data. A modified double layer equivalent circuit has been satisfactorily used to fit the spectra of all three types of coating. In this case, CPE1 in high frequency range represents the capacitive characteristics of cold sprayed pure Ti or composite coating. Considering the bottom layer of cold sprayed coating is relatively dense, it is can be anticipated that CPE1 represents the porous top layer of the coating. CPE2 in low frequency range represents the electrical double-layer capacitance at the electrolyte/dense bottom layer interface. R1 is the electric charge transfer resistance including electron charge transfer process occurring at the electrolyte/dense bottom layer interface and inside the pores of top porous layer.

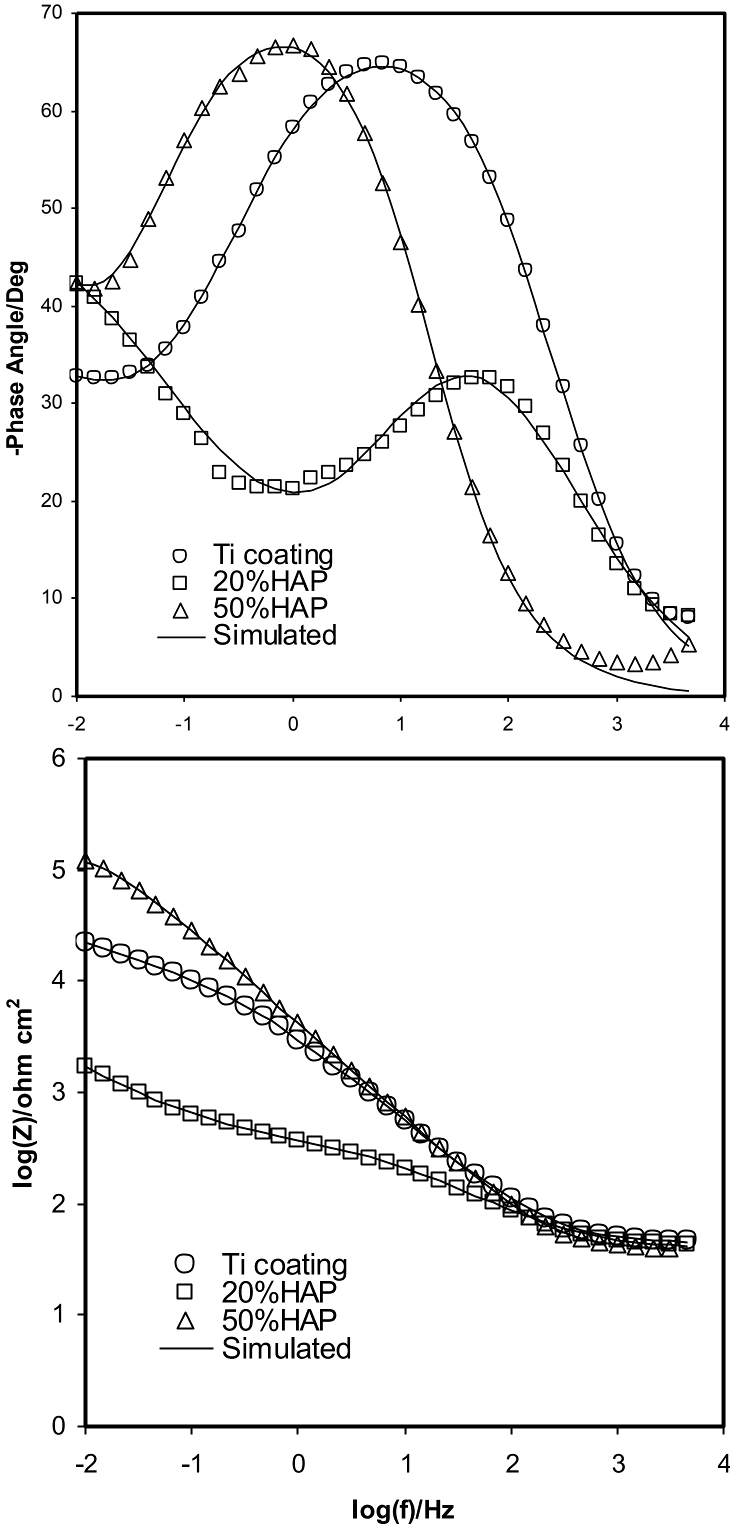

Fig.5.7 Bode phase angle and Bode impedance plot for cold sprayed pure Ti, 20wt% and 50wt% HAP/Ti composite coatings on immediate immersion in Hanks' solution

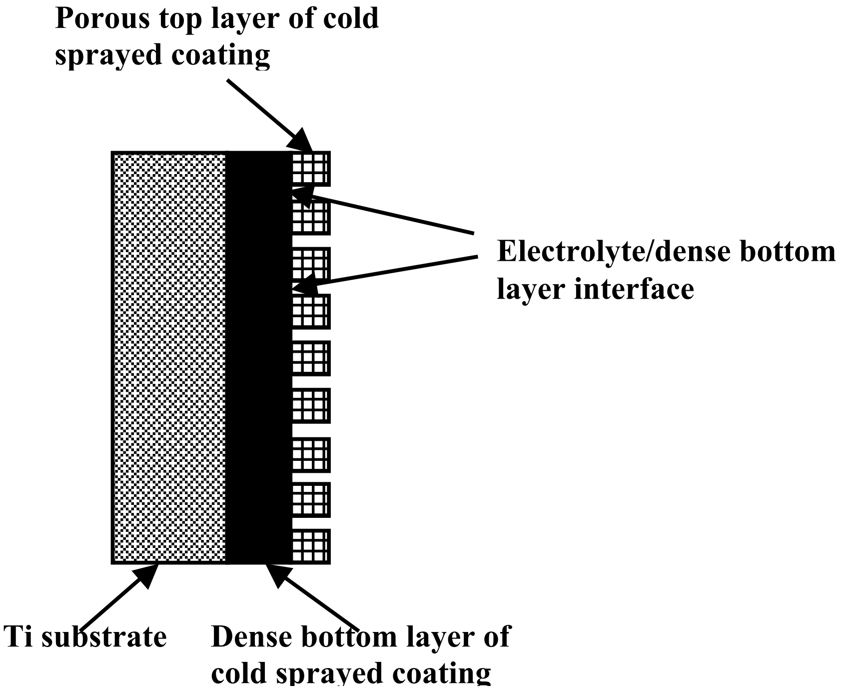

Fig.5.8 Schematic model of substrate/cold sprayed coating/Hanks' solution interface

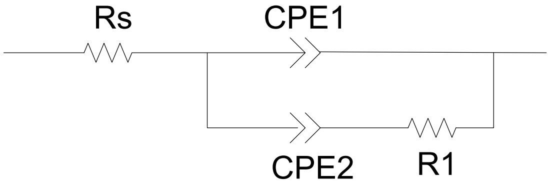

Fig.5.9 Equivalent circuit diagram for cold sprayed pure Ti, 20wt% and 50wt% HAP/Ti composite coatings on immediate immersion in Hanks' solution

The impedance modulus at lowest frequency for 20wt% HAP/Ti composite coating is around $3.2\times10^3\ \Omega\ \text{cm}^2$, which is lower than the other two types of coating and the highest phase angle is around -30^o, which is far away from -90^o. This indicates a relatively poor corrosion protection property meanwhile high kinetic activity for 20wt%

HAP/Ti composite coating and this agrees well with the results obtained from potentiodynamic polarization tests. The spectra obtained for pure Ti coating and 50wt% HAP/Ti coating showed phase angle values close to -70° and the phase hump covered a relatively wide range of frequencies, indicating more capacitive behaviors of these two types of coating than 20wt% HAP/Ti coating.

Table 5.2 EIS spectra fitting results obtained from experimental impedance data using the electrochemical equivalent circuit of Fig. 5.9

Material	$R_1(\Omega cm^2)$	CPE1(Fcm^{-2})	n_1	CPE2(Fcm^{-2})	n_2	Chi-Squared
Ti coat	2621	7.48×10^{-6}	0.89	9.43×10^{-5}	0.16	9.60×10^{-4}
20%HAP/Ti	338.9	2.36×10^{-4}	0.65	3.10×10^{-3}	0.56	0.92×10^{-3}
50%HAP/Ti	6468	5.39×10^{-4}	0.83	1.38×10^{-3}	0.69	1.50×10^{-3}

The impedance parameter values of all three types of cold sprayed coating obtained after fitting the spectra to the equivalent circuit is presented in Table 5.2. It is observed that 50wt% HAP/Ti coating exhibits highest corrosion resistance with highest charge transfer resistance (R1) value compared to the other two types of coating. This result from EIS test is also consistent with the outcome from potentiodynamic polarization test and indicates possible contact of electrolyte with titanium substrate. Similar modified two-layer model was also used by Metikos [14] and Yao [37,38] to study corrosion behavior of sol-gel derived and micro-plasma oxidized ceramic coatings.

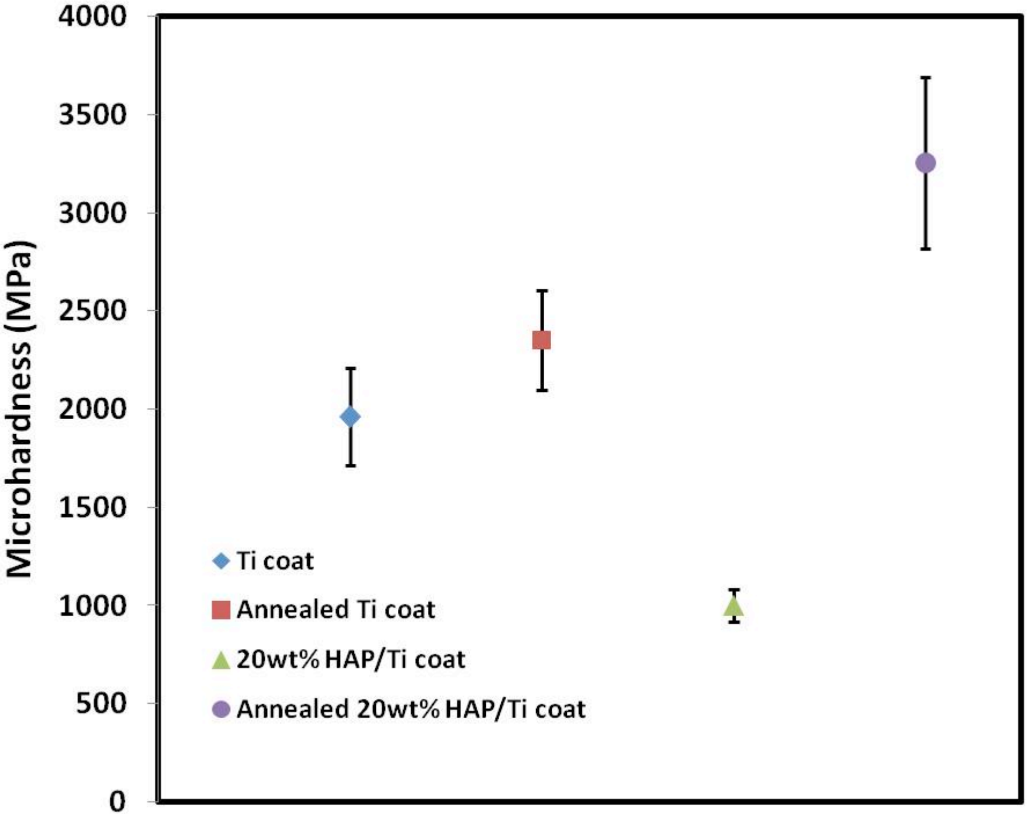

Fig.5.10 Microhardness of cold sprayed pure Ti and 20wt% HAP/Ti composite coatings for both before and after heat-treatment

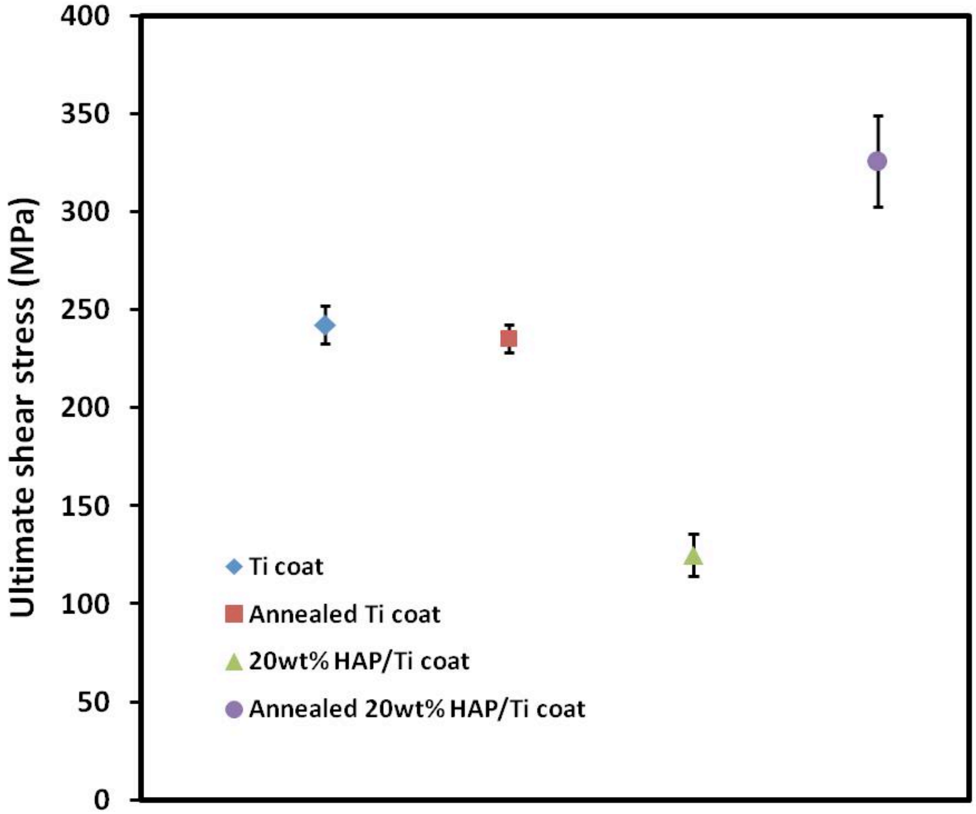

Fig.5.11 Ultimate shear stresses of cold sprayed pure Ti and 20wt% HAP/Ti composite coatings for both before and after heat-treatment

5.4.4 Mechanical Property Characterization

The Vickers microhardness test and shear punch test results for cold sprayed pure Ti and 20wt% HAP/Ti composite coatings for both before and after heat-treatment are summarized in Fig.5.10 and Fig.5.11 respectively. For Vickers indentation tests, strong load-hardness dependence has been found in metallic coatings [24]. When a relatively lower load is used, the indentation location, whether in the bulk of a splat or at a splat boundary, affects the final results considerably [24]. This explains why high standard deviation values were found in our coatings. For shear punch test, a flat solid punch shears thoroughly through the entire thickness of the coating. The overall mechanical property of the coating is measured, which avoids the effect of splat boundary and results a relatively lower standard deviation value. It is observed that for pure Ti coating, ultimate shear stress remained nearly unchanged after heat-treatment and Vickers hardness value just increased a little bit. It is noted that titanium particles experienced nucleation, crystallization and grain growth during annealing process, which resulted reduction of porosity as well as release of residual stresses. The reduction of coating porosity increases the ultimate shear stress and hardness value. However, the release of residual stresses reduces them. For pure Ti coating, the nearly unchanged ultimate shear stress and little changed hardness value resulted from the combined effects of them. For 20wt% HAP/Ti composite coating, both ultimate shear stress and hardness values increased nearly three times after annealing process, which indicates that the porosity is the main factor that affects the mechanical property of cold sprayed composite coating. Besides the reduction of coating porosity, the agglomeration of HAP embedded in Ti matrix (Fig.5.6b) may also contribute to this increase.

5.5 Conclusions

In this study, 20wt% and 50wt% HAP/Ti composite coatings have been successfully deposited by cold spray technique, without compromising the phase constituents of HAP. Compared to pure Ti and 50wt% HAP/Ti coating, 20wt% HAP/Ti coating exhibits higher corrosion current and lower corrosion resistance. However, the post spray heat treatment improve the corrosion property of 20wt% HAP/Ti composite coating remarkably. In addition, the mechanical properties of cold sprayed 20wt% HAP/Ti composite coating such as microhardness and ultimate shear stress were also improved up to three times by post spray heat treatment process. The improvements in both corrosion resistance and mechanical properties are related to coating surface modification during heat treatment process, which resulted defects annihilation, porosity reduction as well as residual stresses relief. The present results indicate that cold spray technique combined with post spray heat treatment provides an effective approach to manufacture HAP/Ti composite coatings with good corrosion and mechanical properties for biomedical applications.

References:

[1] Alexia W.E. Hodgson, Yves Mueller, Dominic Forster, Sannakaisa Virtanen, *Electrochim. Acta* 47 (2002) 1913.

[2] Wojciech Simka, Andrzej Sadkowski, Magdalena Warczak, Aleksander Iwaniak, Grzegorz Dercz, Joanna Michalska, Artur Maciej, *Electrochim. Acta* 56 (2011) 8962.

[3] S. Tamilselvi, V. Raman, N. Rajendran, *Electrochim. Acta* 52 (2006) 839.

[4] M. Karthega, S. Nagarajan, N. Rajendran, *Electrochim. Acta* 55 (2010) 2201.

[5] Shigeru Nishiguchi, Takashi Nakamura, Masahiko Kobayashi, Hyun-Min Kim, Fumiaki Miyaji, Tadashi Kokubo, *Biomaterials* 20 (1999) 491.

[6] Wei-Qi Yan, Takashi Nakamura, Keiichi Kawanabe, Shigeru Nishigochi, Masanori Oka, Tadashi Kokubo, *Biomaterials* 18 (1997) 1185.

[7] C.X. Wang, M. Wang, X. Zhou, *Biomaterials* 24 (2003) 3069.

[8] Gurbhinder Singh, Surendra Singh, Satya Prakash, *Surf. Coat. Technol.* 205 (2011) 4814.

[9] M.F. Morks, Akira Kobayashi, *Surf. Coat. Technol.* 201 (2006) 2560.

[10] Shinn-Jyh Ding, *Biomaterials* 24 (2003) 4233.

[11] R.S. Lima, K.A. Khor, H. Li, P. Cheang, B.R. Marple, *Mater. Sci. Eng. A* 396 (2005) 181.

[12] Won-Gi Kim, Han-Cheol Choe, *Thin solid films* 519 (2011) 7045.

[13] Deliang Qiu, Lejiao Yang, Yansheng Yin, Aiping Wang, *Surf. Coat. Technol.* 205 (2011) 3280.

[14] M. Metikos-Hukovic, E. Tkalcec, A. Kwokal, J. Piljac, *Surf. Coat. Technol.* 165 (2003) 40.

[15] Jianhui Xie, Ben Li Luan, *J. Mater. Res.* 23 (2008) 768.

[16] C.C. Chen, T.H. Huang, C.T. Kao, S.J. Ding, *Electrochim. Acta* 50 (2004) 1023.

[17] C.Q. Ning, Y. Zhou, *Biomaterials* 23 (2002) 2909.

[18] Congqin Ning, Yu Zhou, *Acta Biomaterialia* 4 (2008) 1944.

[19] Ricardo M. Souto, M. Mercedes Lemus, Rui L. Reis, *J. Biomed. Mater. Res. Part A* 70A (2004) 59.

[20] Chun-Cheng Chen, Tsui-Hsien Huang, Chia-Tze Kao, Shinn-Jyh Ding, *J. Biomed. Mater. Res. Part B* 78B (2006) 146.

[21] Shinn-Jyh Ding, Tsui-Hsien Huang, Chia-tze Kao, *Surf. Coat. Technol.* 165 (2003) 248.

[22] K. Balani, T. Laha, A. Agarwal, J.Karthikeyan, N. Munroe, *Surf. Coat. Technol.* 195 (2005) 272.

[23] Chang-Jiu Li, Wen-Ya Li, *Surf. Coat. Technol.* 167 (2003) 278.

[24] T. Novoselova, P. Fox, R. Morgan, W. O'Neill, *Surf. Coat. Technol.* 200 (2006) 2775.

[25] Wen-Ya Li, Chao Zhang, Xueping Guo, Jinling Xu, Chang-Jiu Li, Hanlin Liao, Christian Coddet, Khiam Aik Khor, *Adv. Eng. Mater.* 9 (2007) 418.

[26] A.C. Hall, D.J. Cook, R.A. Neiser, T.J. Roemer, D.A. Hirschfeld, *J. Therm. Spray Technol.* 15 (2006) 233.

[27] A. Choudhuri, P.S. Mohanty, J. Karthikeyan, *ASM International* (2009) 391.

[28] R.S. Lima, A. Kucuk, C.C. Berndt, J. Karthikeyan, C.M. kay, J. Lindemann, *J. Mater. Sci. Lett.* 21 (2002) 1687.

[29] Frank Gartner, Thorsten Stoltenhoff, Tobias Schmidt, Heinrich Kreye, *J. Therm. Spray Technol.* 15 (2006) 223.

[30] Bernard A. Boukamp, *Solid State Ionics* 20 (1986) 31.

[31] R.K. Guduru, K.A. Darling, R. Kishore, R.O. Scattergood, C.C. Koch, K.L. Murty, *Mater. Sci. Eng. A* 395 (2005) 307.

[32] R.K. Guduru, K.A. Darling, R.O. Scattergood, C.C. Koch, K.L. Murty, M. Bakkal, A.J. Shih, *Intermetallics* 14 (2006) 1411.

[33] Robert Wen-Wei Hsu, Chun-Chen Yang, Ching-An Huang, Yi-Sui Chen, *Mater. Sci. Eng. A* 380 (2004) 100.

[34] T. Hussain, D.G. McCartney, P.H. Shipway, T. Marrocco, *J. Therm. Spray Technol.* 20 (2011) 260.

[35] G. Muralithran, S. Ramesh, *Ceram. Int.* 26 (2000) 221.

[36] Ricardo M. Souto, Maria M. Laz, Rui L. Reis, *Biomaterials* 24 (2003) 4213.

[37] Zhongping Yao, Zhaohua Jiang, Shigang Xin, Xuetong Sun, Xiaohong Wu, *Electrochim. Acta* 50 (2005) 3273.

[38] Zhongping Yao, Zhaohua Jiang, Fuping Wang, *Electrochem. Acta* 52 (2007) 4539.

Chapter 6

In vitro study of cold sprayed hydroxyapatite/titanium composite coatings

6.1 Abstract

In this chapter, dense and homogenous 20wt% HAP/Ti composite coatings were successfully deposited on Ti substrates by cold gas dynamic spray technique. X-ray diffraction (XRD) analysis and scanning electron microscopy were applied to identify the phases and the morphologies of the coatings. The bonding strength, corrosion behavior and in vitro immersion properties of composite coatings were also investigated. The results revealed that the phase composition of the HAP in the deposit is identical to that of the precursor powder and the bonding strength of the deposit is comparable/better to that of the plasma sprayed HAP. A relatively higher corrosion current of HAP/Ti composite than that of pure Ti coating in simulated body fluid indicates a good bioactivity for composite coating, which is also testified by the formation of apatite layer on surface of composite coating in vitro test. The cold sprayed HAP/Ti composite can be anticipated to be a promising load-bearing implant material for biomedical applications.

6.2 Introduction

Hydroxyapatite [HAP, $Ca_{10}(PO_4)_6(OH)_2$] has been widely used as dental and orthopedic implant materials because it chemically connects the implant with the bone due to its chemical and crystallographic similarity with bone minerals [1-3]. It has been proved that the existence of HAP coating not only induce the bone growth between implant material and bone but also improve the bonding strength of the implants to the bone [4]. However, the poor mechanical properties such as low fracture toughness and low modulus of elasticity of HAP hindered its application as a load bearing implant [5]. For this reason, HAP coatings have been deposited on mechanically strong and biocompatible metallic materials such as titanium and its alloys [6-9]. This approach combines the good bioactivity of HAP and mechanical advantage of metallic materials. Nevertheless, the bonding strength of HAP coating, and its long term stability after implantation are still questionable. An effective approach to solve this problem is to form a composite coating by reinforcing the HAP coating with a mechanically strong second phase, such as Ti [5], Ti6Al4V [10] and carbon nano-tube [11] etc.

Various techniques, such as magnetron sputtering [12], powder metallurgy [3,13], and plasma spraying[14] have been employed to deposit HAP/Ti composite coatings. Among these techniques, plasma spraying is perhaps the most popularly used technique due to its good chemical composition control and high process efficiency. However, because of high temperature involvement during plasma spraying process, the HAP can be converted into secondary calcium phosphate phases such as tricalcium phosphate (TCP), tetracalcium phosphate (TTCP) or calcium oxide (CaO) and the crystallinity of HAP can also be lowered due to rapid solidification [7,15,16]. These non favorable phases and amorphous contents can lead to rapid degeneration and disintegration of the coating and deteriorate the novel biocompatibility of HAP as well as its adhesion to bone. In addition, Ti is easy to be oxidized during plasma spray process, which could also deteriorate the bonding strength between the composite coating and metallic substrate.

To overcome the above mentioned disadvantages, cold gas dynamic spray technique has been applied to deposit biocompatible HAP composite coatings. And some tentative but meaningful results were obtained. For example, Taylor et al utilized cold spray technique to deposit HAP/Ti composite coatings on aluminum substrates and studied the effect of percent of HAP on the thickness, microstructure and bonding strength of deposited coatings [17]. Maev et al deposited HAP/phosphate glass composite coatings by cold spray approach and studied the effect of heat treatment on the crystallinity of deposited coatings [18]. However, due to the low deforming capability of HAP, reports of successful fabrication of composite coatings consisting of HAP and Ti by cold spray technique are few and to the best of our knowledge, the study of in vitro behavior of cold sprayed hydroxyapatite/titanium composite coatings is not available in open literature.

In this study, 20wt% HAP/Ti composite coatings were successfully deposited by cold spray technique. The in vitro immersion behavior of composite coatings as well as pure Ti coatings was investigated in simulated body fluid (SBF) solution and corrosion behavior was characterized by Tafel polarization analysis and cyclic voltammetry tests. Furthermore, bonding strength of the deposits was also evaluated using a pull-off adhesion bond test fixture.

6.3 Experimental Details

6.3.1 Deposition of 20wt% HAP/Ti Composite Coatings

Commercially available pure wrought titanium sheet (98.9%, from Mcmaster-Carr Co, USA) was used as the substrate. Rectangular Ti coupons, 50×36×3 mm^3, cut from sheet materials, were grit blasted with Al_2O_3 particles (36 mesh) and ultrasonically cleaned in acetone for 10 min before cold spraying. Sponge titanium powder (~45 μm) was purchased from Titanium Powder Specialists, Accushape, Inc. Commercial high purity HAP powder (CAPTAL 30, Plasma Biotal Limited, UK) was used at 20wt% level and mechanically mixed with titanium sponge powders. An in-house developed system was utilized to fabricate HAP/Ti composite coatings under optimized spray parameters. The premixed powders were fed by a high pressure powder feeder and accelerated through a converging-diverging nozzle. The nozzle was kept normal to the substrates with a standoff distance of 15 mm. All deposits were manufactured on titanium substrates and the titanium substrates were driven by a robot with a traverse speed ranging from 50 to 400 m/s. The gas pressure and temperature were 35 bars and 700 ^{o}C respectively. For comparison, the pure titanium coatings were also deposited at the same conditions, except a relatively lower gas temperature (500 ^{o}C) employed. The basic scheme and detailed information of the cold spray process are described in literature [19-21].

6.3.2 Phase, Microstructure and Bond Strength Characterization

The microstructural characteristics of powders and coatings were examined using a scanning electron microscope (HITACHI S-2600N SEM). The coatings were cut perpendicular to the coating-substrate interface, hot-mounted, and then polished progressively. The final polishing procedure was performed using colloidal silica with a particle size of 0.04 μm. The samples were then washed in running water and ultrasonically cleaned with acetone. The phase composition of coatings was determined by a RIGAKU MINIFLEX XRD system using Cu Kα. The X-ray data were collected in the 2 θ range of 30-50° in steps of 0.02°. The bonding strength of cold sprayed composite coating to substrate was evaluated using a pull-off adhesion bond test fixture driven by an Instron-type testing machine (Instron 4469) at a speed of 0.05 in/min. Both sides of deposited samples were glued to cylindrical stainless steel shafts of 20mm in diameter and 25 mm in length using instant adhesive glue (Elcometer epoxy E1100S). After assembly, the samples were held perpendicularly and placed in a furnace at 120 ^{o}C for 1 h. Three samples were tested and the mean value of bonding strength was calculated from the fracture load and the surface area. A photograph exhibiting the testing fixture and a schematic plot describing the failure mode are shown in our previous study [19].

6.3.3 Electrochemical Corrosion Studies

The electrochemical measurements were carried out using a flat three-electrode cell (K0235 Flat Cell, Princeton Applied Research), with the samples acting as the working electrode, Ag/AgCl electrode as the reference electrode and a platinum grid as the counter electrode. The specimen area exposed to the electrolyte solution is 1 cm^2. The simulated body fluid (SBF) used in this study is Hanks' balanced salt solution purchased from Mediatech Inc. The composition of Hanks' balanced salt solution is listed in Table1.

Electrochemical corrosion properties were determined by using a Solartron SI 1287 potentiostat. Prior to each measurement, all samples (as-received Ti coatings and HAP/Ti composite coatings) were polished progressively until a mirror finish surface was achieved. In order to avoid the possible oxidation of samples, the electrochemical tests were commenced immediately after immersion of the samples in Hanks' solution. For Tafel analysis, the working electrodes were polarized from -0.8 V (Vs. reference electrode potential) to 0.5 V at a scan rate of 0.1667 mV/s. The cyclic voltammetry curves were obtained in the potential range of -1 V to 3.5 V with the scan rate of 1 mV/s. CorrWare software was used to determine the corrosion potential (Ecorr), corrosion current (Icorr) and polarization resistance (Rp). All the experiments were carried out at least three times under ambient temperature.

6.3.4 Immersion Test of Deposited Coatings in Hanks' Solution

The coated specimens were immersed in vials with 50 ml of Hanks' solution. The experiment was performed at 37 ^{o}C and the vials were sealed to remain sterile. After certain periods of time, the specimens were removed from Hanks' solution, washed with distilled water and dried at room temperature. Then, the morphological and elemental analysis of the coatings was studies by SEM/EDX.

6.4. Results and Discussion

6.4.1. Characterization of 20wt% HAP/Ti Composite Powders and Coatings

The morphology of mixed HAP and Ti composite powders is shown in Fig.6.1. The white elongated particles are Ti and the gray spherical particles are HAP. Detailed examination revealed that the particles of HAP powder (~ 30 μm) are porous and some of them were crushed into small pieces during mixing process.

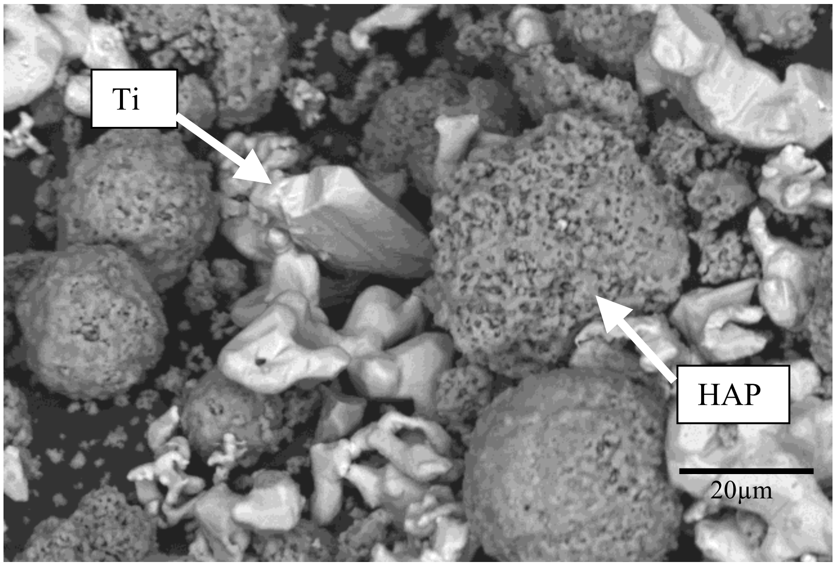

Fig.6.1 Morphology of HAP/Ti composite powders

Table 6.1 Ecorr, Icorr and Rp obtained from polarization curves by Tafel extrapolation method

Sample	E_{corr} (mv)	I_{corr} ($\mu A/cm^2$)	Rp ($k\Omega\ cm^2$)
Ti coating	-241.9	0.362	72.1
HAP/Ti coating	-379.9	0.934	27.9

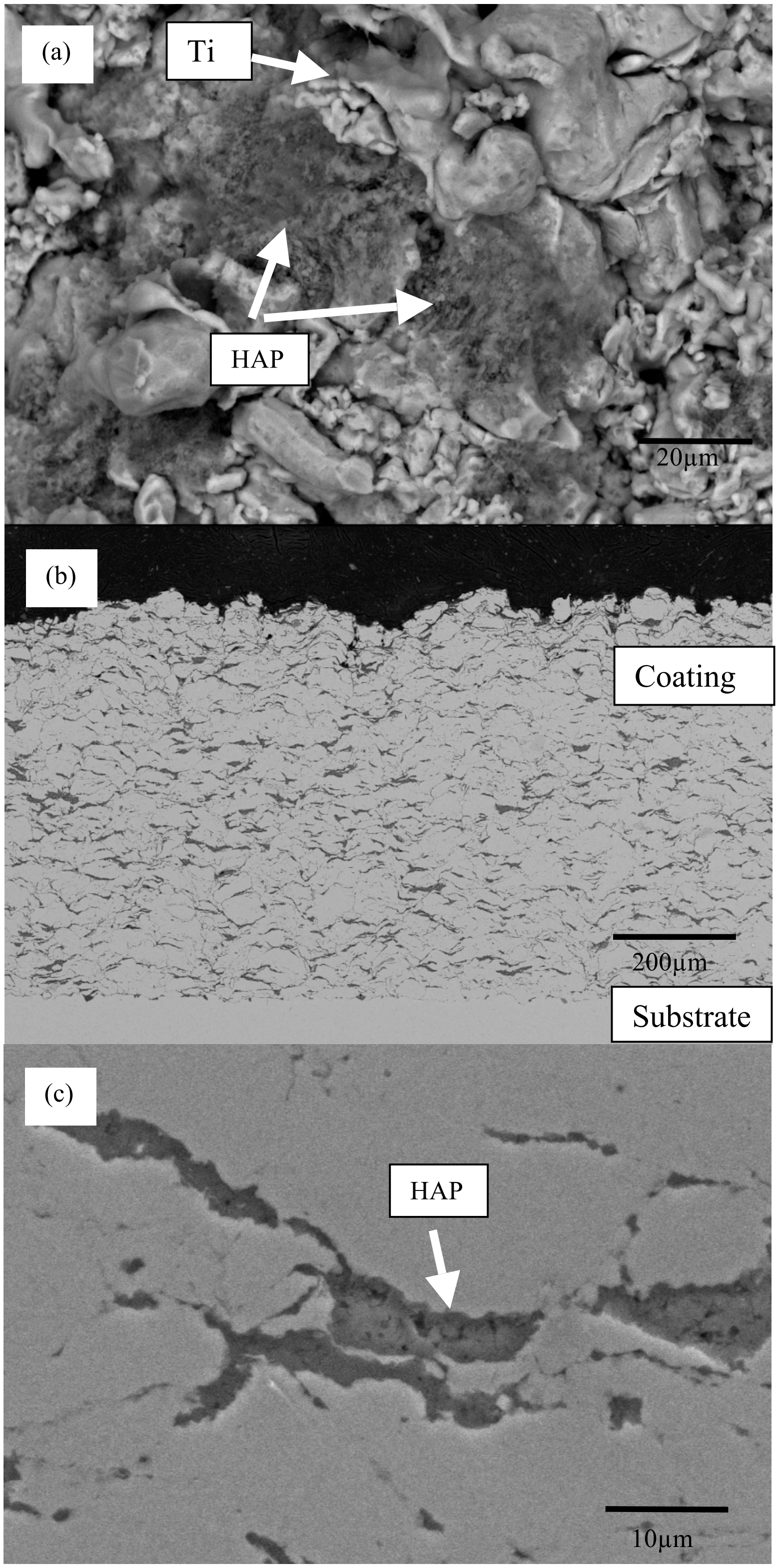

Fig.6.2 Microstructure of 20wt% HAP/Ti composite coatings: (a) Surface morphology of composite coating; (b) Cross section view of composite coating; (c) High magnification view of composite coating in Fig.6.2(b)

Fig.6.2a shows the surface morphology of as-sprayed 20wt% HAP/Ti composite coating. It is composed of two distinguished parts: Ti part and HAP part. Different with plasma sprayed coating, it shows a very rough, non-melted structure. Ti particles on the surface of the coating did not deform significantly and spherical HAP particles got crushed into small fragments due to high impact. Both little deformation of Ti, thus the irregular shape of Ti particles is kept, and crushed HAP particles increased the surface roughness of the composite coating. The high surface roughness provides the nucleation sites with lower interface energy for bone-like apatite to anchor [10, 22]. Fig.6.2b shows the cross-section structure of 20wt% HAP/Ti composite coating. Energy dispersive x-ray (EDX) spectroscopy analysis indicates that the darkish gray area is HAP and the light gray area is Ti. It is observed that HAP was successfully deposited in Ti matrix and a dense, homogenous coating was obtained. The encapsulation of HAP particles within the Ti matrix is shown in Fig.6.2c. HAP particles were nicely compacted. Image analysis indicated that these coatings encapsulated nearly 16% HAP and 4% HAP powder from the powder mixture was lost during the deposition process.

The bonding strength of as-sprayed composite coatings is averaged to 24.5 MPa. Note that this value is significantly higher than that of plasma sprayed monolithic HAP coatings [14]. Three plausible causes could explain the high bond strength of cold sprayed HAP/Ti composite coatings. First is the mechanical interlock among Ti particles within the coatings and good adhesion between Ti splats with Ti substrate. Secondly, low thermal residual stress due to low temperature of cold spraying also contributes improvement of bond strength of coatings. At last, the observed metallurgical bonding [23] at some particle-particle interfaces and particle-substrate interfaces due to cold welding phenomenon is also considered to increase the bonding strength of composite coating.

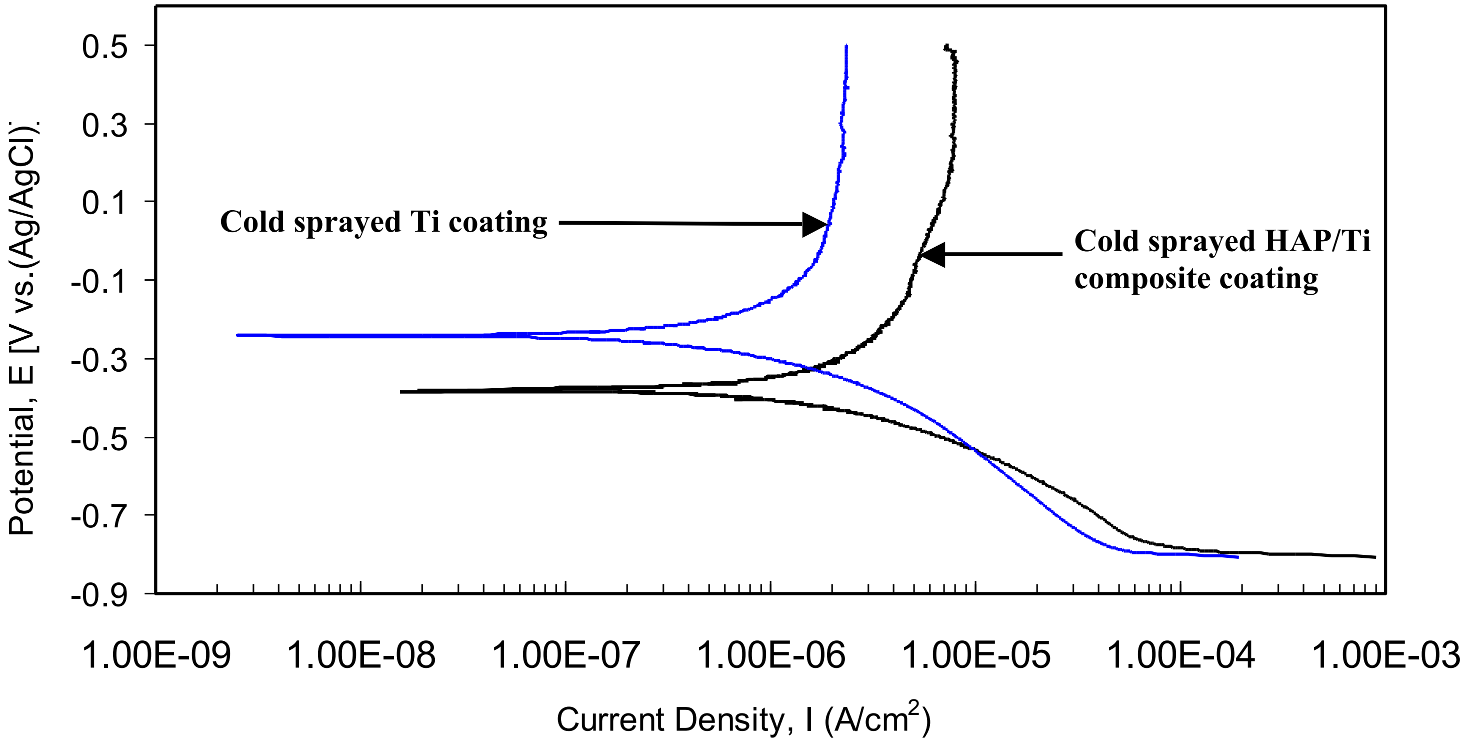

Fig.6.3 Tafel plot for cold sprayed Ti and 20wt% HAP/Ti composite coatings in Hanks' balanced solution

6.4.2 Electrochemical Corrosion Behavior of 20wt% HAP/Ti Composite Coatings

Fig.6.3 presents the Tafel plot for cold sprayed Ti and 20 wt% HAP/Ti composite coatings in Hanks' solution. The corrosion potential (E_{corr}), corrosion current density (I_{corr}) and corrosion resistance (Rp), from polarization curves determined by Tafel extrapolation are shown in Table6.1. Ti coating exhibits higher corrosion potential and bigger corrosion resistance comparing with composite coating, which indicates a better corrosion property of Ti coating[24]. The I_{corr} values of the Ti coating, 20wt% HAP/Ti composite coating are 0.362 $\mu A/cm^2$ and 0.934 $\mu A/cm^2$ respectively. Composite coating has higher corrosion current density than Ti coating. This result indicates that composite coating is kinetically more active than Ti coating. At corrosion potential, the corrosion current is in an equilibrium state and can be considered as an exchange current between coating and Hanks' solution indicating deposition and/or release of Ca^{2+} and/or phosphorous [25]. For sprayed coating, two parameters are considered as main factors that affect the corrosion behavior: porosity and residual stress. In our case, besides these two parameters, the percentage of HA should also be considered. The mechanism of formation of apatite layer on Ti coating and HA coating is different. HAP promotes the formation of new apatite layer compared to Ti. This explains why composite coating has higher corrosion current than Ti coating.

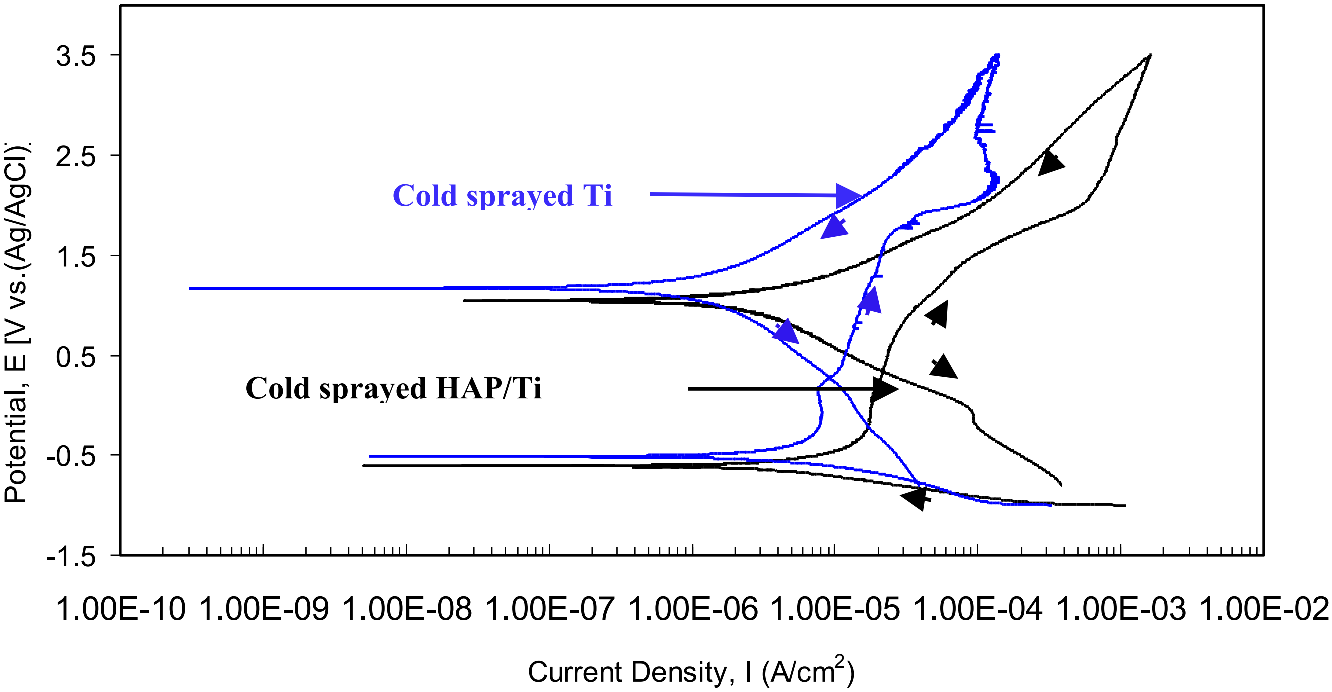

Fig.6.4 Cyclic voltammogram for cold sprayed Ti and 20wt% HAP/Ti composite coatings in Hanks' balanced solution

Fig.6.4 shows the cyclic voltammograms for cold sprayed Ti and 20 wt% HAP/Ti composite coatings in Hanks' solution. It is evident that for both starting and final corrosion potential, Ti coating has relatively higher corrosion potential than HAP/Ti composite coating, which is consistent with previous result of Tafel analysis. Both samples showed obvious passivation zone in a similar potential range of -0.3V to 1.6V, while the composite coating has the higher passivation current. From potential above 1.6V, the anodic current density of Ti coating increased at a faster rate, indicating TiO_2 passive layer breakdown [26] and at a potential around 2.2V, a current oscillation is observed, which typifies a pitting nucleation and re-passivation process. It is noted that the existing pores on the coating surface may extend as pits into the sample. Basically, the cold sprayed coatings are coatings consisted of porous top layer and dense bottom layer [27]. For the cold sprayed 20wt% HAP/Ti composite coating, no obvious pitting corrosion was observed, which indicated a relatively dense and homogenous coating obtained. This is consistent with previous microstructural investigation results.

6.4.3 Immersion Behavior of Composite Coatings in Hanks' Solution

The surface morphologies of 20wt% HAP/Ti composite coatings after immersion in Hanks' solution for various periods are shown in Fig.6.5. It can be seen that after four days of immersion, the top surface of HAP part coating appeared dissolved during immersion; some spherical particles have grown on the top surface of Ti part coating (Fig.6.5a inset picture). The EDX analysis confirmed that Ca, P element contained in these particles. More spherical particles precipitate and the size of the initially precipitated spherical particles increases as immersion duration increases. After one week of immersion, the composite coating surface is found completely covered by a dune like layer with spherical particles embedded inside. The EDX analysis indicates that the layer is apatite layer composed of Ca, P, and O (Fig6.7). It is also found that some microcracks formed in the apatite layer. The occurance of these microcracks is beleived caused by drying shringkage [28] or resulted from diffusion and reaction between coating and Hanks' solution[9]. When the immersion time was increased to two weeks, the layer becomes dense and the granular particles in the apatite layer grows further. The EDX analysis also shows the increase of the intensity of P, Ca elements after two weeks of immersion compared to that of one week of immersion (Fig6.7), which indicates the newly formed apatite layer becomes thicker with elongation of the immersion duration. After three weeks, many granular particles nucleate and precipitate in the initially formed apatite layer, which indicates the continuous growing ability of apatite layer (Fig6.5d).

The immersion behavior of cold sprayed pure Ti coating in Hanks' solution is also investigated for comparing purpose and the results are presented in Fig.6.6. After 5 days of immersion (Fig.6.6a), a crystalline structure is observed precipitated on the surface of Ti coating. Detailed examination ((Fig.6.6a inset picture) revealed its dendritic shape. The corresponding EDX result shown in Fig.6.8 confirmed the presence of elements such as Ca, P and O. With immersion time prolonged to 12 days, a dense layer with spherical particles inside formed on some Ti particles surface. Some microcracks are also observed on the newly formed layer. However, unlike the EDX results for composite coating, elements such as Na, Mg are also detected besides Ca, P and O (Fig.6.8). It can be seen from Fig.6.6c that after immersion of three weeks, the newly formed layer became denser and more crystalline structures precipitate. However, compared with apatite layer formed on composite coating, this newly formed layer on pure Ti coating shows different morphology: more like precipitated crystalline structure with dendritic shape not dune like apatite layer. Fig6.6d shows the low magnification view of Ti surface after immersion of three weeks. As it is shown, the newly formed layer occupies part of Ti surface. This result indicates that some parts of the pure Ti coating are more active than the others.

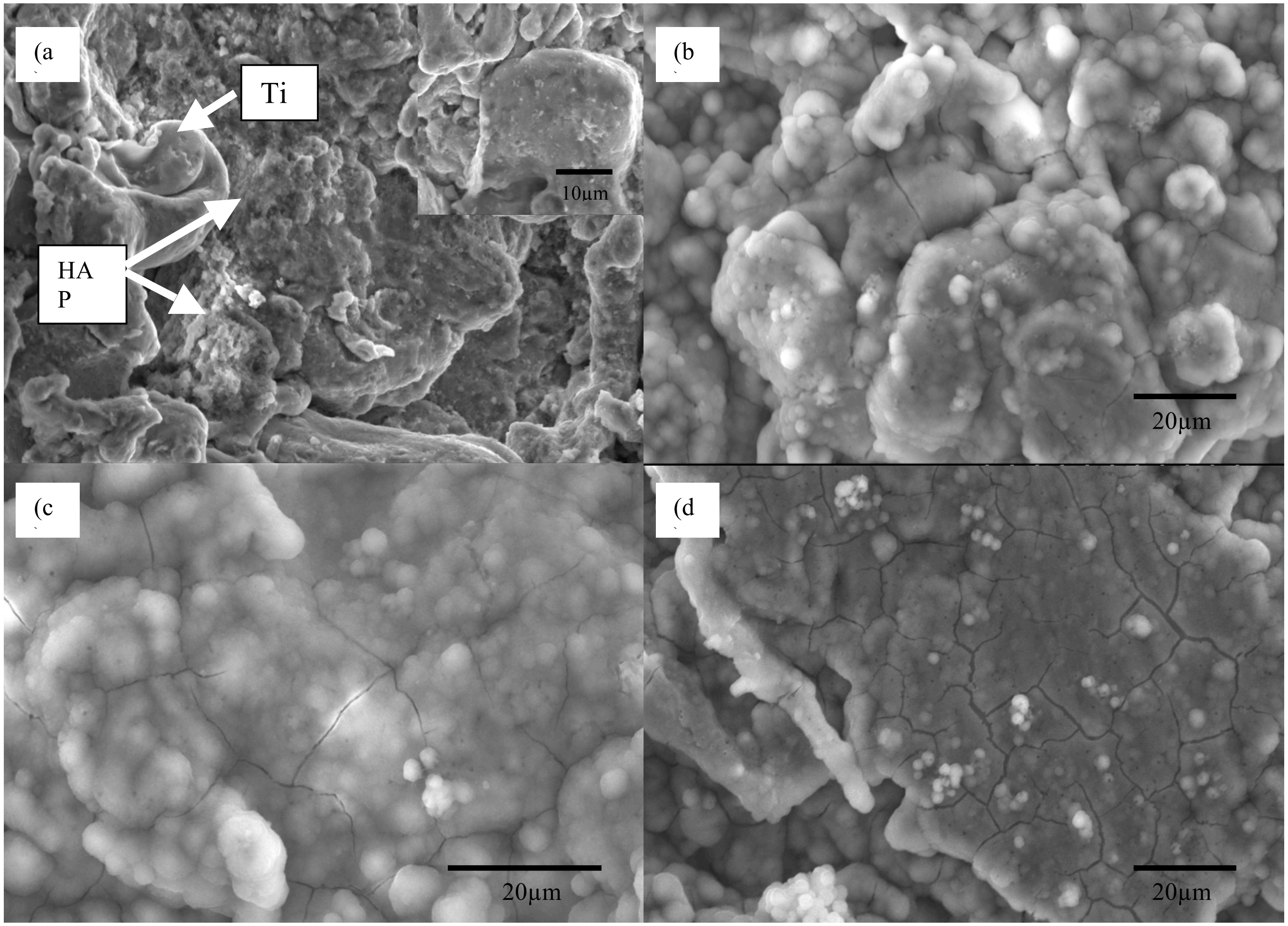

Fig.6.5 Surface morphologies of 20wt% HAP/Ti composite coatings after immersing in Hanks' solution for various periods of time: (a) four days (inset is high magnification image showing the spherical apatite particles formed on surface of Ti part coating); (b) one week; (c) two weeks; (d) three weeks

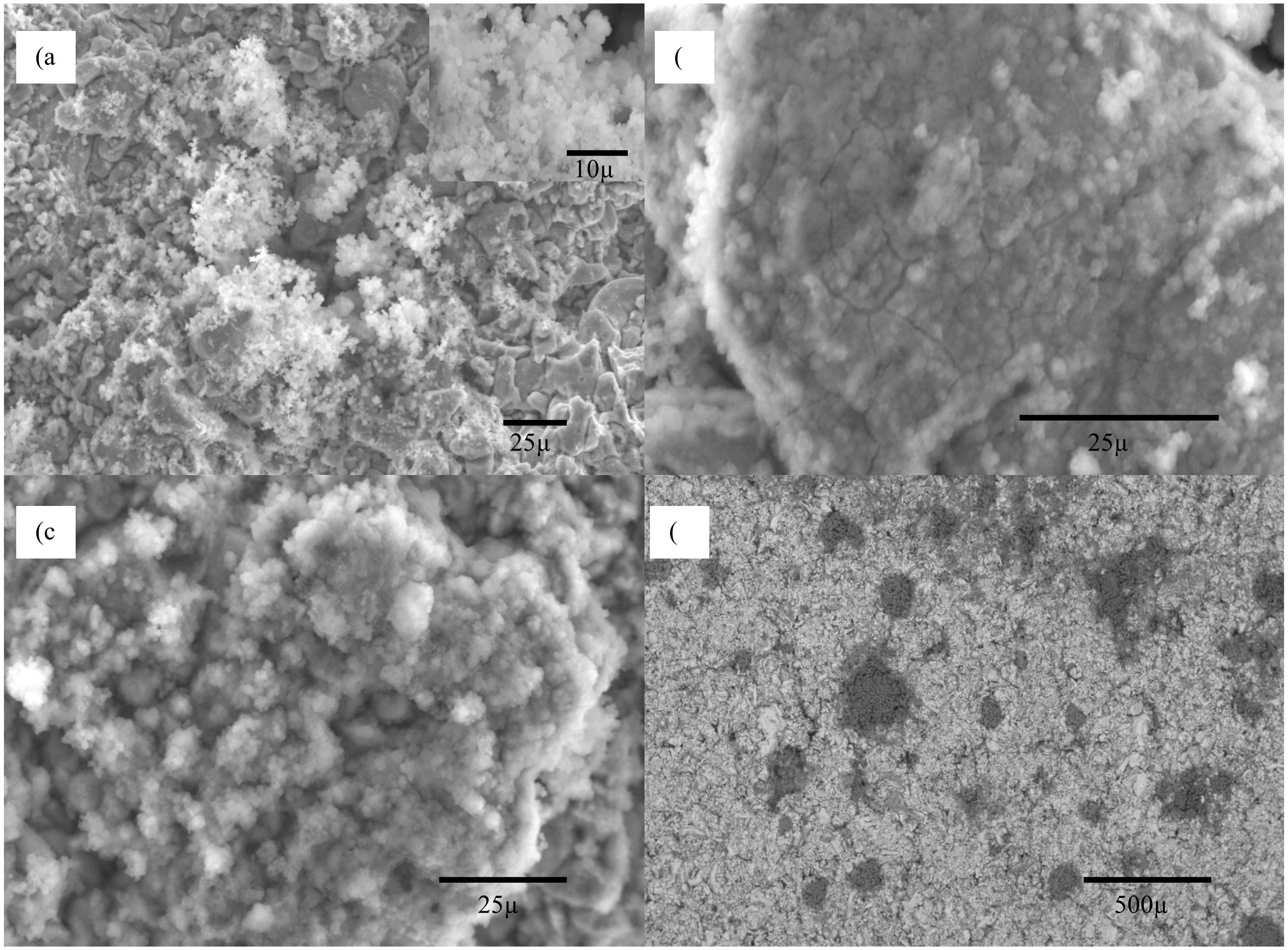

Fig.6.6 Surface morphologies of pure Ti coatings after immersing in Hanks' solution for various periods of time: (a) five days (inset is high magnification image showing the crystalline structure precipitate); (b) twelve days; (c) three weeks; (d) three weeks (low magnification view)

The good bioactivity of cold sprayed HAP/Ti composite coatings is confirmed by the nucleation and growth of a bone-like apatite layer in Hanks' solution. Only 20wt% HAP contained in our coatings is sufficient to induce the formation of apatite layer in Hanks' solution and the addition of Ti does not distinctly affect the formation of apatite layer. A query on highly crystalline HAP coating deposited by cold spraying may be raised, since highly crystalline HAP coating is difficult to resorb in SBF [29] and an amorphous coating is more beneficial for early stage of bone ingrowth [30]. Our results indicated that the nucleation of apatite particles on Ti part coating (Fig.6a inset picture) may stimulate the nucleation of apatite particles on highly crystalline HAP part coating. Highly crystalline HAP promotes the growth of these nucleated apatite particles to form an apatite layer to cover the entire surface of composite coating. One may argue that the naturally formed TiO_2 is not bioactive enough to induce Ca-P precipitation [31]. For cold sprayed coating, due to the porous nature of top layer, TiO_2 thin films with porous structure are expected to form on the top surface of coating in Hanks' solution. And the bioactivity of TiO_2 with porous structure has been proved by Li et al, which could lead to Ca-P deposition [32]. The correlations and effects between formation of apatite layer on HAP and Ti part coating deserved more investigations. In addition, for cold sprayed pure Ti coating, although a newly formed layer containing elements of Ca, P and O was observed after immersion of three week, morphology different with traditional dune like apatite layer was obtained. Whether osteoblasts can proliferate on this newly formed layer on pure Ti coating and let the bone matrix integrates into it need more studies in vivo experiment.

Commercially, HAP powders ($395/kg, Plasma Biotal Limitted) are much more expensive than Ti powders ($85/kg, Accushape, Inc). Compared to plasma sprayed 100wt% HAP coating and HAP/Ti composite coating with 80 and 40wt% HAP [33], only 20wt% HAP used in our cold spraying method could reduce the cost greatly.

6.5 Conclusions

In chapter, 20wt% HAP/Ti composite coatings have been successfully deposited by cold spray technique, without compromising the phase constituents of HAP. The bond strength of the composite coating compared or exceeded the reported values of comparable plasma sprayed coating. A relatively higher corrosion current of composite coating than that of Ti coating indicates a good bioactivity of composite coating, which is consistent with the results of in vitro immersion test. After one week of immersion, a dune like apatite layer was observed on the surface of 20wt% HAP/Ti composite coating and the apatite layer became denser and thicker with the increase of immersion duration. The present results indicate the potential applications of cold sprayed HAP/Ti composite coatings under load-bearing conditions as well as potential economical effect since only 20 wt% HAP used in the coatings.

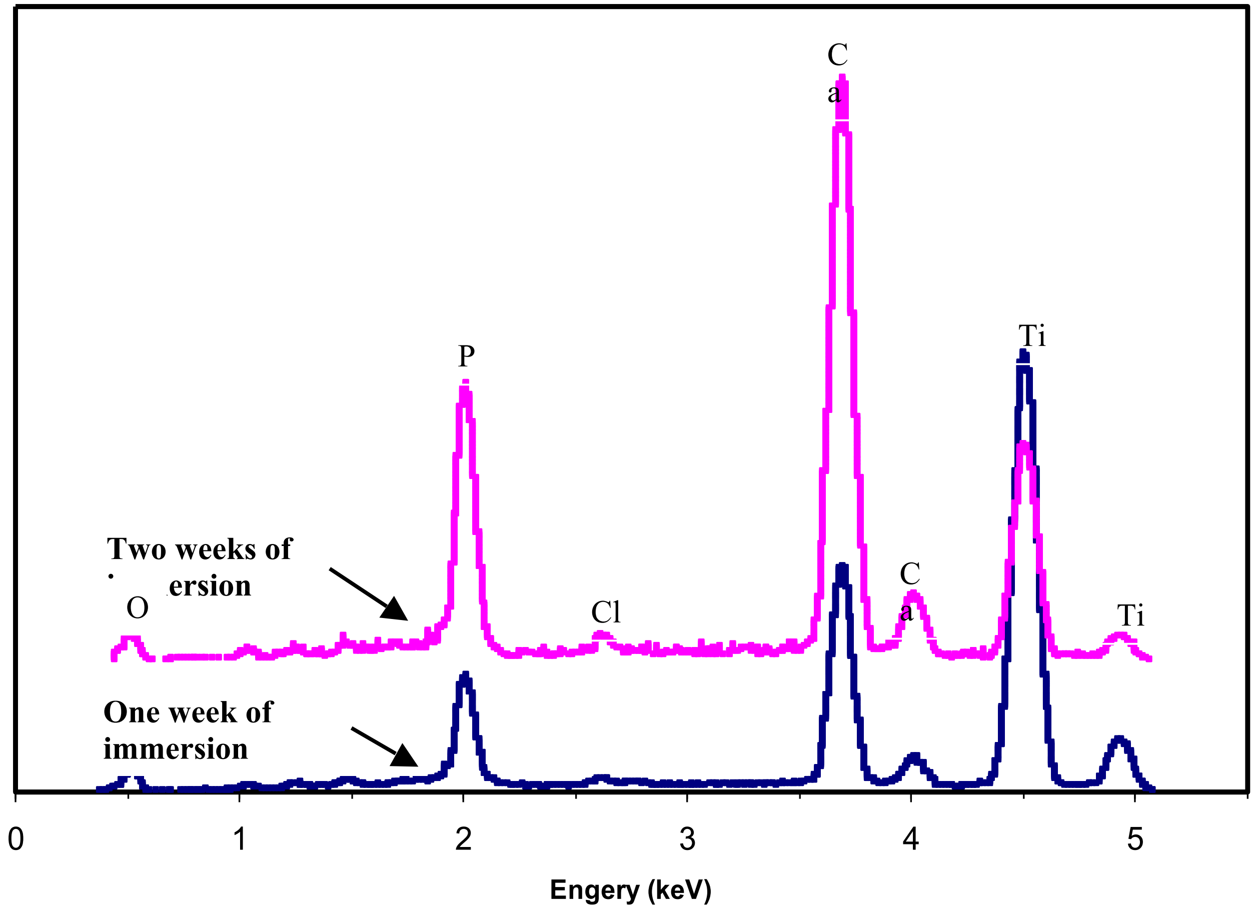

Fig.6.7 EDX spectra of the 20wt% HAP/Ti composite coating after one and two weeks immersion

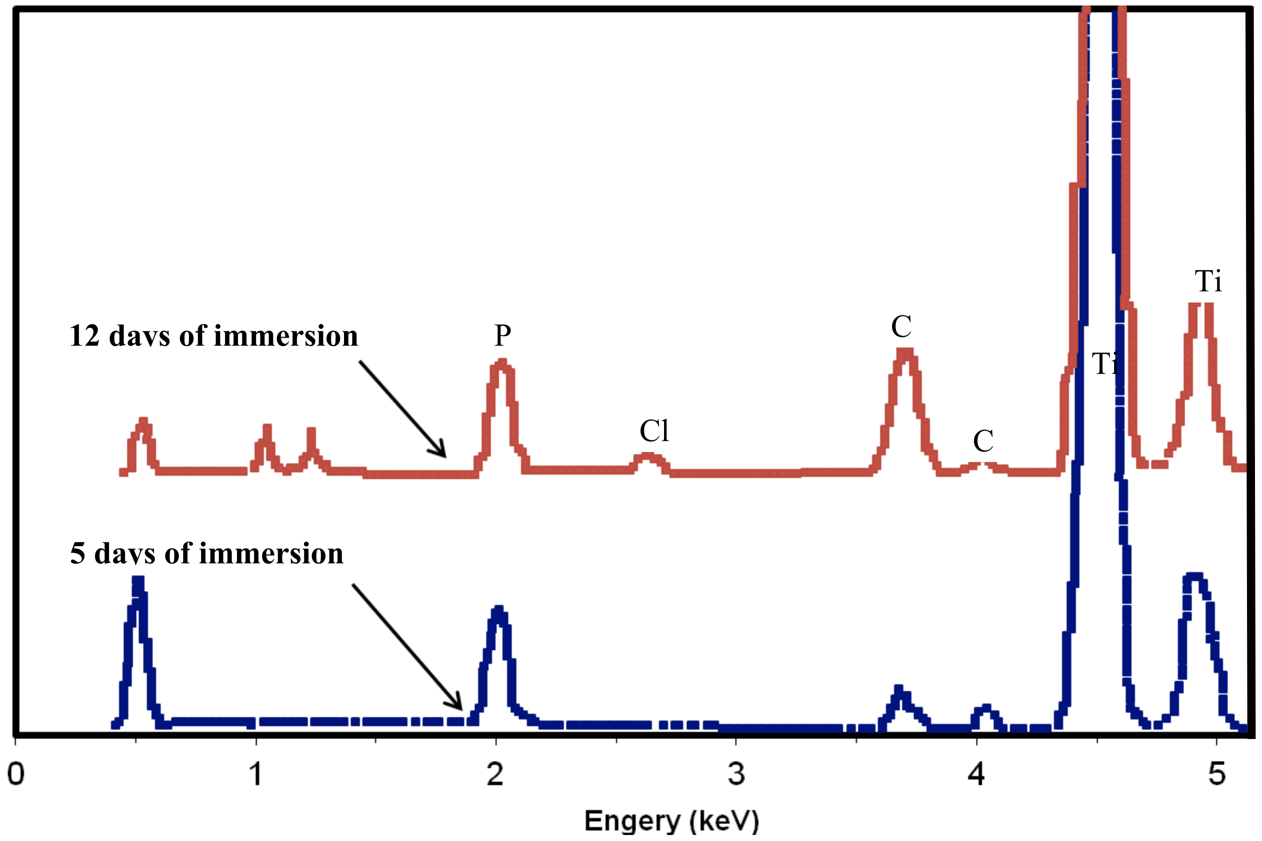

Fig.6.8 EDX spectra of the pure Ti coating after 5 days and 12 days of immersion

References:

[1] M.F. Morks, N.F. Fahim, A. Kobayashi, *Appl Surf Sci* 255 (2008) 3426.

[2] Yanfeng Dai, Min Xu, Junchao Wei, Haobin Zhang, Yiwang Chen, *Appl Surf Sci* 258 (2012) 2850.

[3] C.Q. Ning, Y. Zhou, *Biomaterials* 23 (2002) 2909.

[4] R.S. Lima, K.A. Khor, H. Li, P. Cheang, B.R. Marple, *Mater Sci Eng A* 396 (2005) 181.

[5] Won-Gi Kim, Han-Cheol Choe, *Thin Solid Films* 519 (2011) 7045.

[6] M. Metikos-Hukovic, E. Tkalcec, A. Kwokal, J. Piljac, *Surf. Coat. Technol.* 165 (2003) 40.

[7] Y.C. Tsui, C. Doyle, T.W. Clyne, *Biomaterials* 19 (1998) 2031.

[8] S.W.K. Kweh, K.A. Khor, P. Cheang, *Biomaterials* 21 (2000) 1223.

[9] S.W.K. Kweh, K.A. Khor, P. Cheang, *Biomaterials* 23 (2002) 775.

[10] Y.W. Gu, K.A. Khor, P. Cheang, *Biomaterials* 24 (2003) 1603.

[11] Kantesh Balani, Rebecca Anderson, Tapas Laha, Melanie Andara, Jorge Tercero, Eric Crumpler, Arvind Agarwal, *Biomaterials* 28 (2007) 618.

[12] Shinn-Jyh Ding, *Biomaterials* 24 (2003) 4233.

[13] Congqin Ning, Yu Zhou, *Acta Biomaterialia* 4 (2008) 1944.

[14] Chun-Cheng Chen, Tsui-Hsien Huang, Chia-Tze Kao, Shinn-Jyh Ding, *J. Biomed. Mater. Res. Part B: Appl Biomater* 78B (2006) 146.

[15] Shinn-Jyh Ding, Tsui-Hsien Huang, Chia-tze Kao, *Surf. Coat. Technol.* 165 (2003) 248.

[16] Jiyong Chen, J.G.C. Wolke, K. de Groot, *Biomaterials* 15 (1994) 396.

[17] K. Taylor, B. Jodoin, J. Karov. Utilization of composite powders to apply ceramic coatings in cold spray, *the 5th International Surface Engineering Congress*, Washington State Convention Center, Seattle, Washington, USA, May 15-17, 2006; ASM International, p. 124.

[18] R.Gr. Maev, H. Weinert, E. Maeva, V. Leshchynsky, Poznan-Wasowo. Low pressure gas dynamic spray of hydroxyapatite composite coatings, *the 17th International Scientific and Techanical Conference*, Poland, Sept. 22-24, 2008; Design and Technology of Drawpieces and Die Stampings.

[19] A. Choudhuri, P.S. Mohanty, J. Karthikeyan, *ASM international* 2009, 391

[20] F. Gartner, T. Schmidt, T. Stoltenhoff, H. Kreye, Recent Developments and Potential Applications of Cold Spraying, *Adv. Eng. Mater.* 8 (2006) 611.

[21] T. Hussain, D.G. McCartney, P.H. Shipway, T. Marrocco., *J. Therm. Spray Technol.* 20 (2010) 260.

[22] J. Weng, Q. Liu, J.G.C. Wolke, D. Zhang, K. de Groot, *J. Mater. Sci. Lett.* 16 (1997) 335.

[23] W.-Y. Li, C. Zhang, H.-T. Wang, X.P. Guo, H.L. Liao, C.-J. Li, C. Coddet, *Appl. Surf. Sci*. 253 (2007) 3557.

[24] X. Zhou, P. Mohanty, *Corros. Eng. Sci. Techn.* 47 (2012) 145.

[25] Jianhui Xie, Ben Li Luan, *J. Mater. Res.* 23 (2008) 768.

[26] Robert Wen-Wei Hsu, Chun-Chen Yang, Ching-An Huang, *Mater. Sci. Eng. A* 380 (2004) 100.

.

[27] Chang-Jiu Li, Wen-Ya Li, Deposition characteristics of titanium coating in cold spraying, *Surf. Coat. Technol.* 167 (2003) 278.

[28] Y.W. Gu, K.A. Khor, D. Pan, P. Cheang, *Biomaterials* 25 (2004) 3177.

[29] K.A. Gross, C.C. Berdt, *J. Mater. Sci. Mater. Med.* 5 (1994) 219.

[30] Suzanne H. Maxian, Joseph P. Zawadsky, Michael G. Dunn, *J. Biomed. Mater. Res.* 27 (1993) 111.

[31] Tadashi Kokubo, Fumiaki Miyaji, Hyun-Min Kim, Takashi Nakamura, *J. Am. Ceram. Soc.* 79 (1996) 1127.

[32] Li P, Ph.D Thesis, *Leiden University*, The Netherlands, 1993.

[33] Xuebin Zheng, Minhui Huang, Chuanxian Ding, *Biomaterials* 21 (2000) 841.

Chapter 7

Argon atmospheric plasma sprayed hydroxyapatite/Ti composite coating for biomedical applications

7.1 Abstract

20wt% hydroxyapatite/Ti composite coatings were fabricated via an in-house developed argon atmospheric plasma spraying (AAPS) system on Ti substrates. The phase and morphologies of the coatings were identified by X-ray diffraction and scanning electron microscopy. The electrochemical corrosion behavior of the coatings was evaluated in a simulated biomedical environment by using potentiodynamic polarization and electrochemical impedance spectroscope techniques. The bioactivity of the composite coatings was studied by immersing the coatings in simulated body fluid (SBF) for up to 8 months. The mechanical properties such as microhardness, friction and bonding strength were also investigated. Results demonstrate that dense composite coatings with a typical morphology of HAP homogenously distributed in Ti matrix are obtained and the decomposition of HAP during plasma spraying process is avoided. The bonding strength is significantly higher than that of HAP or Ti reinforced HAP coatings and the frictional property is comparable to Ti substrate. A relatively higher corrosion current of HAP/Ti composite than that of pure Ti coating in simulated body fluid indicates a good bioactivity for composite coating, which is also testified by the formation of apatite layer in vitro test. After eight months immersion, a thick, tortoise-shell like apatite layer covered the entire top surface of composite coating. The study indicates the potential of AAPS deposited HAP/Ti composites as load bearing implant materials.

7.2 Introduction

Titanium and its alloys have been widely used as dental and implant materials because of their good mechanical properties and high corrosion resistances, but they are not showing very good osteo-conductivity [1-3]. Hydroxyapatate (HAP) has received continuous attention as biomedical materials to promote accelerated osteo-integration with bone because of its physical and chemical similarities with bone tissues [4-6]. However, as a type of bio-ceramic materials, the low ductility of HAP limits its application as load bearing materials. In order to combine the good mechanical properties of Ti based metals with excellent biocompatibility and bioacticity of HAP, various coating techniques such as plasma spraying [7-10], sol-gel processing [11,12], electrical polarization [13], high velocity oxy-fuel (HVOF) spray [14-15] and aerosol deposition [16] have been applied to deposit HAP coating onto Ti or its alloy substrate. Nevertheless, the long-term stability of HAP coating in body environment is still questionable. In order to maintain its long-term stablity, two requirements are commonly needed to fulfill: first, HAP coating itself should have good mechanical properties, e.g., high hardness, low friction etc; second, the bonding strength of interface between HAP coating and metallic substrate should be high enough to sustain possible fatigue stress during surgical operation or after implantation. To overcome above mentioned problems, two creative ways have been brought out. One is to reduce the particle size of HAP to nanoscale level to gain superior biological and biomechanical properties [17]. Huang et al use liquid precursor plasma spray process to manufacture nano-structured HAP coatings [18]. Cheang et al studied nanostructure and pore formation mechanisms of thermal sprayed HAP splats by utilizing both HVOF and direct current plasma spray techniques [14, 19].

The other is to use various coating techniques to make bio-composite coatings by adding biocompatible second phase such as Ti [6, 20-24], TiO_2 [15, 25, 26], Ti6Al4V [27-29], carbon nanotube [16, 30] to reinforce the HAP.

Among all these techniques, plasma spraying has been successfully used as a reliable cost-effective solution and attracted much attention in recent years. However, because of high temperature involved during plasma spraying process, readily oxidized element such as Ti is easy to be oxidized, which might impair the bonding between Ti particle and Ti substrate. In order to solve this problem, plasma spraying at vacuum or low pressure condition is studied [31-33]. Controlled atmosphere plasma spraying (CAPS) technique has also been applied to study the deposition of HAP coatings [34, 35]. However, to the best of our knowledge, the spaying process carried out in argon atmosphere to deposit 20wt% HAP/Ti composite coatings is still not available in the literature. In addition, most researchers add small amount of Ti to HAP to form a structure of Ti particles distributed in HAP matrix, there is limited literature available on the incorporation of HAP into Ti matrix.

In the current study, 20wt% HAP/Ti composite coatings were fabricated by an in-house developed AAPS system. A systematic investigation was carried out to assess the structural, mechanical, electrochemical properties of deposited composite coatings.

7.3 Experimental Details

Commercially available titanium sponge powder (Titanium Powder Specialists, Sandy, UT, USA) and high purity HAP powder (CAPTAL 30, Plasma Biotal Limited, UK) with typical size of ~45 μm and ~30 μm respectively, were mechanically mixed at

HAP percentage of 20 wt% before plasma deposition. Pure titanium coupons at size of 50×36×3 mm^3 (Mcmaster-Carr Co, Robbinsville, New Jersey, USA) were initially grit blasted with Al_2O_3 of mesh size #36, then degreased and ultrasonically cleaned in acetone. An in- house developed argon atmospheric plasma spraying (AAPS) system was applied to fabricate composite coatings under optimized spraying parameters listed in Table 7.1.

Table 7.1 Optimized argon atmospheric plasma spraying parameters

Plasma power	28 kw
Primary Ar gas pressure	50 psi
Secondary He gas pressure	20 psi
Substrate	Ti
Standoff distance	4 inch
Gun moving speed	100 inch/min
Powder feed	1 RPM
Carrier gas flow	4 m^3/h
Chamber pressure	570 Torr

Fig.7.1 shows the schematic view of this system. A robot controlled, 80 kw plasma gun system (SG-100, Praxair Surface Technologies, Inc., Indianapolis, Indiana, USA) was assembled inside a chamber and the whole spraying process occurred under the protection of argon atmosphere. The surface and cross-section microstructures of deposited coatings were examined using HITACHI S-2600N scanning electron

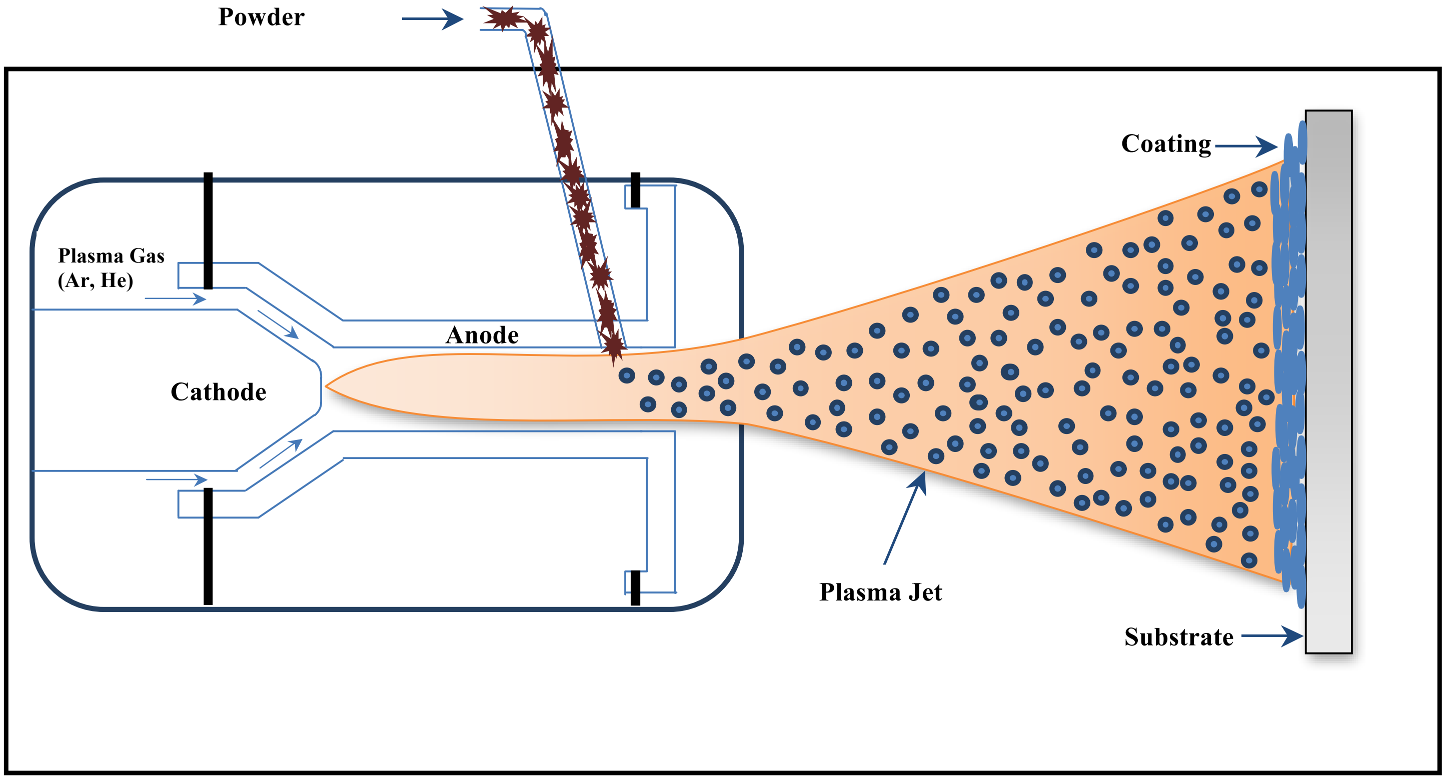

Fig7. 1 Schematic view of argon atmospheric plasma spraying system

microscope (SEM). Phase composition of plasma sprayed coatings were determined from X-ray diffraction (XRD) studies conducted using a Rigaku Miniflex X-ray diffraction machine with a Cu K_α radiation (λ= 1.5402A°).

A flat three-electrode cell (K0235, Princeton Applied Research, Oak Ridge, Tennessee, USA) was used to determine the electrochemical characteristics of AAPS HAP/Ti composite coatings. The electrochemical cell consisted of Ag/AgCl as reference electrode, a platinum plate as counter electrode and the samples as working electrode. Before each experiment, all samples were progressively polished down to 1200 gradation using SiC paper until appearance of a mirror like surface. The samples were then washed in running water and ultrasonically cleaned with acetone. A commercially available simulated body fluid solution (SBF), Hanks' balanced salt solution (Mediatech Inc, Manassas, VA, USA) was used as the electrolyte solution. The composition of this solution is NaCl: 8 g/L, $CaCl_2$: 0.14g/L, KCl: 0.4 g/L, $NaHCO_3$: 0.35 g/L, Na_2HPO_4 (anhydrous): 0.0477 g/L, KH_2PO_4: 0.06 g/L, $MaSO_4$: 0.0977 g/L and D-Glucose: 1g/L. Open circuit potential (OCP), potentiodynamic polarization and electrochemical impedance spectroscopy (EIS) measurements of all samples were carried out using electrochemical workstation -Biologic VMP3 analyzer. The open circuit potential was recorded immediately upon immersion of samples into Hanks' solution until a stable value was reached. The potentiodynamic polarization was applied starting from -1 V to 5 V (vs. OCP) using a scan rate of 1 mV/s. EIS measurements were conducted at open-circuit potential at a frequency range from 0.01 Hz to 10 kHz, with the amplitude of sinusoidal signal set at 10 mV. The recorded impedance spectra were also fitted to deduce the equivalent circuit by using software EC-Lab.

Wear tests of coated and uncoated samples were carried out by using a commercial reciprocating ball-on-disc setup (CSM Tribometer, Switzerland). Ti6Al4V balls of 6 mm diameter were slid at a speed of 60 mm/s to create a 10 mm long wear track. A load of 50 N was applied through the ball for 15000 cycles. Coefficient of friction data was acquired at a rate of 9 Hz. The wear tests were carried out five times for each kind of sample to obtain an average value and standard deviation. After each test, the weight loss was measured using a digital balance (ML54, Mettler Toledo, Switzerland) with an accuracy of 0.1 mg. Hardness tests were performed on polished cross section of coated samples using a Future-Tech, (Tokyo, Japan) Vickers microhardness tester. The measurements were performed with a load of 200 gf applied for a dwell time of 10 s. Each hardness value is the average value of eight tests. The bonding strength of AAPS composite coatings to substrates were evaluated in accordance with ASTM C633 using an Instron-type universal test machine (Instron 4469) at a crosshead speed of 0.05 in/min. Two identical cylindrical stainless steel shafts of 20mm in diameter and 25mm in length were used as a set. Both sides of deposited samples were glued to the shafts using instant adhesive glue (Epoxy E1100S, Elcometer Inc, Rochester Hills, Michigan, USA). The surface of the uncoated side was grit blasted to enhance the adhesion strength. The assembled samples were placed in an oven at 160 ^{o}C for 1 h for thermal curing. Five samples were tested and the average value was presented.

7.4 Results and Discussion

7.4.1 Morphology and Phase Composition

The morphology of mixed HAP and Ti composite powders prepared for plasma spraying is shown in Fig. 7.2(a). The SEM investigation shows that there are two different shapes of Ti particles; relatively large elongated particles mixed with spongy clusters formed by small particles. It has been found that structurally, these two shapes of Ti particles are essentially same, i.e., both have an internal porous structure with pore size ~1.5 μm [36]. For HAP powders, a typical porous and spherical structure is observed. The size of HAP particles is ~30 μm in diameter.

Fig. 7.2(b) shows the cross-section structure of AAPS 20wt% HAP/Ti composite coating. Energy dispersive x-ray (EDX) spectroscopy analysis indicates that the darkish gray area is HAP and the light gray area is Ti. It is observed that HAP is uniformly distributed in Ti matrix and a dense, homogenous coating with a thickness of ~300 μm is obtained. Careful examination reveals that no evidence of microcracks existing, which bears tremendous beneficial for mechanical properties. Fig.7.2(c) shows the encapsulation of HAP particles within the Ti matrix in high magnification. Microscaled molten HAP splats are nicely compacted by Ti splats and no microcracks are observed inside of HAP splats. However, small pores resulted from shrinkage of solidification are observed in the Ti matrix.

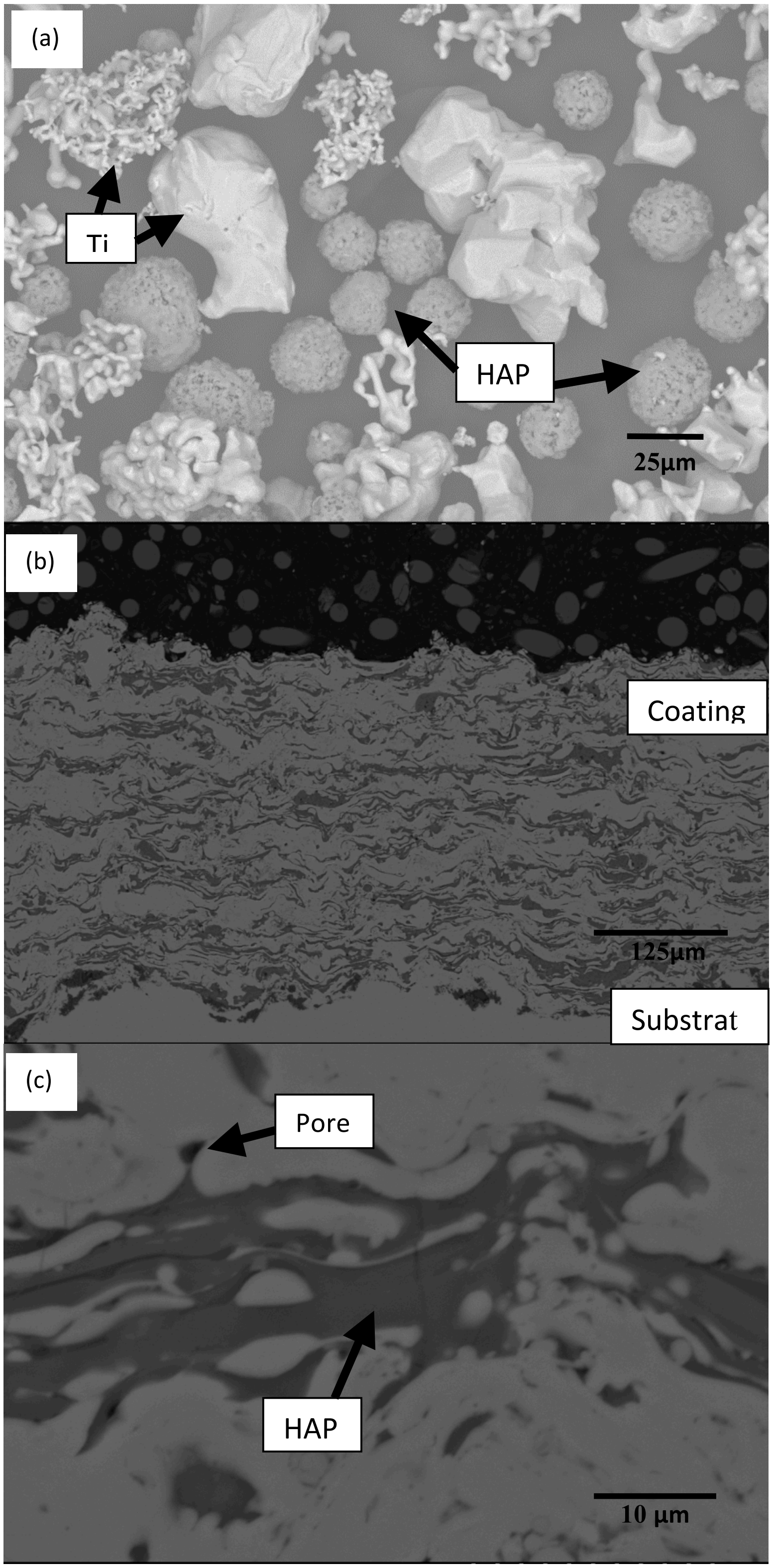

Fig.7.2 SEM images of (a) HAP/Ti precursor powder; (b) cross section view of AAPS 20wt% HAP/Ti composite coating; (c) high-magnification view of (b)

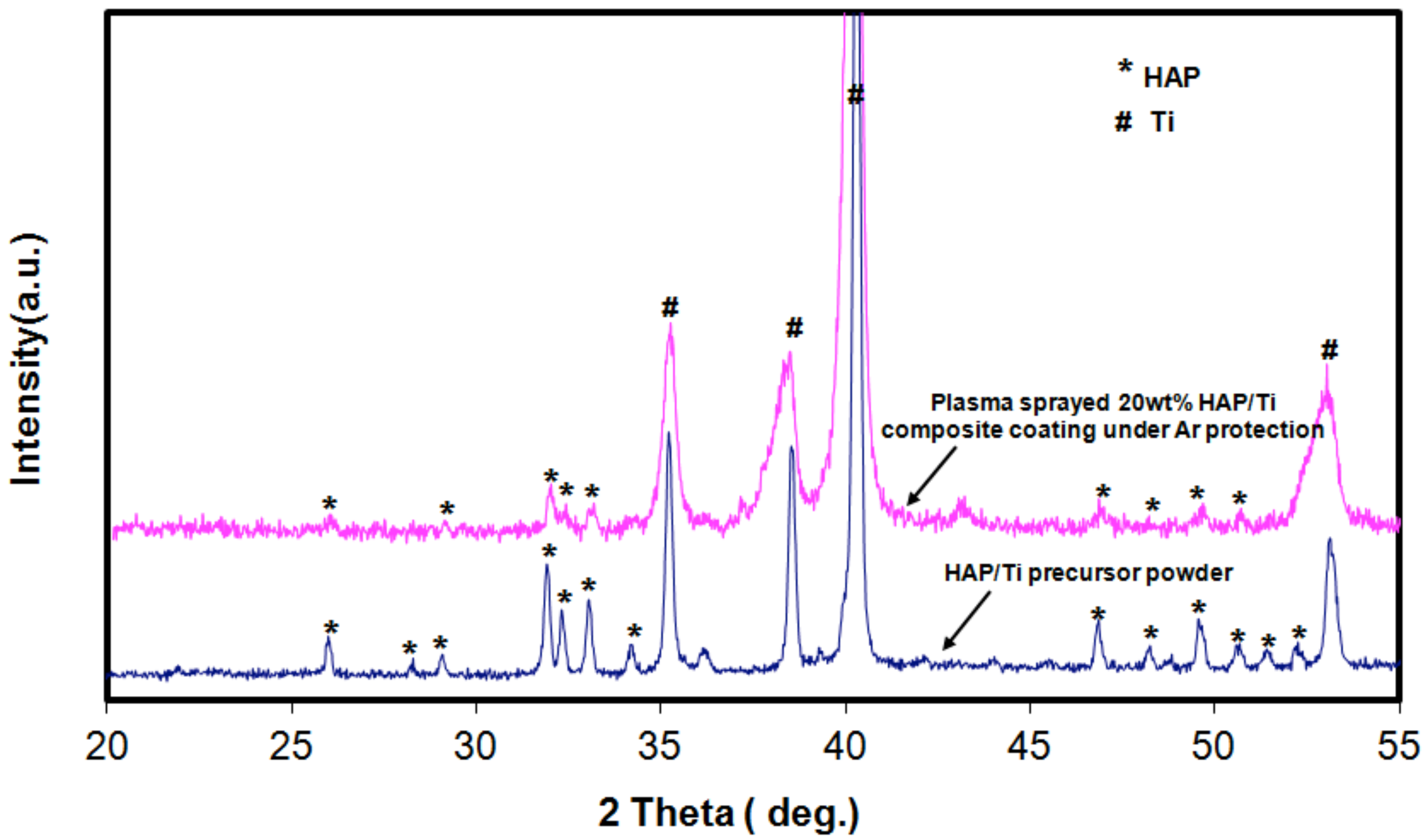

Fig.7.3 X-ray diffraction patterns for AAPS 20wt% HAP/Ti composite coating and 20wt% HAP/Ti precursor powder.

XRD patterns of the composite coatings as well as the precursor powders are shown in Fig.7.3. Compare these two patterns, it is found that the diffraction peaks of both HAP and Ti phases are preserved and no other peaks besides these two phases are shown. This result indicates that the phases of both HAP and Ti powders were not altered during spraying process and the decomposition of HAP particles was avoided. The decomposition of HAP during plasma spraying process mainly comes from extremely high temperature and highly reactive atmosphere [8]. Thus, several approaches have been provided to prevent the decomposition of HAP including using large HAP particles, varying the atmosphere, and controlling the plasma spraying parameters to minimize the time of particle flight [37]. In current study, the inert atmosphere is considered as the main reason of un-decomposition of HAP.

It can also be observed that the peak intensity is reduced and the peak width is broadened after spraying process for both HAP and Ti powders. Due to the high temperature of plasma flame, the precursor powders will likely either wholly or partially melt. The melted portions of particles could solidify to amorphous phase because of rapid cooling, recrystallize, or decompose to impurity because of the highly reactive atmosphere. The un-melted or partially melted particles experienced a refining process due to the fact that the precursor particles might be crushed into small pieces during spraying [38]. The appearance of amorphous phase and refining of initial precursor powders explained the reduction of peak intensity and peak broadening. However, no obvious amorphous hump observed indicates that compared to other researchers' results, the amount of amorphous phase in our particular coating is limited [38].

7.4.2 Electrochemcial Characterization

7.4.2.1 Open Circuit Potential - Time Measurements

The open circuit potential (OCP) – time plots for pure Ti substrate and HAP/Ti composite coating are shown in Fig. 7.4. It can be observed that Ti substrate has a higher OCP than composite coating, which indicates that thermodynamically, Ti substrate is more stable than composite coating. For both samples, the OCP increased toward a nobler potential with time increase and the steady state is reached within one hour. However, it took a longer time to obtain the steady potential for composite coating. It is believed that after Ti is exposed to Hanks' solution, titanium oxide film will spontaneously formed on the surface and result the increase of corrosion resistance [36]. This explained the increase of OCP for pure Ti substrate. The corrosion properties of composite coating are more complex. Composite coating consists of two distinguished parts of coating: Ti part and HAP part. Besides the effect of growth of titanium oxide film on Ti part, the deposition and/or release of Ca^{2+} and/or phosphorous between HAP part and Hanks' solution should also be considered [39]. The combined effect of these two processes determined the corrosion properties of composite coating. A relatively longer time needed to obtain the steady potential for composite coating indicates the process occurred between HAP part coating and Hanks' solution is more active than Ti oxide film growth. In fact, apatite layer is believed initially formed on the HAP part of the coating after immersion in Hanks' solution. Detailed information of apatite layer precipitation can be found in following discussion.

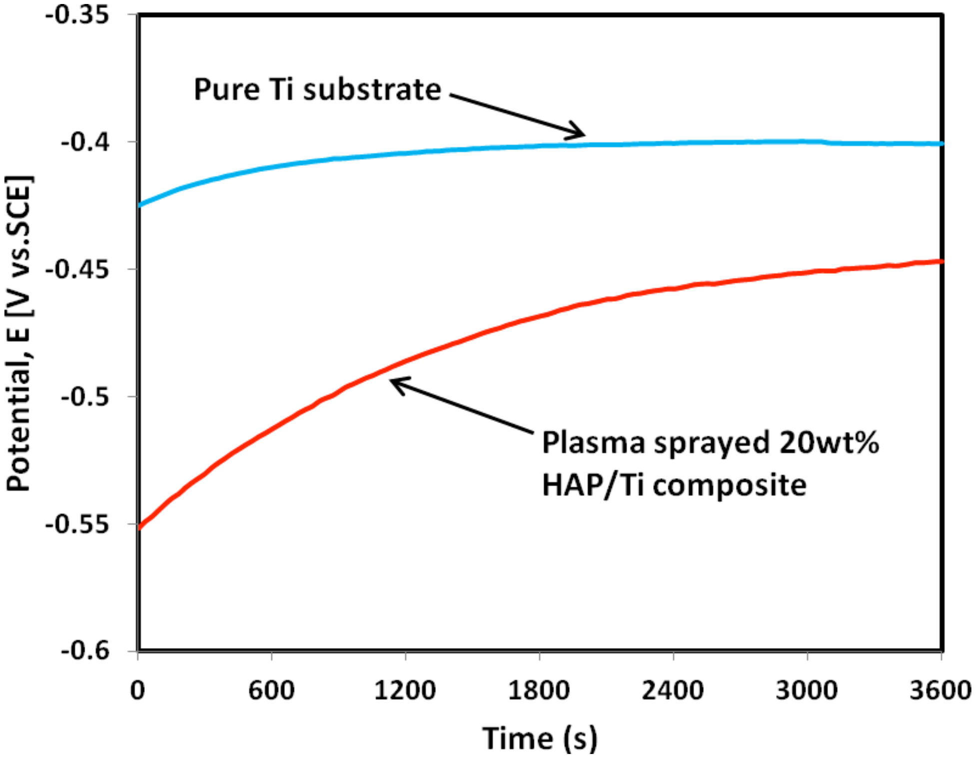

Fig. 7.4 Variation of open circuit potential on immersion in Hanks' solution.

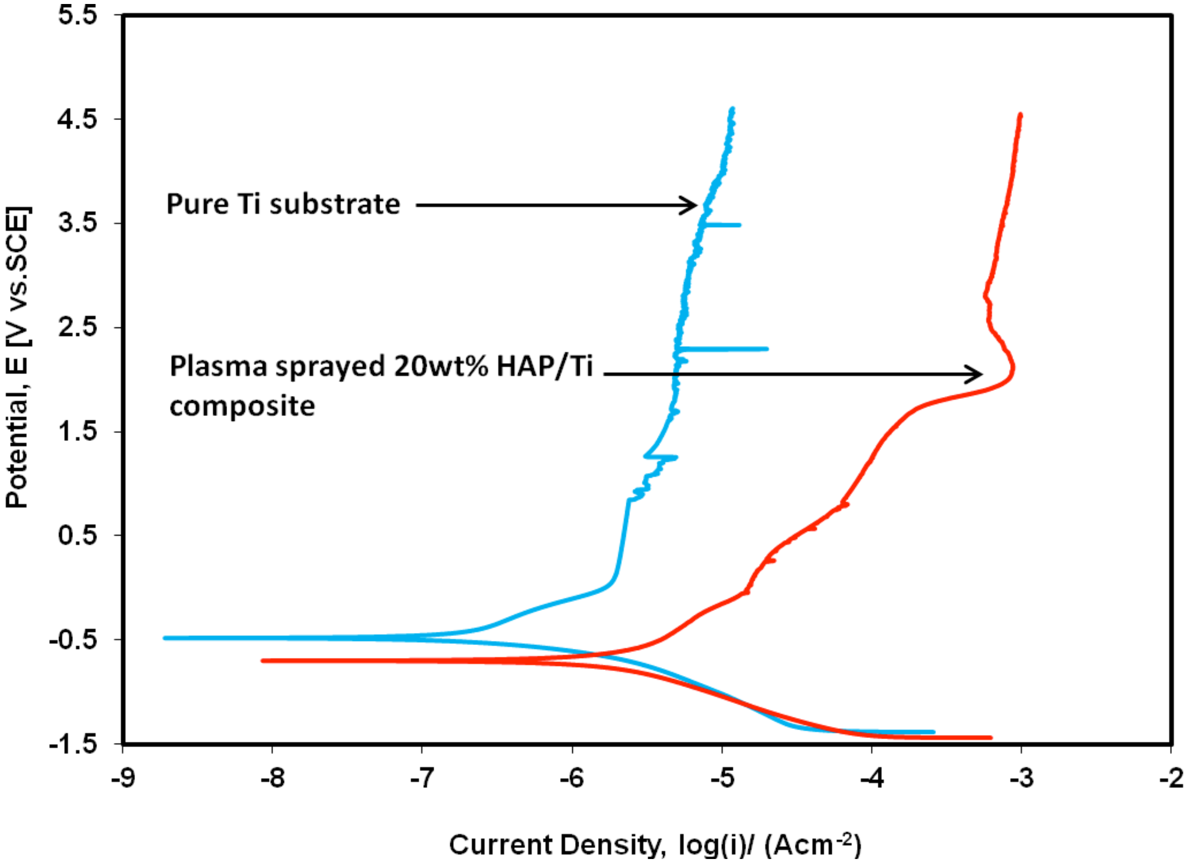

Fig. 7.5 Comparison of potentiodynamic polarization curves of AAPS 20wt% HAP/Ti composite coating and pure Ti substrate

7.4.2.2 Potentiodynamic Polarization

The typical potentiodynamic polarization behavior of pure Ti substrate and AAPS 20wt% HAP/Ti composite coating is shown in Fig.7.5. It is evident that pure Ti substrate has a higher corrosion potential compared to composite coating. This result is consistent with the one of previous OCP test and indicates that pure Ti substrate is thermodynamically more stable in Hanks' solution. An obvious passivation zone is observed for pure Ti substrate in a potential range of 0.3 V to 4.6 V, which indicates that even in a very high anodic potential, pure Ti substrate behaves passive property. For composite coating, from potential above 0.3 V, the anodic current density increases continuously and at a potential around 2V, a current oscillation is observed, which typifies a pitting nucleation and re-passivation process. A similar phenomenon is observed for cold sprayed pure Ti coating [36]. It is also observed that composite coating has higher corrosion current than pure Ti substrate. This result indicates that composite coating is kinetically more active than pure Ti substrate in Hanks' solution. At corrosion potential, the corrosion current is in an equilibrium state and can be considered as an exchange current between coating and Hanks' solution indicating deposition and/or release of Ca^{2+} and/or phosphorous [39]. The mechanism of formation of apatite layer on pure Ti substrate and HAP coating is different. The HAP promotes the formation of new apatite layer compared to pure Ti [40]. This explains why composite coating has higher corrosion current than pure Ti substrate.

The optical microscope image of surface morphology of composite coating after progressive polishing was shown in Fig.7.6(a). After potentiodynamic polarization scan, surface variation of composite coating are shown in Fig.7.6(b) and (c) at low and high magnification. Confirmed with current oscillation observed for composite coating in Fig.7.5, the evidence of the localized corrosion is found in Fig.7.6(b). Similar with pervious study on cold sprayed composite coating [40], an apatite layer is observed precipitating on top of HAP part of the surface.

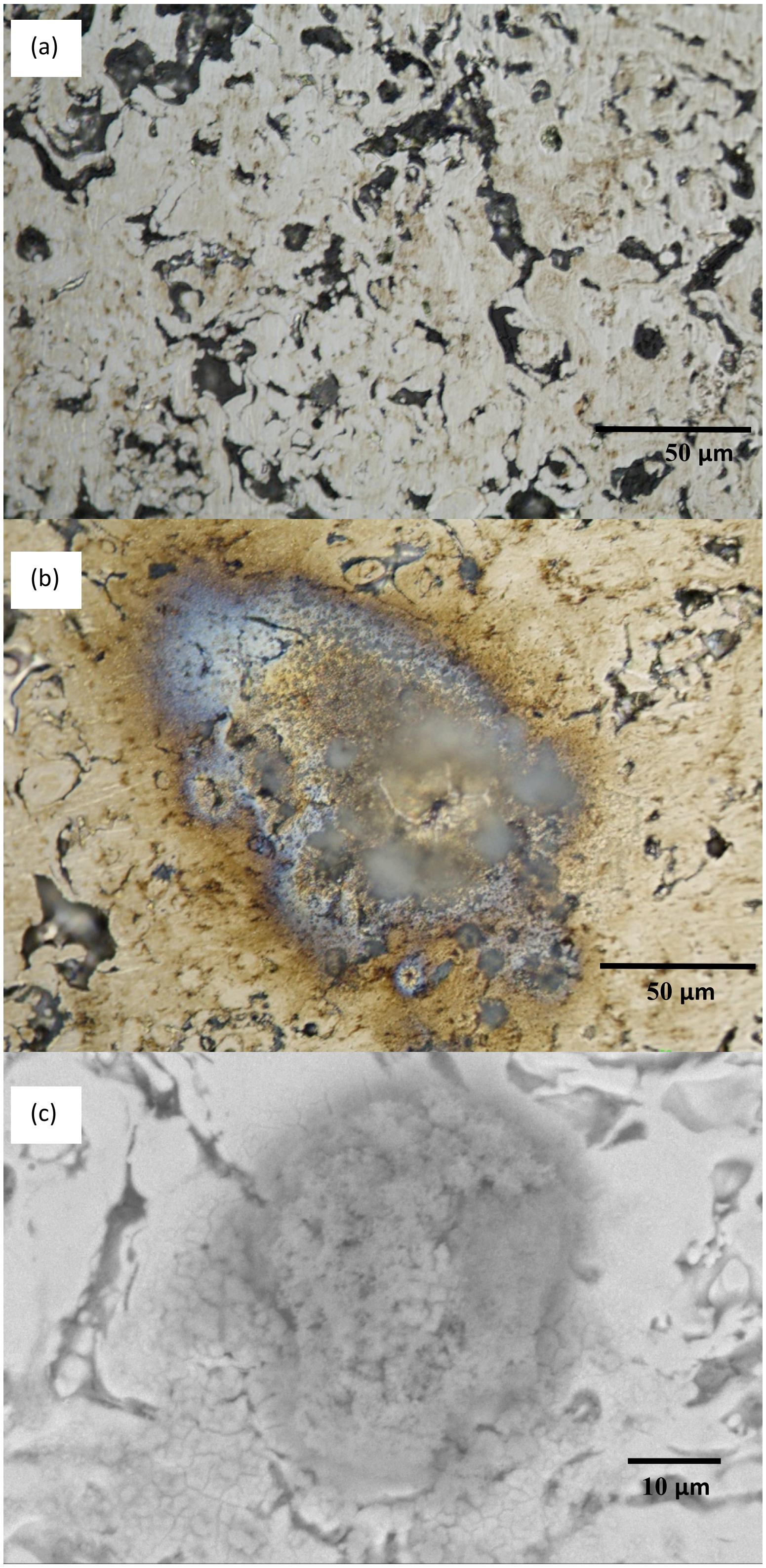

Fig.7.6 Optical microscope images of surface morphology of AAPS 20wt% HAP/Ti composite coating: (a) polished surface (b) corroded surface after potentiodynamic polarization scan (c) high-magnification SEM image showing one of those corroded areas.

7.4.2.3 Electrochemical Impedance Spectroscopy

Fig.7.7 shows the Bode phase angle and impedance modulus diagrams obtained immediately after immersion in Hanks' solution for AAPS 20wt% HAP/Ti composite coating. For comparing purpose, EIS analysis result on pure Ti substrate is also presented [36]. It is observed that one time constant behavior controlled the electrochemical behavior of pure Ti substrate. This time constant presented as a phase hump in Bode phase angle diagram as well as a gradient in the Bode impedance modulus diagram corresponds to the capacitive behavior of pure Ti substrate. The high impedance value at intermediate and low frequency range and phase angle close to -80^{o} at peak point indicate a relatively good corrosion property of pure Ti substrate. This result is consistent with other researchers' results and the good corrosion property is attributed to the single passive oxide film naturally formed on the surface of Ti substrate [41]. For composite coating, the impedance spectra exhibit two time constants although the appearance of the second time constant is not obvious. A typical model of a metallic material covered by a porous coating exposed to electrolytic environment has been successfully used to explain the electrochemical corrosion behavior of cold sprayed composite coating [40]. Different from cold sprayed composite coating, the porosity of the composite coating in current study is relatively less, which results the featureless of the appearance of the second time constant. Both the impedance modulus at lowest frequency and the highest phase angle for composite coating are lower than those of pure Ti substrate. This indicates a relatively poor corrosion protection property but high kinetic activity for composite coating, which is beneficial to the formation of apatite layer on the surface of composite coating after immersion in Hanks' solution.

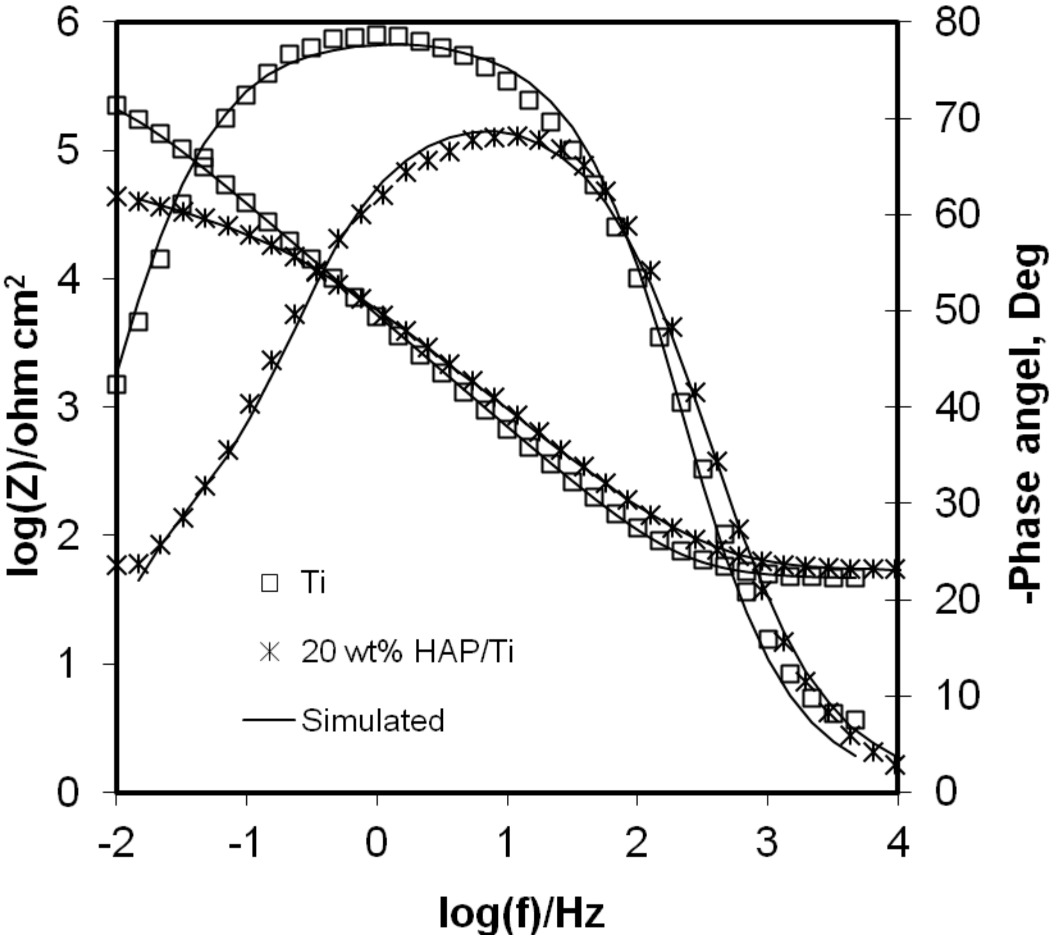

Fig. 7.7 Initial and fitted Bode plot for pure Ti substrate and AAPS 20wt% HAP/Ti composite coating on immediate immersion in Hanks' solution.

(a)

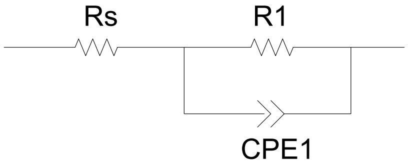

(b)

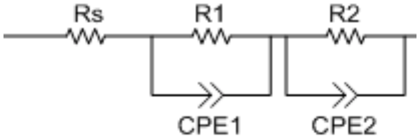

Fig. 7.8 Equivalent circuit model
(a) for pure Ti substrate and
(b) for AAPS 20wt% HAP/Ti composite coating.

The equivalent circuit model used for simulating the impedance spectra are shown in Fig.7.8. The impedance spectra of pure Ti substrate after immersion in Hanks' solution are simulated by a single layer equivalent circuit (Fig.7.8(a)), where R_s refers to solution resistance, R_1 and constant phase element (CPE1) represent the charge transfer resistance and double-layer capacitance of oxide film/electrolyte interface [36]. A double layer equivalent circuit has been satisfactorily used to fit the spectra of composite coating. In this case, R1 and CPE1 represent the electric charge transfer resistance and capacitive characteristics of top layer of composite coating respectively. R2 and CPE2 represent the charge transfer resistance and electrical double-layer capacitance at the electrolyte/dense bottom layer interface [40]. The impedance parameter values of both pure Ti substrate and composite coating obtained after fitting the spectra to the equivalent circuit are presented in Table 7.2. It is observed that pure Ti substrate exhibits higher corrosion resistance with higher charge transfer resistance (R1) value compared to composite coating. This result from EIS test is consistent with the outcome from potentiodynamic polarization test. A relatively lower corrosion resistance indicates more active interaction between composite coating and Hanks' solution. The formation of apatite layer on the surface of composite coating after immersion in Hanks' solution in following study verified this active interaction.

Table 7.2 EIS spectra fitting results using the electrochemical equivalent circuits of Fig.7.8

Material	$R_1(\Omega cm^2)$	$CPE1(Fcm^{-2})$	n_1	$R_2(\Omega cm^2)$	$CPE2(Fcm^{-2})$	n_2
Ti sub	3.53×10^5	3.81×10^{-5}	0.88	-	-	-
20%HAP/Ti	0.21×10^5	4.49×10^{-5}	0.81	0.35×10^5	0.18×10^{-3}	0.82

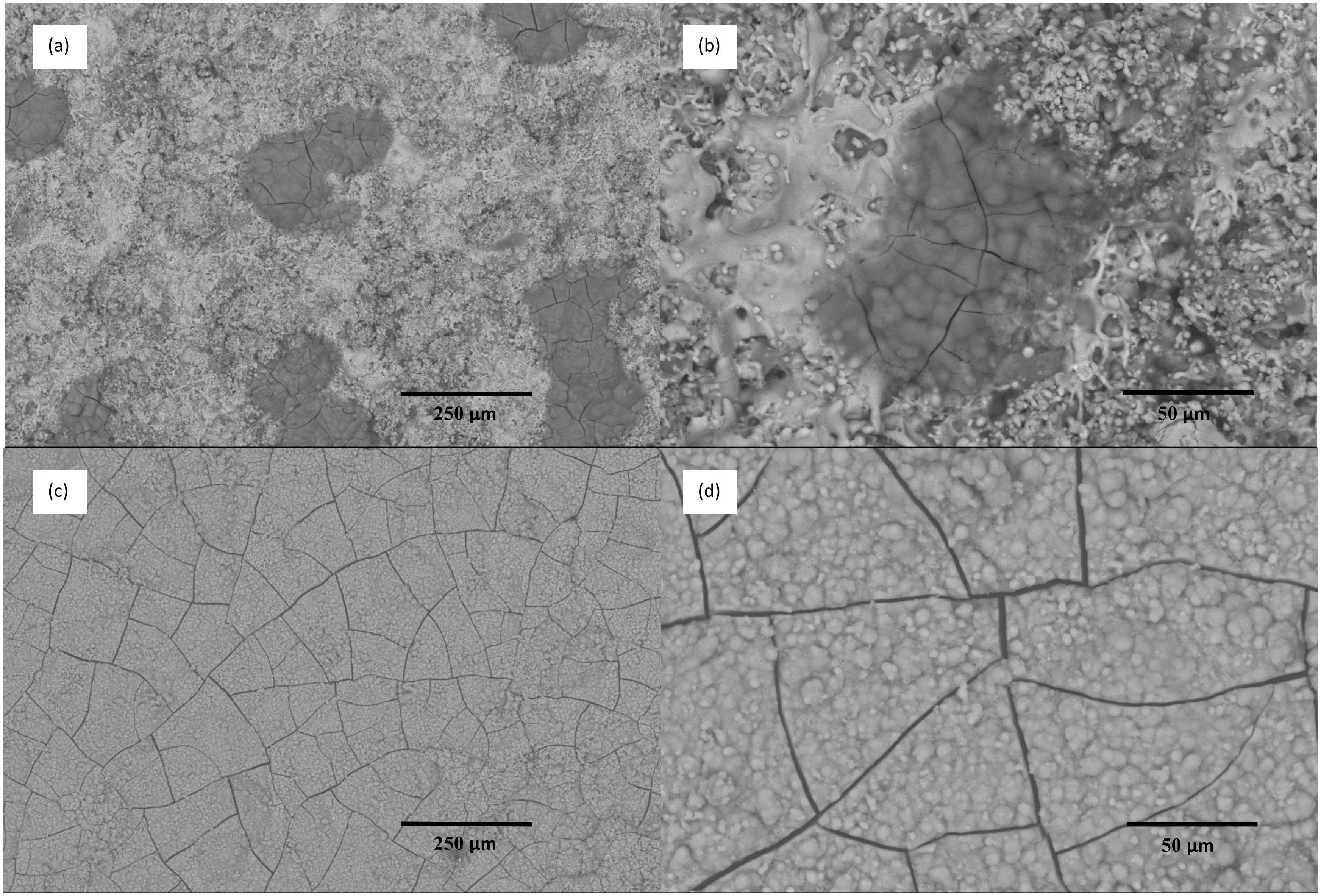

Fig.7.9 Scanning electron micrographs of AAPS 20wt% HAP/Ti composite coatings after immersion in SBF for: (a), (b) 3 weeks and (c), (d) 8 months; (b), (d) show detailed microstructure information in high magnification

7.4.2.4 Immersion Behavior Investigation

Apatite deposition on surface of understudied materials after immersion in SBF has been widely used to evaluate the bioactivity of implant materials. Plasma sprayed pure HAP or reinforced HAP composite coating has shown good bioactivity in vitro study [27, 28, 42]. Based on the previous researchers' observation and current study, the deposition of apatite commonly experiences three stages. At the first stage, the top surface of HAP coating appeared dissolved during immersion and some spherical particles precipitate. At the second stage, more spherical particles precipitate and the size of the initially precipitated spherical particles increases as immersion duration increases. At this stage, the surface of understudied material is found covered by a dune like apatite layer with spherical particles embedded inside. Finally, at the third stage, many granular particles nucleate and precipitate in the initially formed apatite layer, which indicates the continuous growing capability of apatite layer [27, 28, 42].

The surface morphologies of AAPS composite coatings after immersion in Hanks' solution for various periods are shown in Fig.7.9. In this study, in order to investigate the continuous growing capability of initially formed apatite layer, the immersion test was conducted for a long period and the surface morphologies of composite coatings after immersion in Hanks' solution for three weeks as well as eight months are shown in Fig.7.9(a) and Fig.7.9(c) respectively. Fig.7.9(b) and 7.9(d) shows detailed microstructure information in high magnification. It can be seen that after three weeks of immersion, dune-like apatite patterns formed on the surface of HAP/Ti composite coating (Fig.7.9(a)). The EDX analysis confirmed that Ca, P element contained in these patterns. Detailed examination revealed that these apatite patterns initially formed on the top surface of HAP part coating (Fig.7.9(b)). Compare Fig.7.9(a) and Fig.7.9(c), it is obvious that after immersion of eight months, the entire top surface of composite coating are covered by a thick, tortoise-shell like apatite layer. This result indicates that with the increase of immersion time, the apatite patterns initially formed on the top surface of HAP part coating spread and cover the Ti part coating. It is observed from Fig.7.9(d) that this apatite layer consists of many granular-like particles. It is easy to perceive that these granular-like particles grow from initially precipitated apatite patterns. In addition, after eight months of immersion, multiple large deep cracks of about 3 μm in size were observed that propagated along the surface of the coating. These microcracks are beleived caused by drying shringkage [28].

7.5 Mechanical Properties Characterization

The friction force was recorded continuously during wear test and the evolution of the coefficient of friction (COF) is plotted in Fig.7.10. It is observed that for AAPS 20wt% HAP/Ti composite coating, COF reaches steady state condition after initial 2,000 cycles and it takes 3,000 cycles for pure Ti substrate to be steady. However, for both types of samples, the steady state COFs are similar with a value of ~0.47, which indicates a similar frictional property of composite coating and pure Ti substrate. Fig.7.11 shows the mechanical properties (Vicker's microhardness and weight loss after wear test) of Ti substrate and composite coating. Composite coating shows a much higher hardness value of 498 Hv compared to the one of Ti substrate of 284 Hv. This result can be explained by the fact that our coating is a homogenous coating with low porosity (Fig.7.2). The melted HAP particles diffuse between the Ti particles and splats and enhance the bonding strength and hardness. For thermal sprayed composite coatings, besides porosity, many other factors should also be considered when evaluating mechanical properties such as crystallinity, residual stresses, HAP/Ti ratio and microstrutual features (particle size, micro-cracks) [38]. The resulting microhardness depends on the combined effects of these factors. The relatively higher hardness value of our composite coating compared with most of reported pure HAP or reinforced HAP coating indicates a good yielding strength of our coating [20, 43, 44]. In addition, when a relatively lower load is used, the indentation location, whether in the HAP splat or in the Ti splat, affects the result considerably. This explains the high standard deviation values found in our coatings.

The weight loss of two types of samples is also shown in Fig7.11. The weight loss value for composite coating is slightly higher (0.5 mg) than that of pure Ti substrate. The fact of no significant difference in weight loss for both types of samples is consistent with the previous observation of COF result (Fig.7.10). It needs to be pointed here that an inverse relationship between wear characteristics and hardness, namely weight loss decrease with increase of hardness has been reported [45]. Besides the hardness, the elastic modulus of studied material also has high effect on wear property [46]. The similar weight loss observed from two types of samples results from the fact that HAP is type of bio-ceramic material with very low elastic modulus. During wear test process, big HAP splat is easy to be crushed into small particles and peel off from the Ti matrix.

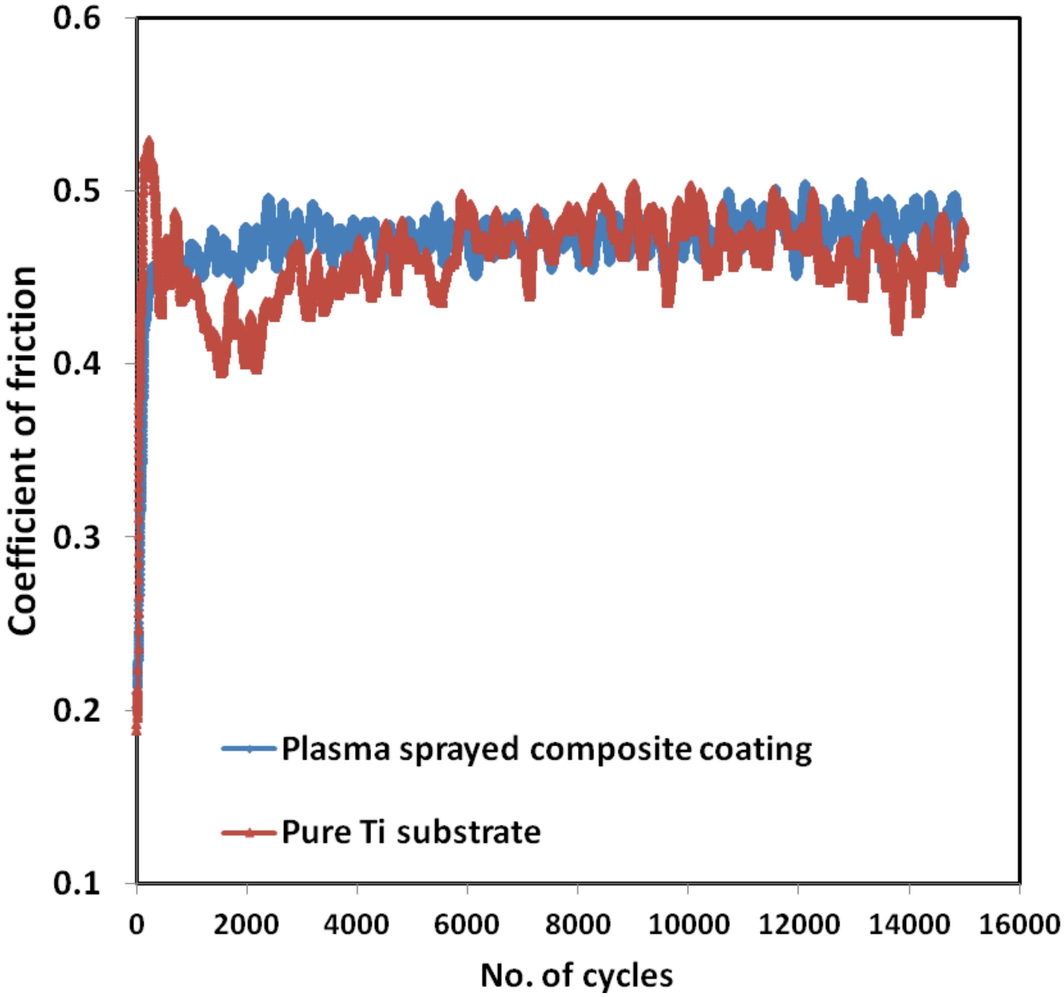

Figure 7.10 Evolution of the coefficient of friction of pure Ti substrate and AAPS 20wt% HAP/Ti composite coating versus number of cycles

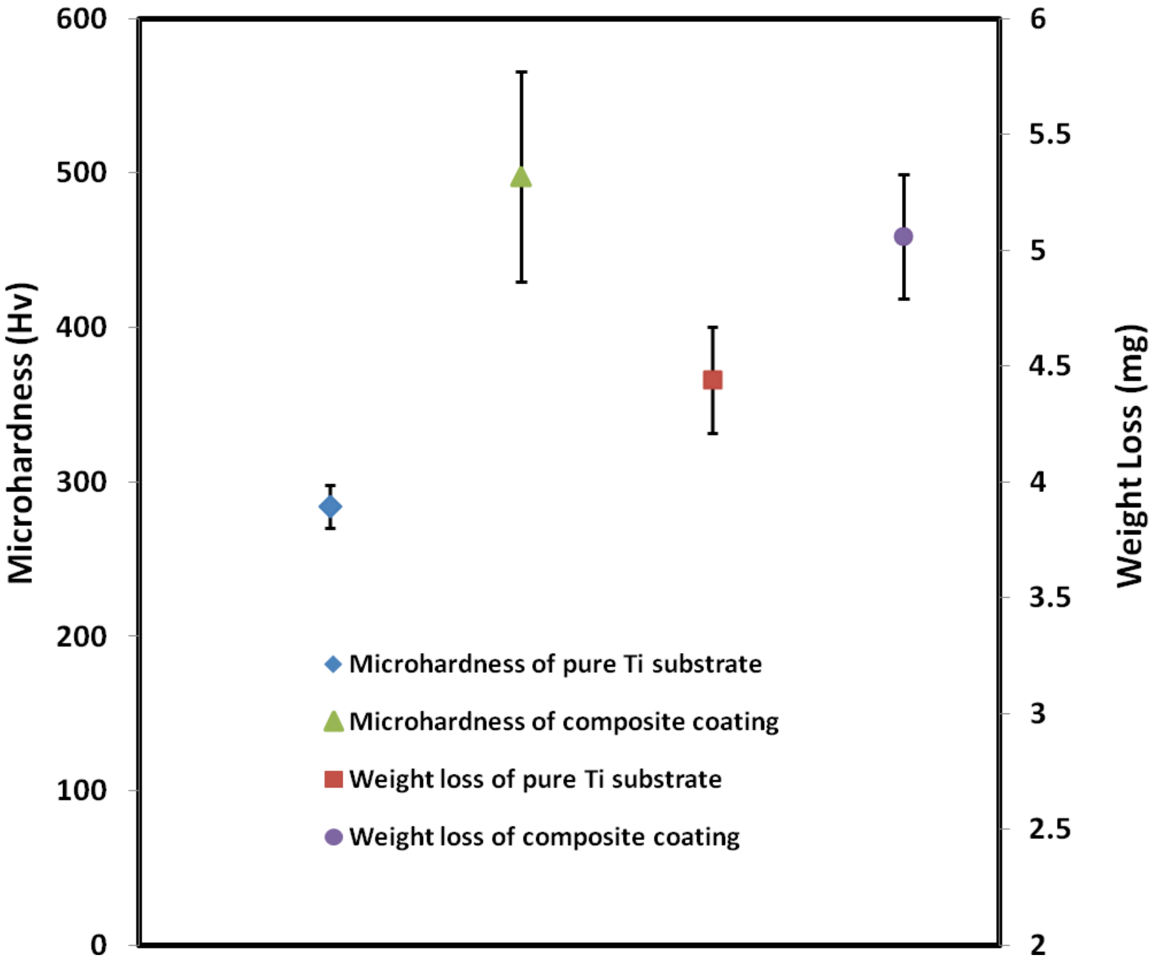

Figure 7.11 Comparing of Vicker's microhardness and weight loss of Ti substrate and AAPS 20wt% HAP/Ti composite coating

The bonding strength of composite coatings is averaged to 38.2 MPa, which is much higher than that of plasma sprayed HAP coatings [42] and Ti [20] or Ti6Al4V [27] reinforced HAP coating. The mismatch of the coefficients of thermal expansion between Ti substrate and HAP coating, thus high residual stresses remained after spraying, is the main reason of poor bonding strength of plasma sprayed HAP coating [20]. The addition of Ti to HAP coating reduces this mismatch and increases the bonding strength. The application of 80wt% of Ti in current study fulfills the high expectation of bonding strength. In addition, inert atmosphere reduces the oxidation of Ti and improves its bonding to Ti substrate further more.

7.6 Conclusions

20wt% HAP/Ti composite coatings were successfully deposited on the surface of Ti substrates by using AAPS technique. SEM images reveal that the coatings are dense and HAP is homogeneously distributed in Ti matrix. The XRD investigation shows that small amount of HAP is transformed to amorphous content during AAPS process but no obvious sign of HAP decomposition is found. Potentiodynamic polarization and EIS results display that composite coating has a slightly lower corrosion resistance than pure Ti substrate in SBF but indicate a good bioactivity. The immersion test conducted at 37 ^{o}C in SBF up to 8 months verified this conclusion. A thick, tortoise-shell like apatite layer covers entire surface of composite coatings after immersion of 8 months. The composite coatings also show good mechanical properties. The microhardness is averaged as 498 Hv; the frictional property is comparable to Ti substrate and the bond strength is measured as high as 48.9 MPa. From above mentioned results, it can be deduced that AAPS deposited HAP/Ti composites are excellent implant material candidates for biomedical applications.

References:

[1] Yeon-Wook Kim, *Mater. Manuf. Processes* 25 (2010) 307.

[2] Yunfeng Li, Shujuan Zou, Dazhang Wang, Ge Feng, Chongyun Bao, Jing Hu, *Biomaterials* 31 (2010) 3266.

[3] M.R. Khan, N. Donos, V. Salih, P.M. Brett, *Bone* 50 (2012) 1.

[4] Byoung-Ki Lim, Fangfang Sun, Su-Chak Ryu, Kwangnak Koh, Dong-Wook Han, Jaebeom Lee, *Biomed. Mater.* 4 (2009) 7.

[5] M Bobby Kannan, Lynnley Orr, *Biomed. Mater.* 6 (2011) 11.

[6] C.Q. Ning, Y. Zhou, *Biomaterials* 23 (2002) 2909.

[7] Z. Zyman, J. Weng, X. Liu, X. Zhang, Z. Ma, *Biomaterials* 14 (1993) 225.

[8] K.A. Khor, P. Cheang, *J. Therm. Spray Technol.* 3 (1994) 45.

[9] E.P. Paschalis, Q. Zhao, B.E. Tucker, S. Mukhopadhayay, J.A. Bearcroft, N.B. Beals, M. Spector, G. H. Nancollas, *J. Biomed. Mater. Res.* 29 (1995) 1499.

[10] Y.C. Tsui, C. Doyle, T.W. Clyne, *Biomaterials* 19 (1998) 2015.

[11] L. -D. Piveteau, M.I. Girona, L. Schlapbach, P. Barboux, J. –P. Boilot, B. Gasser, *J. Mater. Sci. – Mater. Med.* 10 (1999) 161.

[12] M. Metikos-Hukovic, E. Tkalcec, A. Kwokal, J. Piljac, *Surf. Coat. Technol.* 165 (2003) 40.

[13] Subhadip Bodhak, Susmita Bose, Amit Bandyopadhyay, *Acta Biomater.* 6 (2010) 641.

[14] R.S. Lima, K.A. Khor, H. Li, P. Cheang, B.R. Marple, *Mater. Sci. Eng. A* 396 (2005) 181.

[15] H. Li, K.A. Khor, P. Cheang, *Biomaterials* 23 (2002) 85.

[16] Byung-Dong Hahn, Jung-Min Lee, Dong-Soo Park, Jong-Jin Choi, Jungho Ryu, Woon-Ha Yoon, Byoung-Kuk Lee, Du-Sik Shin, Hyoun-Ee Kim, *Acta Biomater.* 5 (2009) 3205.

[17] Hongjian Zhou, Jaebeom Lee, *Acta Biomater.* 7 (2011) 2769.

[18] Yi Huang, Lei Song, Tao Huang, Xiaoguang Liu, Yangfeng Xiao, Yao Wu, Fang Wu, Zhongwei Gu, *Biomed. Mater.* 5 (2010) 7.

[19] H. Li, K.A. Khor, P. Cheang, *Biomaterials* 25 (2004) 3463.

[20] Xuebin Zheng, Minhui Huang, Chuanxian Ding, *Biomaterials* 21 (2000) 841.

[21] Shinn-Jyh Ding, *Biomaterials* 24 (2003) 4233.

[22] Won-Gi Kim, Han-Cheol Choe, *Thin solid films* 519 (2011) 7045.

[23] J. Huang, S.M. Best, W. Bonfield, Tom Buckland, *Acta Biomater.* 6 (2010) 241.

[24] Congqin Ning, Yu Zhou, *Acta Biomater.* 4 (2008) 1944.

[25] C.E. Wen, W. Xu, W.Y. Hu, P.D. Hodgson, *Acta Biomater.* 3 (2007) 403.

[26] Deliang Qiu, Lejiao Yang, Yansheng Yin, Aiping Wang, *Surf. Coat. Technol.* 205 (2011) 3280.

[27] Y.W. Gu, K.A. Khor, P. Cheang, *Biomaterials* 24 (2003) 1603.

[28] Y.W. Gu, K.A. Khor, D. Pan, P. Cheang, *Biomaterials* 25 (2004) 3177.

[29] Z.L. Dong, K.A. Khor, C.H. Quek, T.J. White, P. Cheang, *Biomaterials* 24 (2003) 97.

[30] Kantesh Balani, Rebecca Anderson, Tapas Laha, Melanie Andara, Jorge Tercero, Eric Crumpler, Arvind Agarwal, *Biomaterials* 28 (2007) 618.

[31] H. Singh, B.S. Sidhu, D. Puri, S. Prakash, *Mater. Corros.* 58 (2007) 92.

[32] R.B, Heimann, T.A. Vu, *J. Therm. Spray Technol.* 6 (1997) 145.

[33] F. Brossa, A. Cigada, R. Chiesa, L. Paracchini, C. Consonni, *J. Mater. Sci. – Mater. Med.* 5 (1994) 855.

[34] V. Guipont, M. Espanol, F. Borit, N. Llorca-Isern, M. Jeandin, K.A. Khor, P. Cheang, *Mater. Sci. Eng., A* 325 (2002) 9.

[35] S. Beauvais, V. Guipont, F. Borit, M. Jeandin, M. Espanol, K.A. Khor, A. Robission, R. Saenger, *Surf. Coat. Technol.* 183 (2004) 204.

[36] X. Zhou, P. Mohanty, *Corros. Eng. Sci. Techn.* 47 (2012) 145.

[37] S.R. Radin, P. Ducheyne, *J. Mater. Sci. – Mater. Med.* 3 (1992) 33.

[38] Limin Sun, Christopher C. Berndt, Clare P. Grey, *Mater. Sci. Eng., A* 360 (2003) 70.

[39] Jianhui Xie, Ben Li Luan, *J. Mater. Res.* 23 (2008) 768.

[40] X. Zhou, Pravansu Mohanty, *Electrochim. Acta* 65 (2012) 134.

[41] M.C. Garcia-Alonso, L. Saldana, G. Valles, J. L. Gonzalez- Carrasco, J. Gonzalez-Cabrero, M. E. Martinez, E. Gil-Garay, L. Munuera, *Biomaterials* 24 (2003) 19.

[42] S.W.K. Kweh, K.A. Khor, P. Cheang, *Biomaterials* 23 (2002) 775.

[43]M.F. Morks, N.F. Fahim, A. Kobayshi, *Appl. Sur. Sci.* 255 (2008) 3426.

[44] Gurbhinder Singh, Surendra Singh, Satya Prakash, *Surf. Coat. Technol.* 205 (2011) 4814.

[45] F.J Gil, E Fernandez, J.M. Manero, J.A. Planell, J. Sabria, M. Cortada, L. Giner, *Bio-Med. Mater. Eng.* 5 (1995) 161.

[46] Subhadip Bodhak, Shekhar Nath, Bikramjit Basu, *J. Biomed. Mater. Res. A* 85 (2007) 83.

Chapter 8

Conclusions and Recommendations for Future Work

HAP bioceramic has been widely used in surgical implants to promote osteointegration with bone. However, it's mechanical strength as well as the coating manufacturing techniques such as plasma spraying limit the application domain of this novel biocompatible ceramic. In this study, both the mechanical strength enhancement by formulating a HAP/Ti composite coating as well as the preservation of the desired HAP morphology by developing suitable application techniques were explored. In order to avoid the decomposition of HAP, that typically occurs during plasma spraying process and reduce the oxidation of Ti powder simultaneously, cold gas dynamic spraying (CGDS) and argon atmosphere plasma spraying (AAPS) techniques were employed to fabricate HAP/Ti composite coatings on Ti substrate. Pure Ti coatings were also manufactured and investigated for comparison purpose. The results showed that compared to pure Ti coating, cold sprayed HAP/Ti composite coating exhibits higher corrosion current and lower corrosion resistance. However, the post spray heat treatment improve the corrosion property of HAP/Ti composite coating remarkably. In addition, the mechanical properties such as microhardness and ultimate shear strength of cold sprayed 20wt% HAP/Ti composite coating also improved up to three times by post spray heat treatment process. Plastic shear instability at the particle and substrate interface causes metallurgical bonding in cold spray process. As is well known, plastic strain does increase corrosion rate, and hence as sprayed coatings exhibited higher corrosion currents. Upon heat treatment, recovery and recrystallization improved the corrosion resistance. Further, the recrystallization also improved the interfacial bonding and hence improved the mechanical properties. After one week of immersion, a dune like apatite layer was observed on the surface of 20wt% HAP/Ti composite coating and the apatite layer became denser and thicker with the increase of immersion duration. Thus, cold sprayed HAP/Ti composite with post heat treatment has the potential to be used as a bioceramic of choice.

For AAPS deposited HAP/Ti composites, SEM images reveal that the coatings were dense and HAP was homogeneously distributed in Ti matrix. The XRD investigation showed that small amount of HAP transformed to amorphous content during AAPS process but no obvious sign of HAP decomposition was found. It is to be noted that when 100% HAP is sprayed by plasma process, normally a significant portion of the HAP transforms to undesirable amorphous phase. However, the presence of significant portion of Ti in the feed stock appeared to have a positive impact on phase preservation. This may be due to the preferential absorption of thermal energy by the titanium powders during the transit in the plasma plume. Ti being highly conductive would absorb more energy compared to the ceramic HAP powders. Thus, the HAP phase would not be overheated, thus reducing the possibility of being quenched in the coating and forming the undesirable glassy phase. Potentiodynamic polarization and EIS results displayed that composite coating had a slightly lower corrosion resistance than pure Ti substrate in simulated body fluid (SBF) but indicated a good bioactivity. The immersion test conducted at 37 ^{o}C in SBF up to 8 months verified this conclusion. A thick, tortoise-shell like apatite layer covered the entire surface of composite coatings after immersion of 8 months. The composite coatings also showed good mechanical properties. The microhardness averaged around 498 Hv; the frictional property was comparable to Ti substrate and the bond strength measured as high as 48.9 MPa.

From the above observations, it can be deduced that CGDS or AAPS deposited HAP/Ti composites are excellent candidate materials for biomedical applications. While the AAPS material showed promising properties, it should be noted that it is an expensive process due to the requirement of maintaining an inert environment. Another important question that was addressed in the study was the minimum required HAP content in the composite coating that is absolutely necessary to promote bioactivity in a timely manner. It was observed that 20% HAP is sufficient to promote significant bioactivity. Therefore, a composite coating is a preferred choice due to

- Improved mechanical properties compared to 100% HAP coating.
- Phase preservation
- Reduced cost due to less HAP requirement (HAP~500$/lb and Ti~80$/lb).

Specifically, cold spray process is preferred due to higher material utilization and lower operation cost.

Although, in-vitro studies do show good promises, further *in vivo* experiments are needed to evaluate the acceptance of composite coatings for surgical operation.

Furthermore, from manufacturing and property evaluation prospectives, the following aspects need more investigation

- Deposition efficiency of the composite material.
- Retention ratio of HAP powder in the coating compared to the feed stock.
- Mechanical strength using nano-indentation techniques instead of shear punch test

Publications Arising From This Work

Journal Papers

X. Zhou, Raj Siman, Lin Lu, Pravansu Mohanty, Argon atmospheric plasma sprayed hydroxyapatite/Ti composite coating for biomedical applications, Journal of Surface and Coating Technology, 207 (2012) 343–349.

Xuan Zhou and Pravansu Mohanty, Corrosion behavior of cold sprayed titanium coatings in simulated body fluid, Corrosion engineering, science and technology, 47 (2012) 145-154.

Xuan Zhou and Pravansu Mohanty, Electrochemical behavior of cold sprayed hydroxyapatite/titanium composite in Hanks' solution, Electrochimica Acta, 65 (2012) 134– 140.

Conference Presentation and Paper

Xuan Zhou and Pravansu Mohanty, Study of High-Frequency Artifacts on EIS Measurements of Ti and Its Alloys in Simulated Body Fluid, ECS Transaction, 33 (2011) 59-68.